Nonvolatile Hologram Storage in $BaTiO_3$

by

Thomas William McNamara

B.S., Johns Hopkins University (1988)

S.M., Massachusetts Institute of Technology (1991)

Submitted to the Department of Electrical Engineering and Computer Science
in Partial Fulfillment of the Requirements for the Degree of

Doctor of Philosophy in Electrical Engineering and Computer Science

at the

Massachusetts Institute of Technology

September 1996

Signature of Author _____

Department of Electrical Engineering and Computer Science

June 27, 1996

Certified by _____

Cardinal Warde

Professor of Electrical Engineering

Thesis Supervisor

Accepted by _____

F.R. Morgenthaler,

Professor of Electrical Engineering

Chair, Departmental Committee on Graduate Students

Nonvolatile Hologram Storage in $BaTiO_3$

by

Thomas William McNamara

Submitted to the Department of Electrical Engineering and Computer Science
on July 1, 1996 in Partial Fulfillment of the Requirements for the Degree of
Doctor of Philosophy in Electrical Engineering and Computer Science

ABSTRACT

A key obstacle to the development of high-capacity three-dimensional information mass storage systems using photorefractive crystals is that readout of holograms stored in the conventional manner is destructive. Thus hologram fixing in these materials is important if practical systems are to be built. High-temperature (80–120°C) photorefractive grating writing results for a variety of pure and doped barium titanate ($BaTiO_3$) crystals are presented. Strong fixable secondary gratings were found to be correlated with increasing levels of Fe and Ni in doped crystals. Fixing was not observed in our pure crystals or those doped with V, Rh, or Co. Fixing was enhanced in an iron-doped crystal reduced by high-temperature annealing at low oxygen partial pressures, but not in reduced undoped, Co-doped or V-doped crystals. It was also found that the diffraction efficiency of a fixed grating in $BaTiO_3$ is a strong function of temperature, grating period and crystal orientation. Diffraction efficiency was improved by at least two orders of magnitude (from 0.1% to 10%) over earlier ionic fixing processes in $BaTiO_3$. Lower temperatures lead to longer storage times. The ionic carriers forming the fixable gratings have thermally activated mobilities of 1.77 eV and 0.76 eV.

Thesis Supervisor: Cardinal Warde
Title: Professor of Electrical Engineering

Contents

List of Figures

List of Tables

Chapter 1

INTRODUCTION

Photorefractive phenomena can be observed in any material which is photoconductive, transparent to the wavelengths of interest, and electrooptic. When a transparent photoconductor is exposed throughout its volume to a three-dimensional interference pattern, charge carriers are generated in the bright regions and recombine in the dark. The result is a faithful three-dimensional recording of the original light intensity, stored as a space-charge pattern. The electric field due to this charge separation modulates the refractive index through the electrooptic effect, so that a phase-only volume hologram develops in real time. These photorefractive holograms persist in the dark but can be erased by shining spatially uniform light through the crystal, so that photorefractive media are fully reusable.

Unfortunately, optical readout erases photorefractive holograms. Several optical techniques have been used to get around this difficulty. For example, the problem can be partially solved by using a "safe" readout wavelength to which the crystal is not very sensitive. The disadvantages of this procedure are that: (1) readout is still destructive over many readout cycles, particularly at high readout intensity levels, (2) two lasers are necessary, and (3) the stored image is distorted on readout. The life of the hologram may be extended during destructive readout by optimizing the applied

electric field [1]. Alternatively, storage of an array of binary pixels can be maintained by optical "refresh" or positive-feedback bistable imaging systems employing one or more photorefractive crystals [2, 3, 4]. However, the storage densities demonstrated so far in these systems have been very low, and the systems are complex.

A better solution is to use a fixing procedure to render recorded holograms insensitive to photoconductive erasure. Fixing is usually accomplished by techniques which somehow free light-insensitive secondary charge species to move in the space-charge electric field of the primary photorefractive grating.

Microscopic physical mechanisms which have been found to explain the properties of secondary gratings include thermally activated ionic drift and formation of alternating microdomains. Thus most techniques for fixing photorefractive gratings belong to one of two broad categories: (1) those involving high-temperature recording and low-temperature readout (fixing by thermal cycling), and (2) those involving applied electric fields exceeding the coercive field of ferroelectric photorefractive media (electrical fixing) leading to microdomains. In this dissertation only thermal hologram fixing will be discussed in any detail. In thermal fixing, at sufficiently high temperatures, in some materials, secondary carriers are attracted to primary charges of the opposite sign, thus locally neutralizing some or all of the space charge which formed the original photorefractive hologram. When optical hologram writing ceases and the secondary carriers are once more fixed in place, uniform illumination is used to distribute the primary carriers evenly throughout the crystal, revealing the secondary grating. This fixed grating is not optically erasable. It may persist for years or longer at room temperature.

Multiplex holographic storage in photorefractive crystals has been receiving increasing attention from government and industry in the last few years. Some recent

results in lithium niobate include storage of 5000 images of 200 × 300 pixels each in a single 1 cm^3 crystal [5]. If the signal-to-noise ratio were sufficient and crosstalk low enough, that would correspond to an information density of 3×10^8 bits/cm^3. It is believed that the ultimate theoretical limit on the information density is on the order of one bit per cubic wavelength: 10^{12} bits/cm^3 at a wavelength of 1 μm [6]. At the same wavelength, optical disks are limited by diffraction to 10^8 bits/cm^2. Thus in principle 3-D holographic memory has storage capacity advantages over non-holographic 2-D optical storage.

The high storage density of volume holographic media has been achieved by angular multiplexing: each image is recorded as a volume hologram with a unique reference wave. Each hologram can then be retrieved by re-illuminating the crystal with the appropriate reference wave. Since each hologram is Bragg matched to a unique reference wave, selective retrieval is possible with very low crosstalk [5, 7]. The requirement for addressing a particular hologram is merely angular scanning of a collimated beam (the storage medium itself need not move). The seek time for an entire page of data can be short by the standards of conventional mass storage devices (less than 1 ms with commercially available beam scanners, compared to 5–10 ms for current magnetic disk drives).

1.1 Summary of Original Results Presented in this Thesis

The following original experimental results were obtained during the course of this thesis research:

1. For the first time, high-diffraction-efficiency holograms (η =10%) have been fixed by thermal cycling in $BaTiO_3$. This result is very significant for appli-

cations, because electrical fixing techniques used in $BaTiO_3$ use a "revealing" step, which erases the stored holograms [8, 9].

2. The formation of ionic holographic gratings in $BaTiO_3$ crystals has been found to be correlated with Fe and Ni doping. Earlier studies did not report any details of impurity effects. This is critical because impurity doping is necessary for generating sufficient mobile oxygen vacancies to allow fixable gratings to be written.

3. Diffraction efficiency of fixed gratings was found to depend strongly on temperature, grating period, and crystal orientation.

4. The thermal fixing process in $BaTiO_3$ was greatly improved by separating the readout and storage steps.

5. Two different temperature-activated fixing mechanisms have been observed in one $BaTiO_3$ crystal. Evidence suggests that one mechanism consists of thermally activated oxygen vacancies. The other may possibly be thermally activated hydrogen ions weakly bound to oxygen atoms in the lattice.

1.2 Fixing Holograms in Photorefractive Materials

We adopt the definition here that a fixing process is one whose storage time (τ_s) is much longer than its writing time (τ_w) at constant light intensity. For high performance this asymmetry should be as large as possible ($\tau_s/\tau_w = 10^6$ or more). For instance, if τ_s =10 years and τ_w = 1 minute, $\tau_s/\tau_w \simeq 5 \times 10^6$ (see Fig. 1.1). Obtaining a high ratio τ_s/τ_w depends primarily on making the ionic mobility decrease as much as possible on cooling from writing to storage temparature. This in turn requires: (1)

a high activation energy for the ionic carriers, and (2) a high writing temperature and low storage temperature. Control of the concentration of ionic carriers allows τ_s and τ_w and writing time to be varied together, but will not change τ_s/τ_w greatly. Thus storage time can be increased at the expense of a proportional increase in writing time. This could be accomplished by lighter doping leading to a lower concentration of mobile ions.

Historically, thermal fixing methods were reported first in $LiNbO_3$ crystals, by Amodei and Staebler [10]. Writing took 30 minutes at 100°C or above and fixing was accomplished by cooling the crystal to room temperature. This froze the secondary grating in place, and illumination with uniform light to redistribute the photorefractive carriers uniformly revealed a phase grating which was not optically erasable. It has since been shown that the fixable gratings in these crystals were formed by charge compensation of photorefractive gratings by hydrogen ions with a temperature-activated mobility [11]. These "bare protons" formed OH^- centers which were detected by their infrared absorption near 3μm. The concentration of these ions could be increased by annealing the crystals in a water vapor atmosphere, or decreased by heating in a dry atmosphere [12]. The fixing properties were found to improve or disappear accordingly.

Holograms have been thermally fixed in photorefractive $Bi_{12}SiO_{20}$ (BSO) and potassium niobate ($KNbO_3$). Arizmendi [13] reported fixing in BSO by thermal cycling between room temperature and 260°C. Since BSO is not ferroelectric, ionic drift was suspected as the cause of the observed secondary gratings, but the nature of the ions was uncertain. Fixing by thermal cycling was accomplished in $KNbO_3$ by Montemezzani and Günter [14]. Montemezzani et al. based theoretical work including a set of transport equations for the coupled photoconductive-ionic system on their

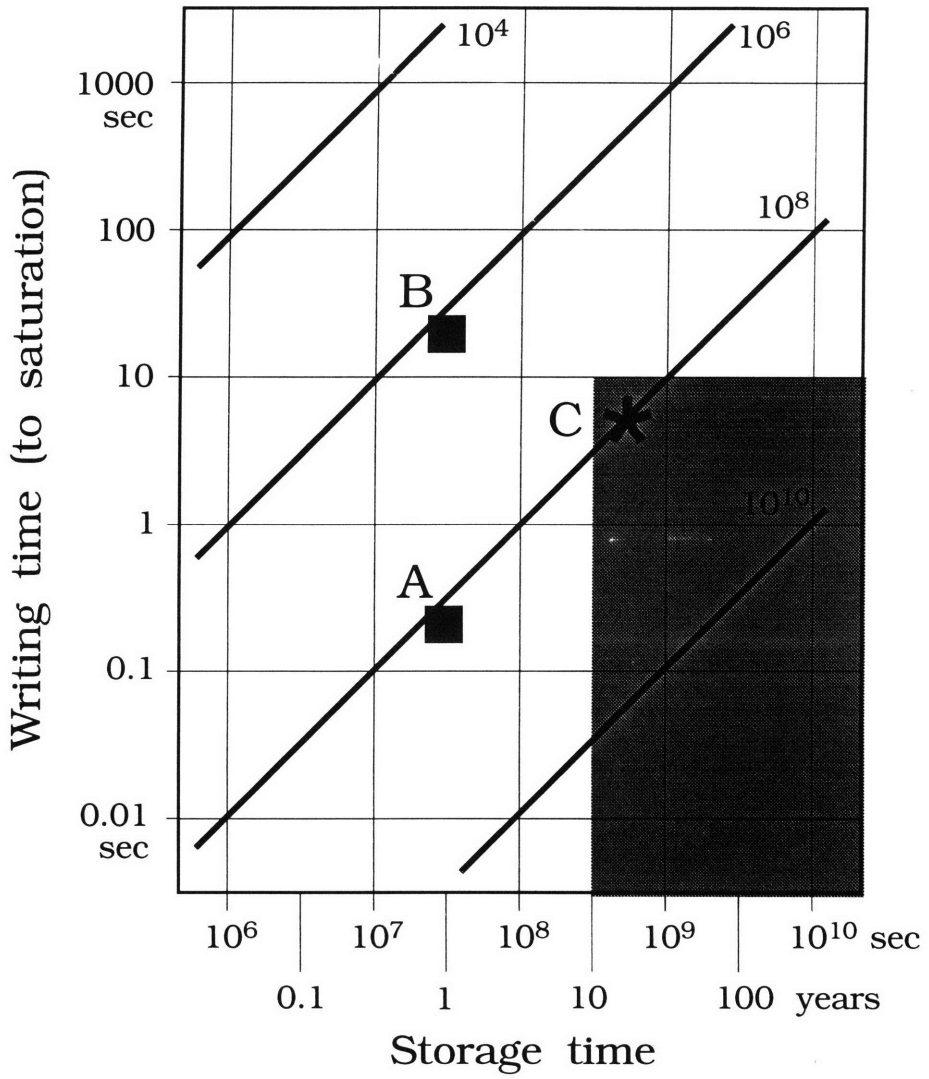

Figure 1.1: Diagonal lines: storage and writing times attainable at various ratios τ_s/τ_w. (**A**): $BaTiO_3$:Fe, 1kppm, reduced, writing T=120°C. (**B**): same crystal; writing T=95°C. (**C**): This point should be attainable by using the same writing temperature as for point A but lowering the concentration of mobile ions (less doping leads to lower ionic conductivity). Shaded area defines performance needed for data storage or optical interconnect applications.

observations in that material [15].

$BaTiO_3$ has very large electrooptic coefficients and low absorption at red and infrared wavelengths, making it one of the most promising materials for nonvolatile storage of high-diffraction-efficiency volume phase holograms. To this end, several workers have demonstrated techniques for fixing holograms in $BaTiO_3$ [8, 16], [104,105]. Electrical fixing in $BaTiO_3$ was first demonstrated by Micheron and Bismuth [8] as well as in strontium barium niobate (SBN) [17]. They used a four-step technique: (1) a photorefractive hologram was written to saturation in a poled crystal; (2) a negative (opposite to the sense of the poling field) voltage pulse exceeding in magnitude the coercive field for ferroelectric switching ($\sim$ -1 kV/cm) was applied to form a fixed compensating secondary grating, resulting in a lowered diffraction efficiency as primary and secondary gratings cancelled out; (3) the crystal was illuminated uniformly to redistribute the carriers of the primary grating, revealing a fixed grating with a high diffraction efficiency; (4) erasure was accomplished by applying a positive repoling field which was several times the coercive field of the crystal. Micheron and Bismuth reported much higher diffraction efficiencies in SBN than in $BaTiO_3$, but recent workers have had difficulty achieving these values [18]. Garrett et al. have recently used a one-time revealing field to obtained high diffraction efficiencies from electrically fixed holograms in $BaTiO_3$. But the revealing field apparently acts by repoling the crystal, eliminating the fixed grating and leaving behind a compensating space charge pattern that quickly decays. Thus this technique allows long hologram storage times but readout is destructive. Application of electric fields can cause cracking near the electrodes in many ferroelectrics, limiting crystal lifetime. However, electrical fixing has the advantage of room-temperature operation.

It is sometimes difficult to determine experimentally whether fixed gratings are due

to ionic drift or microdomain formation. In fact, both mechanisms have been found in some materials (including $BaTiO_3$). Long-range ionic drift can often be distinguished from microdomain formation in photorefractive ferroelectrics by determining whether the process is sensitive to the polarity of fields applied along the crystal's axis of polarization. Repoling with fields well above the coercive field in the material will erase gratings consisting of microdomains [8, 17].

In $BaTiO_3$, fixing has been accomplished by heating crystals to about 100°C without any applied field by Kirillov and Feinberg [16]. Kirillov and Feinberg have argued that the secondary grating in the thermal cycling experiments were ions [16], but did not report any attempts to erase their fixed gratings by applying an electric field. Practical problems encountered in their pioneering work led to very low fixed-hologram diffraction efficiencies, and the most effective crystals used were of unknown composition [16].

Data will be shown in Chapter 3 below, that indicate that thermal fixing is effective in iron- and nickel-doped $BaTiO_3$, but not to any significant degree in undoped crystals or as-grown samples doped with cobalt, vanadium or rhodium [19]. One sample, doped with 1000 parts per million atomic (ppma) of iron and annealed at 800°C in a reducing atmosphere with an oxygen partial pressure of 10^{-4} atm, seems to be the most promising. In this crystal, fixed-grating diffraction efficiencies of several percent have been stored over times far in excess of 24 hours by exploiting crystal orientation and readout temperature. The orientations explored were limited by geometrical considerations in our original setup; we expect to see significant improvement in diffraction efficiency when the optimal orientation is found. Further, we have noticed that the writing intensity can be varied to enhance the diffraction efficiency of the fixable holograms. By optimizing crystal composition, reduction state,

orientation, writing temperature, writing intensity, readout/storage temperature and applied electric fields, it should be possible to obtain diffraction efficiencies in excess of 30% and storage times of several years.

Thermal fixing processes generally have the following disadvantage: during high-temperature writing to update a fixed hologram, all other holograms stored in the same crystal begin to decay. Therefore, thermal fixing processes developed to date are most suitable for read-only applications. Selective erasure of electrically fixed gratings has been reported recently in SBN crystals [20]. That opens up the possibility of random access erasable/rewriteable storage in photorefractive crystals.

Another practical consideration is that the most useful known photorefractive crystals, semi-insulators with high electrooptic coefficients, have wide bandgaps (typically around 3 eV) and thus in the undoped form are most sensitive to green or blue light. Unfortunately the most compact and efficient laser sources available, diode lasers, are not commercially available at these wavelengths. (Frequency-doubled near-IR diode lasers are an option.) Many workers are currently carrying out research on doping photorefractive crystals such as $BaTiO_3$ to improve their infrared photoconductivity. This opens the door to replacing ion lasers with inexpensive, compact, highly efficient diode laser sources in optical information storage systems with photorefractive components. Appendix A (at the end of this dissertation) describes original work on blue Rh-doped and newly-discovered green V-doped $BaTiO_3$ crystals that are highly sensitive to infrared light. Unfortunately, holograms have not been successfully fixed in these crystals. This represents a promising area for future research.

1.3 Dependence of Photorefractive Sensitivity on Temperature

Although $BaTiO_3$ currently has superior gain and diffraction efficiency compared with most other photorefractive materials, its response time and sensitivity at room temperature are still far short of theoretical limits which have been calculated based on the known dielectric properties and carrier mobility in these crystals.

Several workers have already reported substantial increases in photorefractive sensitivity in undoped $BaTiO_3$ [21] and other photorefractive materials [22, 23] at elevated temperatures. The temperature range typically explored is 10°C to 120 °C. The mechanisms responsible for this phenomenon have not been completely explained, but a temperature-activated photorefractive carrier mobility with an Arrhenius dependence has been observed in BSO in recent photorefractive mobility measurements reported by Nouchi et al. [24]. Rytz et al. [21], accounting for known temperature-dependent crystal parameters, suggested a similar mechanism in $BaTiO_3$ in 1986. However, little follow-up work on the temperature-dependent photorefractive sensitivity, gain, response time, and effective trap density in *doped* $BaTiO_3$ has been done to date. It is not yet known how crystal composition and processing should be chosen to best exploit the opportunity for high sensitivity at high temperatures.

The dependence of photorefractive sensitivity on temperature must be measured carefully, because, as is reported in this thesis, the absorption coefficients in $BaTiO_3$ can change substantially as the temperature is raised. In previous studies [21], this fact was not taken into account, and the absorption was measured only at room temperature. The photoconductivity of $BaTiO_3$ increases with increasing temperature. Sensitivity data as a function of temperature are reported in this thesis, and for the

first time incorporate the temperature variation of the optical absorption.

Therefore, in order to optimize real-time applications such as injection locking of multiple lasers, efficient laser beam cleanup, self-pumped phase conjugation, high-gain four-wave mixing and wavefront reconstruction, the effects of crystal composition, annealing treatment, orientation, and operating wavelength for high-temperature sensitivity will be reported.

Furthermore, since the fixing techniques explored so far depend upon photorefractive grating formation at high temperatures, increasing the high-temperature sensitivity of those Fe- and Ni-doped crystals should improve the diffraction efficiency and writing time for fixed gratings.

1.4 Applications of Holographic Information Storage

Holographic recording has been considered for high-density data and image storage applications almost since the invention of holography. So far it has not been introduced as a commercial product. The potential advantages of this technology over conventional magnetic disks are improved speed and capacity. Steadily improving performance in these areas should eventually overcome the disadvantages of high projected costs and the riskiness and expense inherent in development of any new technology. Many of the roadblocks that have slowed development of holographic data and image storage technology are materials issues. The performance of photorefractive media is sure to continue to improve as materials research continues.

Choice of the best holographic storage medium for a specific application requires consideration of several parameters:

- cost,

- permanence of stored holograms,
- simplicity of necessary equipment and procedures,
- achievable optical quality,
- diffraction efficiency of stored holograms,
- exposure requirements (speed),
- spatial resolution,
- maximum aperture (width $\times$ height),
- thickness (Bragg readout allows denser storage),
- range of useful wavelengths,
- mechanical properties.

Which of these properties are essential and which merely desirable depends upon the application. For example, a read/write system designed to replace a magnetic hard disk drive would require the recording medium to provide high resolution, excellent optical quality, high speed, high diffraction efficiency, low cost, red/infrared compatibility, and nonvolatile storage for years over a reasonable temperature range (< 40 °C). Unfortunately that combination of characteristics is beyond the current state of the art in holographic recording media.

In this thesis, a more modest design is envisioned. Full read/write operation is conceded to be more suited to magnetic disk technology at this time. Instead, a reusable write-once, read-many (WORM) system is proposed. The reasons for this are straightforward. The recording medium limited system performance (speed and

recording capacity) more than any other component. For WORM operation, the key requirements for the recording medium are resolution, optical quality, diffraction efficiency, cost, red/infrared compatibility, and nonvolatile storage. (Writing speed is not of paramount importance for a system that will normally be used in read-only mode.) It had previously been demonstrated (by other workers) that photorefractive $BaTiO_3$ could satisfy most of these requirements (details will be discussed in section 2.2.8). The uncertain areas were nonvolatile storage at high diffraction efficiency, optical quality, and cost. In this work, those three areas were addressed. By testing a wide selection of doped $BaTiO_3$ crystals' suitability for hologram fixing, it was demonstrated that iron- and nickel-doped $BaTiO_3$ consistently supports nonvolatile hologram storage. In addition, the high diffraction efficiency typically available in $BaTiO_3$ crystals makes them especially suitable for phase-conjugate readout.

Chapter 2

BACKGROUND

2.1 The photorefractive effect: modelling

2.1.1 Overview

Photorefractive materials exhibit large optical nonlinearity at very low optical intensities (mW/cm^2). This nonlinearity is due to optical charge redistribution in semiinsulating electrooptic crystals, and can be explained by band transport models incorporating defects that modify the photoconductivity. Photorefractivity is one of the few nonlinear optical effects that can redirect large amounts of power (approaching 100%) from a continuous-wave laser beam ([25], pp. v–vi). This makes the photorefractive effect uniquely useful for some applications. The purpose of the following section (2.1.2) is to introduce a simple model of the photorefractive effect and compare its predictions with experimental results. Section 2.2 is a summary of the relevant material properties of photorefractive $BaTiO_3$.

Historically, the photorefractive effect was discovered and termed "optical damage" during second harmonic generation experiments in $LiNbO_3$; its first reported application to holographic storage was in 1968 by Chen et al. [26]. Details on the physical mechanism behind the photorefractive effect are described in review articles by Günter [27] and Staebler [28]. Several longer review papers have been written on

the principles of the photorefractive effect [29, 30, 31, 32].

2.1.2 Physical model

In our physical model of photorefractive hologram writing (see Fig. 2.1), holes, of concentration p, can be optically excited from filled deep acceptors that have concentration N_A. Of these acceptors, some small portion N_A^- are ionized even in equilibrium and function as hole traps. The remaining acceptor concentration N_A^0 consists of neutral acceptors. These will be referred to as full traps. Overall charge neutrality is maintained by an ionized donor concentration N_D^+:

$$\left[N_A^-(\bar{r})\right]_{\mathbf{avg}} = \left[N_D^+(\bar{r}) + p(\bar{r})\right]_{\mathbf{avg}}, \tag{2.1}$$

where the averages are over the volume of the crystal.

As depicted in Fig. 2.2, the response of a photorefractive crystal to nonuniform illumination is the development of space-charge regions near intensity gradients. This is due to generation in the bright regions, diffusion, and recombination in the dark regions. Thus the space-charge field lines originate in the dark and terminate in the light. The first step in finding the electrical potential function $V(\bar{r})$ quantitatively is to write the space charge $\rho(\bar{r})$ in terms of the holes, traps, and compensating donors of our model:

$$\rho(\bar{r},t) = q\left[p(\bar{r},t) - N_A^-(\bar{r},t) + N_D^+\right]. \tag{2.2}$$

The space-charge electric field then satisfies:

$$\nabla \cdot \bar{\bar{\epsilon}} \cdot \bar{E}(\bar{r},t) = \rho(\bar{r},t). \tag{2.3}$$

Since the space charge stored in the traps depends only on the *excess* trapped charge, we define

$$N_1(\bar{r},t) = N_A^-(\bar{r},t) - N_D^+. \tag{2.4}$$

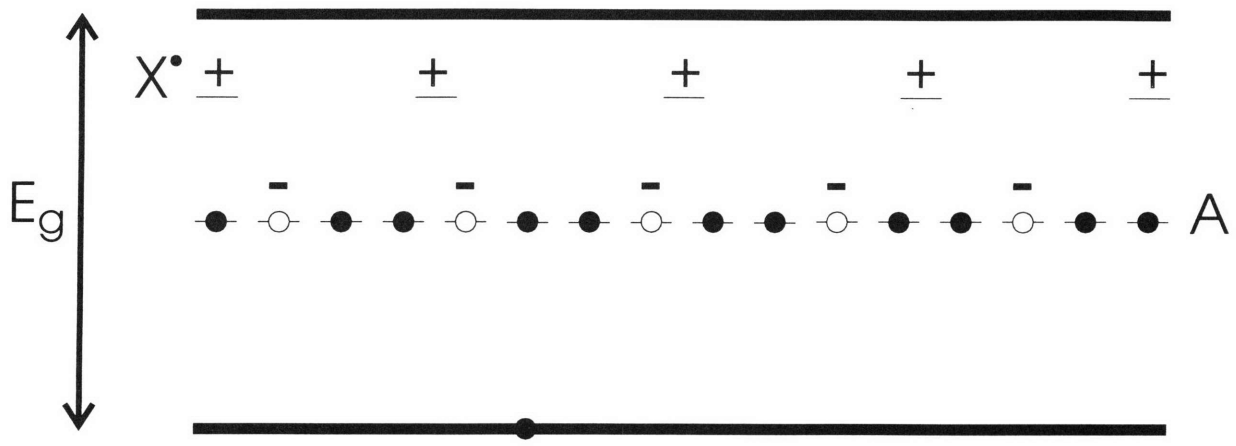

Figure 2.1: Simple model of photoconductivity in $BaTiO_3$. Charge compensation between negatively-charged deep acceptors A' (which function as hole traps) and positively-charged ions $X^{\cdot}$

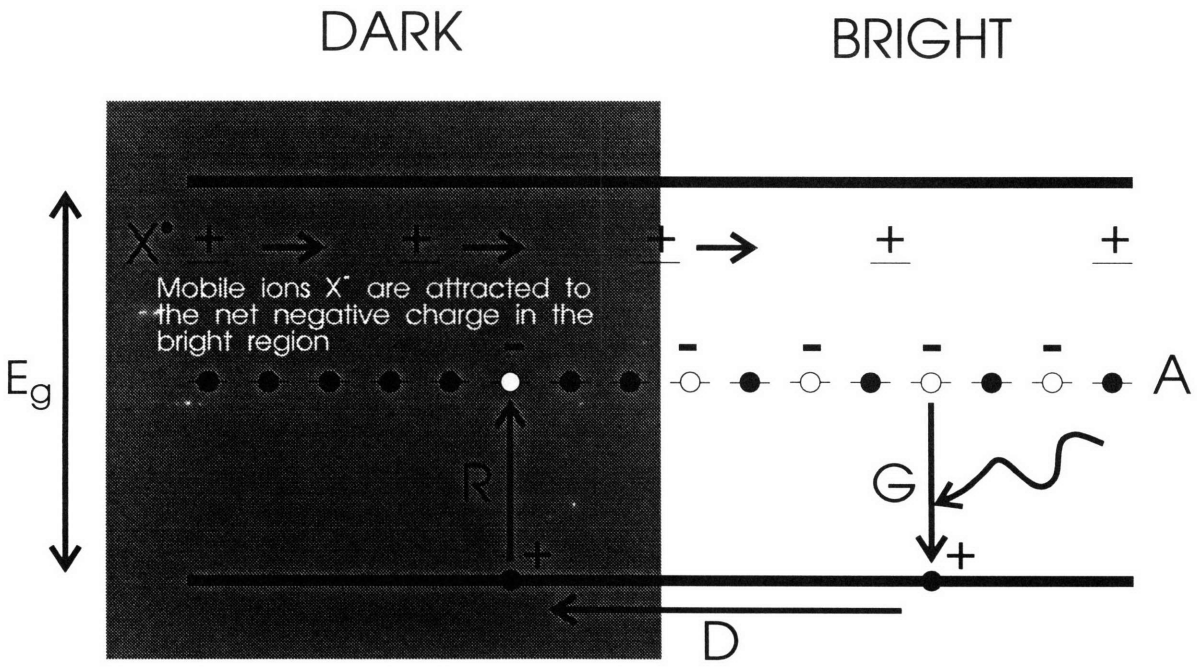

Figure 2.2: Energy-level diagram for barium titanate crystal under constant nonuniform illumination. Generation (G), diffusion (D), and nonradiative recombination (R) of holes (•) produce net negative charge [photoionized acceptors A′ (○)] in the illuminated region.

where the concentration N_D^+ of compensating ionized donors is a constant. We can write an equation of motion for N_1:

$$q\frac{\partial N_1(\bar{r},t)}{\partial t} = -\nabla \cdot \bar{J}_1(\bar{r},t), \tag{2.5}$$

where $J_1(\bar{r},t)$ is the current (due to the flow of holes.) We can divide this current into drift and diffusion components:

$$J_1(\bar{r},t) = q\mu_p \left[p(\bar{r},t)\bar{E}(\bar{r},t) - \frac{kT}{q}\nabla \cdot p(\bar{r},t) \right]. \tag{2.6}$$

Finally, we can find $p(\bar{r},t)$ in terms of the light intensity $I(\bar{r},t)$ and the full and empty trap concentrations by solving the rate equation

$$\frac{\partial p(\bar{r},t)}{\partial t} = -\frac{\partial N_1(\bar{r},t)}{\partial t} = s\frac{I(\bar{r},t)}{h\nu}N_A^0(\bar{r},t) - \gamma_R p(\bar{r},t)N_A^-(\bar{r},t). \tag{2.7}$$

Here s is the ionization cross-section of the filled traps and γ_R is the recombination coefficient. The formula (2.7) equates the rates of hole generation and trap emptying because it was assumed that holes excited to the valence band originate in the traps. Since the recombination time is much shorter than the photorefractive response time, we will always use the assumption of steady-state conditions when solving the rate equation (2.7). Setting the generation and recombination rates equal in (2.7), we obtain for the concentration of holes,

$$p(\bar{r},t) = \frac{sI(\bar{r},t)N_A^0(\bar{r},t)}{\gamma_R N_A^-(\bar{r},t)}. \tag{2.8}$$

Equations (2.1)–(2.8) comprise a general mathematical description of the time and space evolution of the populations of free holes and excess trapped holes in a photorefractive crystal with a single deep trap level and a single carrier type. Here the light intensity, given in three dimensions, supplies the driving term. No general solution of the system (2.1)–(2.8) has been found. In the remainder of this section we will

solve special cases of these equations and compare them with experimental data. In Chapter 5 we will add thermally activated mobile ions as a second, light-insensitive carrier type and compare the revised predictions with observations of fixable gratings. This generic optical model will be discussed further in the next chapter, where it is compared with a a defect chemical model of $BaTiO_3$.

2.1.3 Response of photorefractive media to spatially sinusoidal light intensity

One special case of the one-carrier photorefractive effect which is of great practical importance and can be solved approximately is that of sinusoidal illumination. In the Bragg grating writing system shown in Fig. 2.3, plane waves W_1 and W_2 interfere to create a sinusoidal intensity pattern in the photorefractive $BaTiO_3$ crystal X.

We neglect (until the next section) any effects of the index grating on the amplitudes or phases of the writing beams. We also neglect the photovoltaic effect [34, 35]. In the bright fringes within the crystal, photons are absorbed and mobile charge carriers of a single sign are generated by ionizing impurities. The mathematical model consists of Eqns. (2.1)–(2.8). Application of the model to the case of sinusoidal illumination of a photorefractive crystal is shown schematically in in Fig. 2.4. Diffusion tends to redistribute the holes more evenly in the material, leading to net space charge density peaks at the optical intensity minima (carriers) and maxima (uncompensated ionized traps left behind after diffusion of the carriers). The electric field sourced by the space charge distribution is 90° out of phase from the intensity pattern, and therefore so is the refractive index grating [see Fig. 2.4(a)].

In order to compare our model's predictions with experimental results, we need to make the above observations quantitative. Assume that the light intensity $I(\bar{r}, t)$

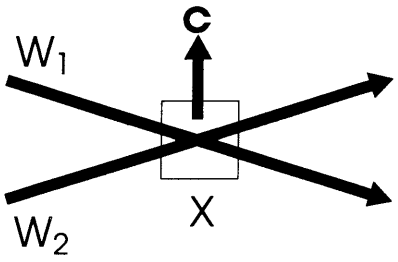

Figure 2.3: Generalized diagram of experimental geometry for writing sinusoidal Bragg gratings in $BaTiO_3$.

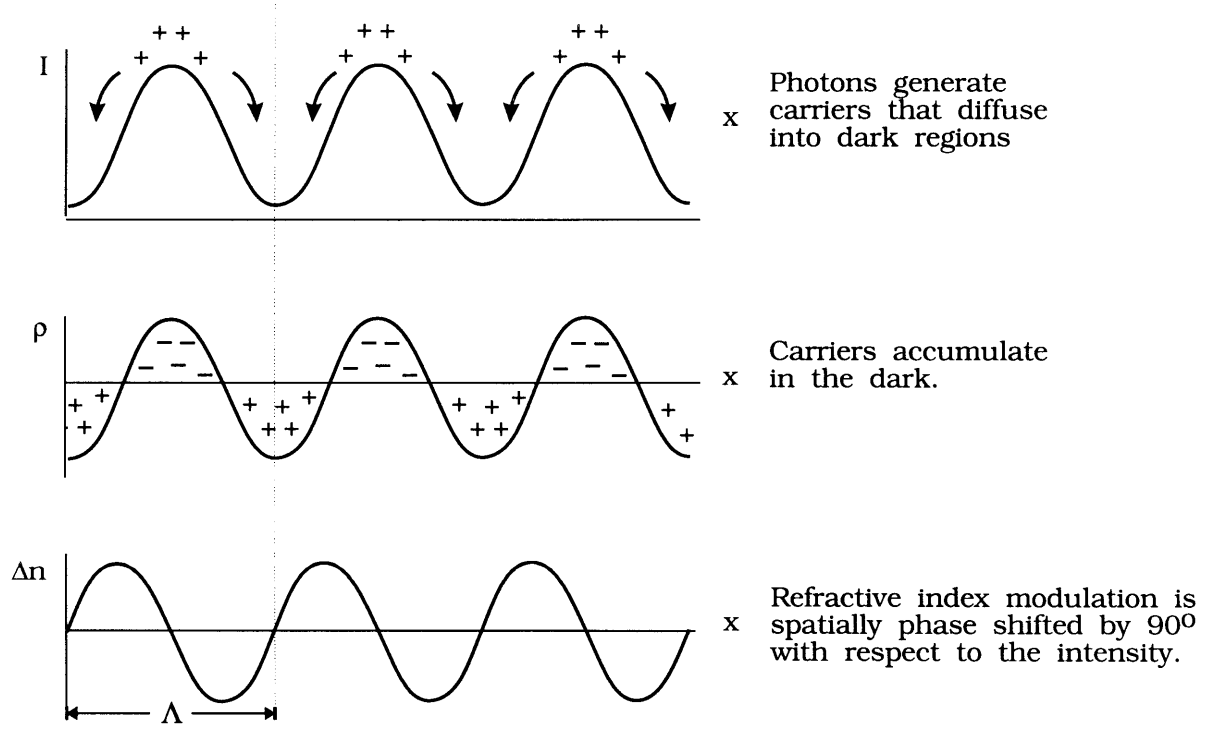

Figure 2.4: Sinusoidal light intensity within a photorefractive crystal: Diffusive charge redistribution leading to phase-shifted index modulation. After Valley and Klein [33].

within the crystal varies sinusoidally and along the x-axis only:

$$I(\bar{r},t) = I_0(t)\,(1 + m\cos(Kx))\,. \tag{2.9}$$

Here $I_0(t)$ depends only on time, m is the modulation depth of the intensity, and K is the magnitude of the grating vector. (Absorption of the writing beams is neglected.) It turns out that as long as the fringe modulation m is much less than one, we can find a simple approximate solution for the time dependence of the spatial Fourier series coefficients at wavenumber 0 and $\pm K$ for each variable in our basic model (2.1)–(2.8) [31, 32].

We assume that the solutions we require will vary little during the carrier lifetime τ_p. Here, $\tau_p = \left(\gamma_R N_A^-\right)^{-1}$. This assumption is valid for light intensity below about 1 MW/cm^2 [33]. We can safely use the steady-state rate equation (2.8) to determine carrier densities. We also assume, in the same intensity range, that the concentration of holes is much less than the concentrations of ionized donors and acceptors. Thus charge storage by free holes can be neglected at intensities lower than 1 MW/cm^2. Neither of the above assumptions is necessarily satisfied when the illumination source is a pulsed laser.

The refractive index modulation of a single-carrier photorefractive grating has the following time dependence [35]:

$$n_1(t) = n_{1\mathrm{ss}}[1 - \exp(-t/\tau_{\mathrm{PR}})]u(t). \tag{2.10}$$

Here τ_{PR} is the time constant of the photorefractive effect and $u(t)$ denotes the unit step. The time constant of the photorefractive effect can be calculated from the formula

$$\tau_{\mathrm{PR}} = \frac{\epsilon_r \epsilon_0}{\sigma} \frac{1}{1 + K^2/k_0^2}. \tag{2.11}$$

Eq. (2.11) can be understood as follows: for small K, the time constant is the same as the leaky dielectric relaxation time for small K. When K becomes comparable to the Debye screening wave vector k_0, diffusion currents become significant and τ_{PR} decreases.

During and after writing, photorefractive gratings can be read out by a Bragg-matched laser beam. The diffraction efficiency of a spatially uniform grating is given by

$$\eta = \sin^2\left(\frac{\pi n_1 L}{\lambda \cos\theta_0}\right), \tag{2.12}$$

where L is the interaction length, λ is the wavelength of the light, $n_1 = \frac{1}{2}n^3 r_{\text{eff}}|E|$ is the amplitude of the refractive index variation, and θ_0 is half the angle between the wave vectors of the writing beams inside the crystal [7].

2.1.4 Photorefractive coupling between the writing beams, steady state

The nonlinearity of the photorefractive effect introduces coupling of power between waves propagating in different directions. This phenomenon is known as beam coupling or two-wave mixing. Beam coupling is due to a spatial phase shift between the intensity maxima and the refractive index maxima. That in turn is due to the mechanism of charge redistribution through generation, diffusion, and retrapping shown in Fig. 2.4 (a). The electric field distribution arising in this case is spatially shifted by 90° along the grating vector $\mathbf{K}$, where

$$\mathbf{K} = \mathbf{k_1} - \mathbf{k_2}. \tag{2.13}$$

This vector gives direction and spatial frequency of the intensity in the fringes generated by interference between the two beams. The sense of the phase shift is determined by the sign of the relevant electrooptic coefficient. Each beam is scattered into the

other's direction by Bragg diffraction from the index grating, but due to the phase shift this is destructive interference in one case and constructive in the other. The fringe modulation m, which is the ratio of the peak sinusoidal spatial variation in the intensity to the sum of the intensities in the absence of interference, is expressed by

$$m = \frac{2\sqrt{I_1 I_2}}{I_0}, \tag{2.14}$$

where I_1 and I_2 are the beam intensities and $I_0 = I_1 + I_2$.

For the case $m \ll 1$, a perturbation treatment yields time constants and saturation values of the variables for the electric field and therefore the electrooptic refractive index modulation. First the saturation (steady-state) situation will be covered. A spatially periodic electric field is developed between the diffused space charge concentrations (see Fig. 2.4a). In the case where a single carrier species is involved in the grating writing process, the peak value of this field is given by [35]

$$\Delta \mathbf{E_{sc}} = -m \frac{k_B T}{q} \frac{1}{K + K_0}. \tag{2.15}$$

Here k_B is the Boltzmann constant, T is the temperature, q is the magnitude of the electron charge, $\mathbf{K}$ is the grating vector defined above, the interference fringe modulation m was defined earlier, and K_0 is a material parameter equal to

$$K_0 = \sqrt{\frac{Nq^2}{\epsilon_r \epsilon_0 k_B T}}, \tag{2.16}$$

where N is the effective density of deep traps (which depends on doping and processing), ϵ_r is the dielectric constant, and ϵ_0 is the permittivity of free space. The electric field allows the amplitude of the refractive index grating modulation to be calculated:

$$\Delta n = -\frac{1}{2} n^3 r_{eff} \Delta E_{sc} \tag{2.17}$$

[35]. The result of this index grating, in general, is power transfer between pairs of beams propagating through the crystal; the exact results are difficult to calculate

due to other interfering effects (Kerr effect, piezoelectric effect, and trap depletion). However, for the simple case of a weak probe beam and a strong, undepleted (where power exchange does not significantly reduce value) pump beam (the case of low m), the problem has a simple solution. The result in this case is an exponential increase in the intensity of the probe beam as it passes through the crystal:

$$I_{probe} = I_0 e^{\Gamma z}, \tag{2.18}$$

where the parameter Γ is called the beam coupling gain, and can be calculated as

$$\Gamma = \frac{4\pi\Delta n}{\lambda \cos(\theta)}, \tag{2.19}$$

where λ is the free-space wavelength and θ is the half-angle between the two interfering beams outside the crystal.

Therefore, as the two beams propagate farther through the interaction region, power is constantly coupled into one beam (toward the +**c**-axis, assuming a positive linear electrooptic effect) until the other is depleted or the beams exit the interaction region. Photovoltaic gratings, with an index change which is local to the optical intensity maxima in the crystal, do not induce any net power exchange between two beams. Holographic (one-beam) readout of previously written photovoltaic gratings is possible, of course [36].

2.1.5 Beam coupling: time dependent case, linear systems perspective

In real-time holographic media such as photorefractive crystals, diffraction of the writing beams from the hologram they create can strongly influence the writing process. This phenomenon is known as beam coupling. The theoretical description of beam coupling must be a self-consistent, time-varying solution. In the most general case,

this is very difficult to find analytically. The goal in this section is to present a general procedure for finding the transfer function for beam coupling, irrespective of the local response of the medium. Cronin-Golomb and others [37, 38, 39, 40, 41, 42] obtained more specialized answers that depend explicitly on the local impulse response of the photorefractive medium, which is assumed to be a single-carrier response. The result obtained here applies at least formally to any local photoconductive response that can be linearized, including the two- and three- carrier photorefractive media encountered when writing fixable holograms. A general prescription for obtaining the local transfer function from the measured coupled-beam transfer function is presented. The process of guessing differential equations to model the local response of the medium can thus be supplemented by direct measurements of the local transfer function. It will be shown that the results derived here reduce to the solution of Cronin-Golomb in the case of a single-carrier photorefractive crystal.

The time response of beam coupling in a photorefractive crystal (i.e., the impulse or step response relating input and output probe intensity) can be solved under the undepleted pump approximation. In this approximation, the two coupled beams are considered as plane waves and the intensity of the probe beam always remains much less than that of the pump. This regime is an important special case, both because it arises very commonly in experiments when the probe beam is made weak and because a very simple expression can be found for the transfer function relating the input and output probe intensities.

First, it is important to confirm that amplification by beam coupling is indeed a linear operation in the undepleted pump approximation. The pump and probe beams, considered as plane waves with $\mathbf{k}$ vectors $\mathbf{k_1}$ and $\mathbf{k_2}$, intersect in the crystal

and produce an intensity pattern with interference fringes of the form

$$I(z,t) = [I_1(z,t) + I_2(z,t)]\,[1 + m(z,t)\cos(\mathbf{K}\cdot\mathbf{r})]\,. \tag{2.20}$$

where the fringe modulation $m(z,t)$ was defined in the previous section. A fringe modulation approaching 1 corresponds to fringes with very deep modulation; a modulation much less than 1 corresponds to nearly constant light intensity. Since $m(z,t)$ is linear in the probe's optical electric field, and the nonlinear refractive index is linear in $m(z,t)$, we treat the crystal and pump as a linear system acting on the probe [37].

To approach the undepleted-pump beam coupling problem from a linear systems perspective, consider a very thin slab of photorefractive crystal. The slab thickness Δz is small enough that the change in probe amplitude $A_1(z,t)$ due to diffracted light from the pump $A_2(z,t)$ is always much less than the magnitude of $A_1(z,t)$:

$$|A_1(z+\Delta z,t) - A_1(z,t)| \ll |A_1(z,t)|. \tag{2.21}$$

Here and in the following analysis we have neglected optical absorption, which is low (approximately 1 cm^{-1}) in many photorefractive materials.

The time dependence of $A_1(z+\Delta z,t)$ is given by the convolution of $A(z,t)$ with the impulse response per unit length h(t) of the photorefractive writing process as defined in section 2.1.3 above. This impulse response will have the form

$$h_{\Delta z}(t) = \delta(t) + \Delta z h(t). \tag{2.22}$$

Thus its Laplace transform, the transfer function of a thin slab of thickness Δz, is

$$H_{\Delta z}(s) = 1 + \Delta z H(s), \tag{2.23}$$

where $H(s)$ is the Laplace transform of $h(t)$. Here Δz is made arbitrarily small, so that $H(s) \ll 1$ holds everywhere but at poles of $H(s)$. Thus the transfer function

for a weak probe beam on passing through a long slab of length $z = N\Delta z$, where $\Delta z = z/N$ and $N \to \infty$, is given by

$$H_z(s) = \lim_{N\to\infty} \left[1 + \frac{z}{N} H(s)\right]^N . \tag{2.24}$$

For finite N, this is one version of a discrete exponential function:

$$\exp[zH(s)] = \left(\exp\left[\frac{z}{N} H(s)\right]\right)^N . \tag{2.25}$$

In the limit $N \to \infty$, the expression inside the square brackets on the right-hand side, $\exp[\frac{z}{N}H(s)] \simeq 1 + \frac{z}{N}H(s)$. This fact can be used to write a closed-form expression for the long-slab transfer function:

$$H_z(s) = \lim_{N\to\infty} \left[1 + \frac{z}{N} H(s)\right]^N = \exp[zH(s)]. \tag{2.26}$$

Another, more careful but more mathematical, way to prove this result is by using the binomial theorem:

$$\lim_{N\to\infty} \left[1 + \frac{z}{N} H(s)\right]^N = 1^N + \binom{N}{1}\frac{z}{N}H(s) + \binom{N}{2}\left[\frac{z}{N}H(s)\right]^2 + \binom{N}{3}\left[\frac{z}{N}H(s)\right]^3 + \cdots . \tag{2.27}$$

Here the symbol $\binom{N}{i}$ stands for $N!/[i!(N-i)!]$, the i^{th} coefficient in the expansion of a binomial raised to the N^{th} power.

$$= \lim_{N\to\infty} \left(1 + zH(s) + \frac{1}{2!}[zH(s)]^2 + \frac{1}{3!}[zH(s)]^3 + \cdots\right). \tag{2.28}$$

$$H_z(s) = \exp[zH(s)]. \tag{2.29}$$

(Here we have used the fact that as $N \to \infty$, $\quad (N-1)/N \to 1$, $\quad (N-2)/N \to 1$, and so forth).

For the special case of single-carrier photorefractive gratings, we can compare the predictions of Eq. (2.29) with results derived in a different way by Cronin-Golomb and other workers [37, 39, 40]. For a single-carrier material, $H_{\Delta z}(s) =$

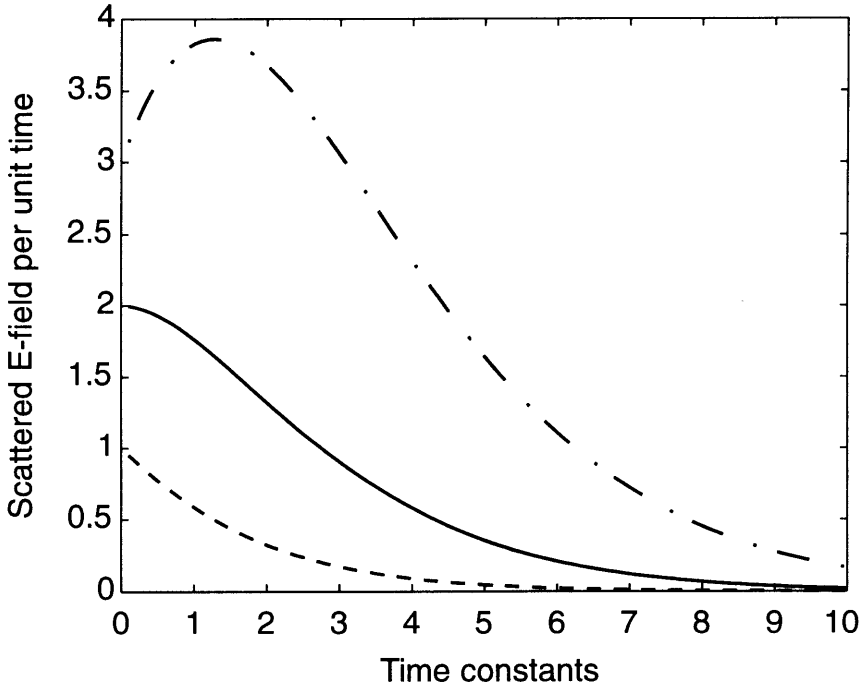

Figure 2.5: Impulse responses for amplified probe beam during beam coupling in a single-carrier photorefractive medium in the undepleted pump regime. Solid line: $\gamma L = 2$, dashed line: $\gamma L = 1$, dash-dot: $\gamma L = 3$.

$\exp\left(\tau_{PR}^{-1}\gamma z/(s+\tau_{PR}^{-1})\right)$ The inverse transform in this case can be found in closed form using a table of Laplace transforms [43] and contour integration:

$$h_z(t) = \delta(t) + \frac{\gamma L}{\tau_{PR}} e^{-t/\tau_{PR}} \sqrt{\frac{\tau_{PR}}{\gamma L t}} I_1\left(2\sqrt{\frac{\gamma L t}{\tau_{PR}}}\right), \tag{2.30}$$

Where I_1 is the modified Bessel function of first order, defined in terms of the Bessel function by $I_1(z) = -jJ_1(jz)$, where j is the imaginary unit ([43], p. 375). The impulse function on the right-hand side reflects the initial linear transmission of the probe beam; the remainder is due to diffracted pump light. This impulse response is plotted in Fig. 2.5 for several values of γL. Eq. (2.30) is valid in the undepleted pump regime.

In summary, a general closed-form expression has been derived for the transfer function $H_z(s)$ that acts on the probe amplitude in a thick crystal, in terms of the transfer function $H(s)$. $1+\Delta z H(s)$ is the transfer function of a slab of crystal that is thin enough that beam coupling can be neglected and the writing beam amplitudes can be considered constant with respect to z. The form of $H(s)$ will depend upon the photorefractive process involved; as shown in section 2.1.3 above, for a single-carrier photorefractive mechanism,

$$\Delta z H(s) = \frac{\gamma \Delta z}{s\tau_{PR}+1}. \tag{2.31}$$

In this case, the response contains (1) a term of magnitude one, corresponding to transmission of the probe directly through the crystal, and (2) a term yielding a first-order low-pass filter response, corresponding to the addition of diffracted pump light to the probe beam after passage through the thin slab Δz.

The general transfer function $H_z(s) = \exp[zH(s)]$ obtained here is useful for several reasons: (1) it can easily be adapted to produce the transfer function of beam coupling processes involving more than one charge carrier, such as those encountered

when writing thermally fixable gratings. To do this, the expression $H(s)$ given in (2.31) above is simply replaced by a different thin-slice transfer function. For the two- and three-carrier cases considered in Chapter 5, the impulse response can be written as a convolution of responses of the form (2.30). (2) it gives a prescription for extracting the local transfer function of a photorefractive medium at arbitrarily high gain-length products: take the logarithm of the complex beam coupling transfer function. Thus the formula $H_z(s) = \exp[zH(s)]$ is useful even when the differential equation for the local photorefractive response is unknown. (The spectrum can be measured by sweeping the frequency of an intensity-modulated probe beam or by numerically performing the FFT of the measured transient decay using numerical software such as MATLAB.) (3) it can be reduced to an expression that agrees with the known time response of conventional single-carrier beam coupling gain and phase response.

In addition to these advantages, the formula (2.29) is intelectually satisfying because its derivation is simple and it clearly yields identical results regardless of whether the crystal in question is considered as a whole or as a cascade of identical but shorter crystals. Vahey's solution [44] also had this property, but it yields inaccurate time constant values even though it seemingly provides a good fit to measured curves.

2.1.6 More complicated geometries

Applications of photorefractive materials in the early 1970s originally focussed on using photorefractive $LiNbO_3$:Fe, with its long dark storage time, to store spatial-frequency-multiplexed volume holograms. This seemed appealing because, given sufficient interaction length, a volume hologram can give readout efficiencies approaching 100% on readout at the appropriate Bragg angles for an arbitrary number of stored

holograms [7]. Interest in this application has declined, although work is still being done in the field; the current "record" is 5000 holograms stored in a $LiNbO_3$ crystal with no significant crosstalk observed on readout [5].

A spatial light modulator (the photorefractive incoherent-to-coherent optical converter, abbreviated PICOC) has been reported which uses erasure by an incoherent image of gratings scattering coherent light in photorefractive crystals to perform incoherent-to-coherent intensity conversion [45].

Beam fanning, a wide-angle spray of light often visible when beams pass through photorefractive crystals, can also be understood in terms of beam coupling. Spherical scattering wavefronts from centers at the crystal surfaces or due to internal inhomogeneities interfere with the main beam and couple power toward the **c** axis of the crystal, resulting in the characteristic "fan" of light arising gradually after an input beam is applied [35]. Because beam coupling gain depends on the fringe modulation between two beams, a uniform incoherent beam applied to the crystal which partially washes out all fringes present will reduce the amount of power lost to beam fanning [46].

More recently, much of the work on applications of photorefractive crystals has moved into other areas. Degenerate four-wave mixing (four-wave mixing optical phase conjugation with all four beams at a single frequency) (see Fig. 2.6a) can be performed in photorefractive crystals. In this geometry, the phasefronts of a beam are detected and read out by another beam, holographically generating the phase conjugate of the original wave amplitude. This property of the "reflected" beam (sign-flipping of the spatial- and time-dependent phases) requires propagation as a time-reversed version of the incident beam.

Phase conjugate reflection can compensate for a complicated distorting medium as

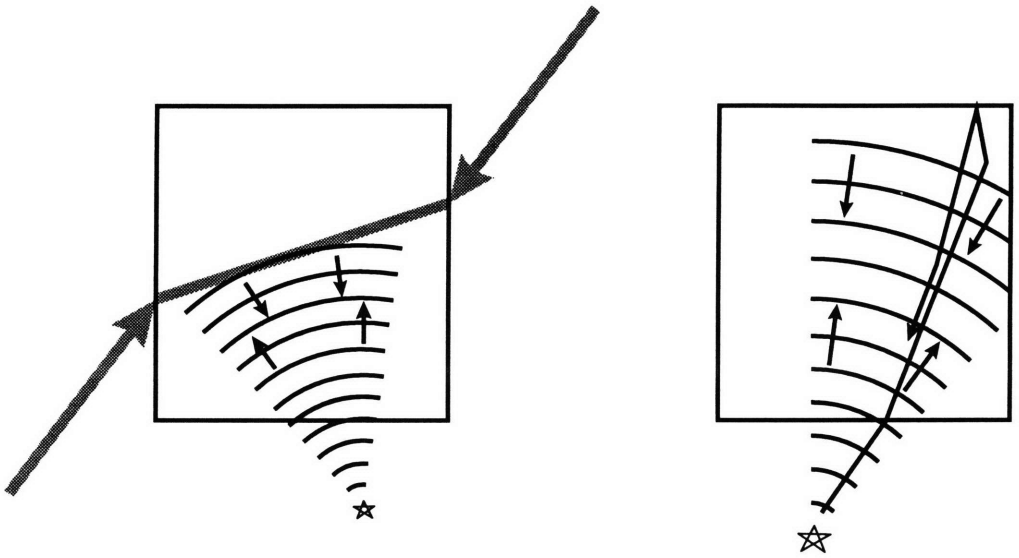

Figure 2.6: Phase conjugation in photorefractive crystals: (a) Degenerate four wave mixing with externally supplied reference beams; (b) Self-pumped phase conjugation

long as the medium lies in both the incident and reflected beam paths: the phasefronts retrace their path back to the source, generating a clean reflection. The effect can be of use inside laser cavities employing a distorting gain medium between a normal, partially transmitting mirror and a phase conjugator: the beam profile at the mirror will contain considerably less spatial noise than would otherwise be obtained. With a high-efficiency phase-conjugate mirror, the process can be more efficient than simple spatial filtering of the output beam. Elimination of the two external pump beams needed for the geometry in Fig. 2.6a has been an important step in this direction.

In some crystals, where beam coupling gain is high enough, a beam totally reflected at an interface near a corner of a crystal can couple to the return beam via additional fanning beams which arise (see Fig 2.6b); this phenomenon was first reported by Feinberg [47]. Under these conditions, a four-wave mixing geometry is set up, and the incident beam is phase conjugated. Phase-conjugate power reflectivities as high as 30% have been observed in nominally pure $BaTiO_3$ crystals [48].

Other devices making use of the photorefractive effect without employing gratings are discussed elsewhere in this thesis; generally their operation is simpler. Some of these devices include the Pockels Readout Optical Modulator (PROM) [49], the PRIZ [50], a device similar to the PROM which reads out an edge-enhanced transformation of the stored image, a photovoltaic spatial light modulator recently reported by Hong et al., and the P-BOD developed in this thesis.

Other applications of photorefractive crystals make use of the photoconductivity and transparency to control a modulator using another material (for example, liquid crystal [51]) or use the electrooptic effect and transparency to make electrically-controlled modulators (for example, integrated optical waveguide modulators in $LiNbO_3$). In the latter case, the photorefractive effect is detrimental and should be eliminated

by control of impurities if possible; this has been accomplished in $LiNbO_3$ by greatly decreasing the iron concentration in the growth melt.

2.2 Barium titanate

2.2.1 The barium titanate crystal lattice

Barium titanate ($BaTiO_3$) is a ferroelectric perovskite crystal. Each titanium ion in the crystal is enclosed by an octahedron of oxygen atoms. When the titanium atom moves off-center in the octahedron, the unit cell acquires a dipole moment. This happens when $BaTiO_3$ is cooled below 130°C. Between 4°C and 130°C at standard pressure, barium titanate ($BaTiO_3$) is a polar crystal with tetragonal 4mm symmetry (see Fig. 2.7). When cooled below 4°C the crystal structure becomes orthorhombic. When heated past about 130°C, called the Curie temperature T_C, $BaTiO_3$ becomes cubic and nonpolar. Thus properties that require inversion asymmetry of the crystal structure vanish–the Pockels electrooptic effect is not observed above T_C.

The unit cell dimensions of tetragonal $BaTiO_3$ are approximately $3.99 \times 3.99 \times 4.03$ angstroms (at room temperature). As we heat the material from room temperature to T_C, these lengths all converge toward 4.01 angstroms (see Fig. 2.8). Holograms fixed in $BaTiO_3$ by thermal cycling are recorded at high temperatures (90°C and above) and read out near room temperature. This means when the fixed holograms are read out, the crystal has been very slightly deformed by cooling.

$BaTiO_3$ is a mechanically brittle material, easily damaged during processing if proper care is not taken. It is sensitive to thermal gradients, which can cause cracking. It is also sensitive to temperature variations outside the tetragonal range given above. Sample growth and preparation-dependent quantities such as surface quality, degree of poling, and presence of cracks, grain boundaries, and small inclusions (leading

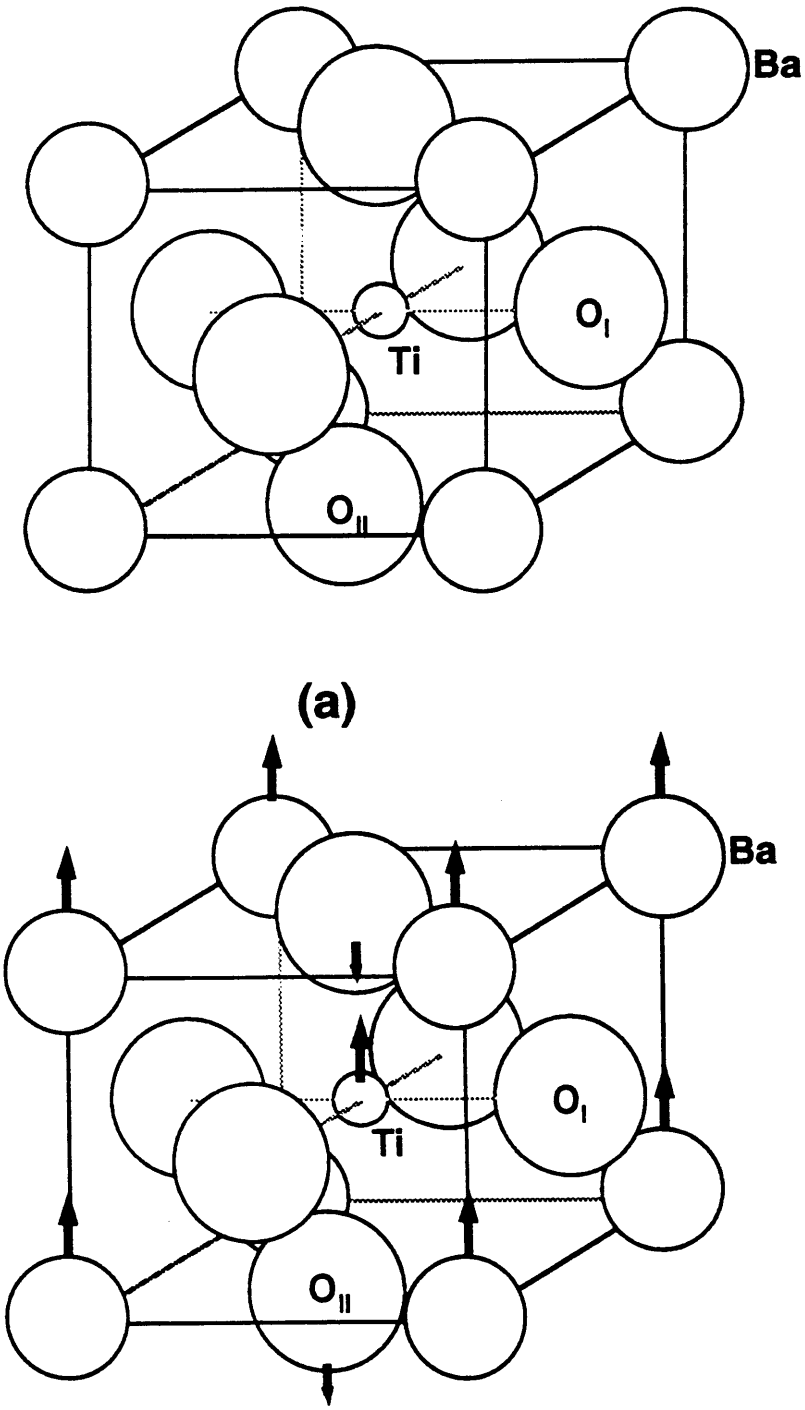

Figure 2.7: Atomic sites in tetragonal $BaTiO_3$ in the cubic (a, above 130 °C) and polar tetragonal (b, room temperature) phases. After Kittel [52], p. 377.

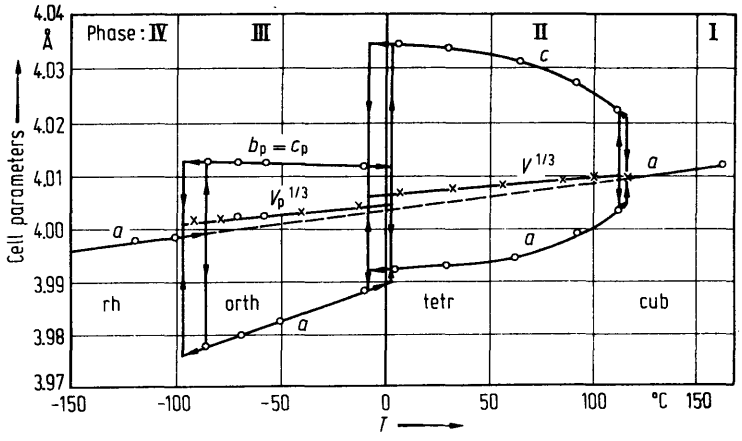

Figure 2.8: Lattice dimensions as functions of temperature in $BaTiO_3$. After [53].

λ	n_o	n_e
488 nm	2.52	2.45
515 nm	2.49	2.42
633 nm	2.42	2.36

Table 2.1: Table of refractive index values at room temperature. After Johnston [54].

to scatter which makes the beam paths in these crystals visible) are not properly material parameters. However, these may be inextricably linked in measurements, at least until measures to eliminate their effects are implemented.

2.2.2 Refractive index

Barium titanate is a birefringent material; optical beams polarized perpendicular to the **c** axis of the crystal see the ordinary index of refraction, others see an extraordinary index which depends on the exact polarization angle. The ordinary and extraordinary refractive indices for light polarized along the axes were measured by Johnston [54] (flux-grown crystals) and by Wemple et al. [55] (melt-grown crystals); their values agree to within a few percent. In addition, Johnston prepared melt-grown samples and obtained close agreement with the value for his flux-grown "butterfly wings." Johnston's values are reproduced in table 2.1 for commonly used laser wavelengths.

The temperature dependence of the index of refraction is cited in section 3.3 below; that measurement was made in a small single-domain region within an unpoled crystal by Lawless and DeVries [56], and should probably be taken as an indication of the temperature variation only. Johnston speculates that inaccuracy in measurement method may be the cause of the difference between his results and Lawless'.

As is the case for many properties of $BaTiO_3$ definitive modern measurements on high-quality, high-purity single-domain single crystals are not available; but Wemple's and Johnston's index values agree closely.

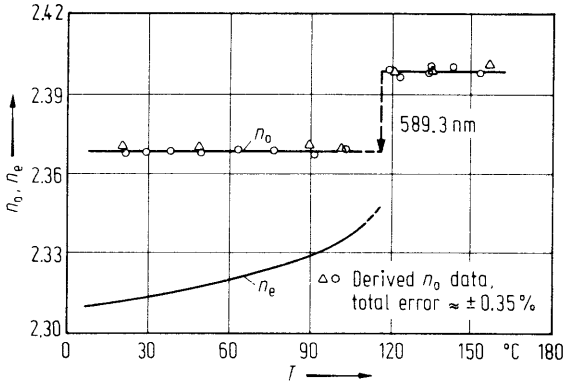

Figure 2.9: Ordinary and extraordinary indices of refraction in $BaTiO_3$ as functions of temperature. $\lambda = 589.3$ nm. After Lawless and DeVries [56].

2.2.3 Dielectric constants

Because of interference by piezoelectric effects, crystal dimensions in $BaTiO_3$ change with externally applied fields, indicating that strain (compression or expansion of the lattice) arises under these conditions, at least at low frequencies. Since "bulk" electrooptic measurements are conducted by applying an electric field to a finite sample, where the sample is free to change its dimensions, these are normally nearly *stress*-free (no net forces applied to the crystal) rather than strain-free (no net distortion of the lattice). In order to measure a strain-free value, the crystal must be physically "clamped" in all directions, so that all components of the strain are zero. Clamped measurements are usually conducted at very high frequencies (hundreds of MHz), in order to combat piezoelectric expansion, which occurs more slowly than this. Unclamped measurements are made at lower frequencies, usually below 1 MHz, where the crystal is free to expand and contract under an applied field. More complete discussion of these issues can be found in [57, p. 183].

The clamped and unclamped values of the dielectric constant along the principal axes of $BaTiO_3$ are fairly well reported. Since expansion or compression of a crystal (strain) under an applied field can affect the polarization arising from that field, particularly in a polar crystal, the clamped and unclamped values show significant differences.

These values were measured by Wemple et al. [55] for melt-grown crystals over a broad range of temperatures below T_C, and are reproduced in figure 2.10.

The value $\epsilon_c = 109$ is from Berlincourt and Jaffe [58], whose value seems in closer agreement with commonly cited results, but since the dielectric constant may depend significantly on impurity concentration [59], the dielectric constants for each crystal should ideally be measured if time and facilities are available.

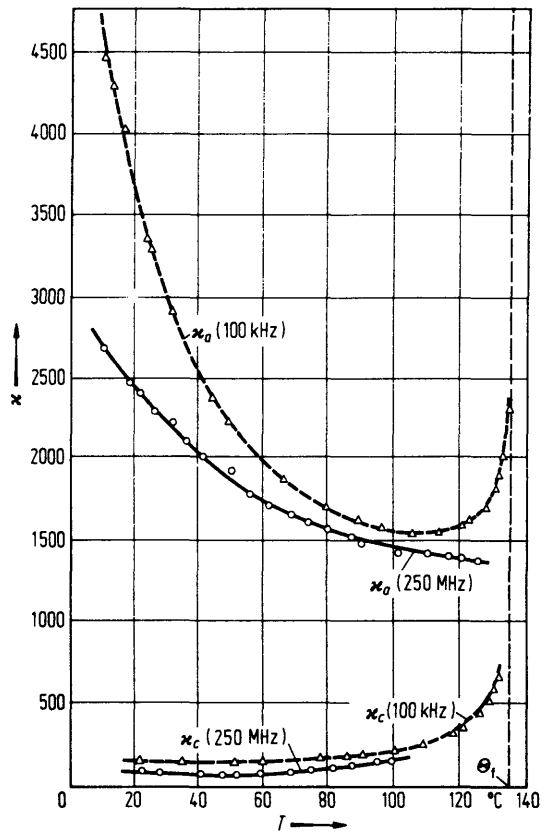

Figure 2.10: Variation of $BaTiO_3$'s dielectric constants with temperature. After [55].

2.2.4 Pockels effect

The Pockels (linear) electrooptic effect is an electric-field-induced modulation of the refractive index. Because the electric field has a definite orientation on which this effect depends (for example, making the field negative clearly makes the modulation negative), it appears only in noncentrosymmetric media. The refractive index modulation which appears due to the applied is nearly linear in the applied field (actually the value $\kappa = 1/\epsilon$ at the optical frequency is modulated linearly, where the index n is proportional to $1/\kappa^{\frac{1}{2}}$).

Zgonik et al. have noted that mechanical clamping due to the surrounding crystal can modify the effective electrooptic coefficients, necessitating use of the piezo-optic tensor for strictly accurate calculations. Unfortunately not all elements of that tensor have not been measured with high accuracy at this time [60]. Glass (in [25, ch. 7]) has pointed out that in grating applications where the electric field shows rapid spatial oscillation, adjacent portions of the grating are essentially free to expand and contract *in the direction of the periodicity,* so unclamped measurements are probably closer than the unclamped values for our purposes.

Clamped and unclamped values for the electrooptic coefficients are given in table 2.3. Variation of electrooptic coefficients with temperature is indicated in Fig. 2.11.

The unclamped electrooptic coefficients r_{33} and r_{13} in the tables are taken from the paper by Ducharme and Feinberg [61] in recent experiments which eliminate space-charge fields and piezoelectric expansion from consideration. They report very little change in measured values from 10 Hz to 10^5 Hz, which is consistent with a good measurement of the unclamped value. Those authors do not report measurements of r_{42} however. The unclamped coefficient r_{42} was measured by Johnston, as given in

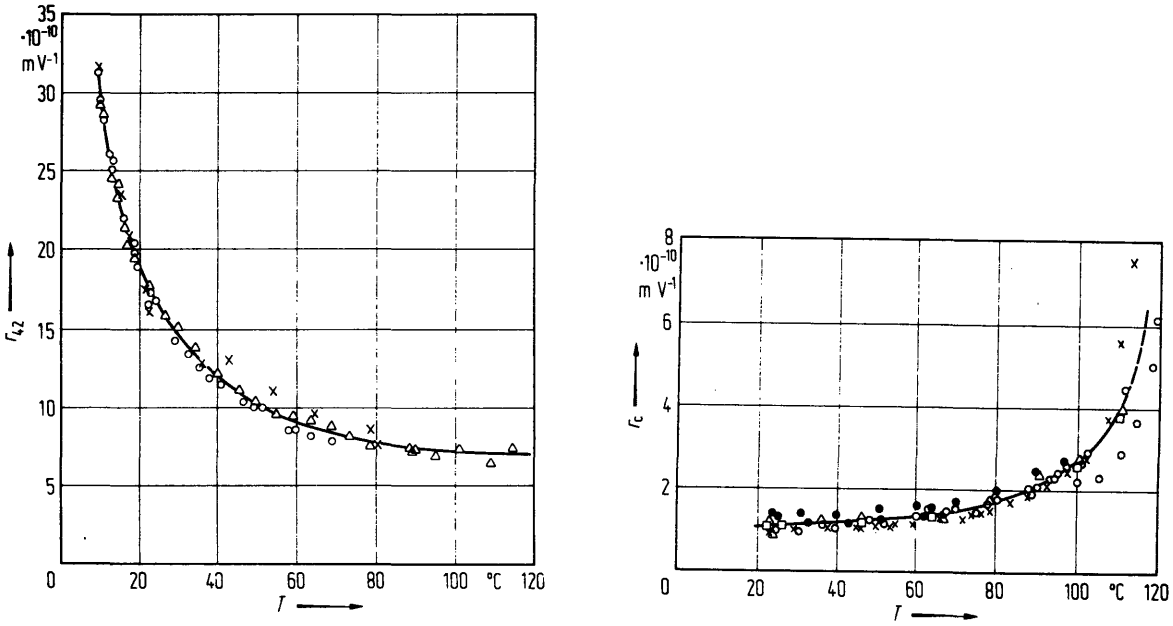

Figure 2.11: Pockels coefficients vs. temperature. After Wemple [55].

$$\begin{pmatrix} 0 & 0 & r_{13} = 19 \pm 1 \\ 0 & 0 & r_{13} \\ 0 & 0 & r_{33} = 97 \pm 7 \\ 0 & r_{42} = 1640 & 0 \\ r_{42} & 0 & 0 \\ 0 & 0 & 0 \end{pmatrix}$$

Table 2.2: (a) Unclamped values of the electrooptic coefficients in $BaTiO_3$. All quantities have dimensions of pm/V.

$$\begin{pmatrix} 0 & 0 & r_{13} = 8 \\ 0 & 0 & r_{13} \\ 0 & 0 & r_{33} = 28 \\ 0 & r_{42} = 820 & 0 \\ r_{42} & 0 & 0 \\ 0 & 0 & 0 \end{pmatrix}$$

Table 2.3: (b) Clamped values of the electrooptic coefficients in $BaTiO_3$. All quantities have dimensions of pm/V.

[53]. A value from which r_{33} and r_{13} are derived have been measured by Godefroy and co-workers, in measurements which eliminate space-charge fields but not piezoelectric expansion [59], and clamped values are from measurements reported by Johnston [62] and Kaminow [63]. Johnston's clamped values are the most commonly cited, particularly for r_{42}, although they were conducted on impure, incompletely poled crystals, grown by a method which is no longer used (flux-grown "butterfly wings").

No recent (*i.e.*, pure, single-crystal) published results could be found on the clamped values of the electrooptic coefficients in $BaTiO_3$, but the large difference between the clamped and unclamped values indicates that a majority of the observed unclamped electrooptic effect in $BaTiO_3$ is probably a result of field-induced strain rather than (much faster) electronic effects within the unit cells of the crystal.

2.2.5 Other mechanical and dielectric properties

The piezoelectric [61, 53] coefficients, quadratic electrooptic coefficients below [53] and above [64] the Curie temperature T_C have been measured in $BaTiO_3$. The quadratic electrooptic coefficient is interesting because of the possibility of fast (*i.e.*, high photoconductivity due to high temperature) photorefractivity at high temperatures using moving gratings in quadratic electrooptic materials [65]. The quadratic electrooptic coefficient is large above the Curie point (about $7 \times 10^{-12} cm^2/V^2$), which unfortunately seems to decrease rapidly with increasing temperature. Below T_C the quadratic electrooptic coefficients are one to two orders of magnitude larger than this [53] and should therefore be considered in analyses of photorefractive and other electrooptic phenomena in $BaTiO_3$.

2.2.6 Electronic transport

Barium titanate can be prepared as a p-type or n-type material. The samples used in this study were almost all p-type due to acceptor doping, background acceptor impurities, and relatively high oxygen partial pressure during growth in air. $BaTiO_3$ has a wide bandgap (about 3.1 eV at room temperature), making it ideal for use with short-wavelength visible light as long as the dopant-induced absorption is sufficiently low to allow efficient light transmission.

The photoconductivity and dark conductivity of $BaTiO_3$ crystals can be modified by varying growth conditions, purity and post-processing (oxidation and reduction during annealing) [61, 66, 33]. In particular, the photoconductivity is not linear with intensity but in general fits an empirical expression

$$\sigma(I) = \sigma_{dark} + \sigma_0 \left(\frac{I}{I_0}\right)^x, \tag{2.32}$$

where I_0 and x are experimentally measured parameters. This sublinear intensity dependence of the photoconductivity is due to filling of shallow traps at high intensities, reducing the carrier lifetime. The reasons behind this behavior have been discussed quantitatively by Mahgerefteh and Feinberg [67] and Tayebati [68]; the power-law variation is only a convenient interpolation relationship.

2.2.7 The bulk photovoltaic effect

In the bulk photovoltaic effect in polar crystals, anisotropic generation of carriers with a preferred initial velocity in a constant direction is believed to result in a net photocurrent [69, 34, 35]. The current is easily measured, and more details on the effect will be given in section 4.1.1, where these measurements are conducted for the crystal used to build the prototype P-BOD.

2.2.8 Selection of barium titanate for hologram fixing experiments

In general, materials with large linear electrooptic coefficients tend to provide large photorefractive nonlinearities (high Δn), and materials with high photoconductivities tend to be fast (small $\tau_{di} = \epsilon_0 \epsilon / \sigma$, where τ_{di} is the dielectric relaxation time and σ is the conductivity including photoconductivity). Similarly, materials with low dark conductivities have long dark storage times. In addition to this, a photorefractive medium's usefulness is limited by its absorption coefficient α, measured in cm^{-1}. If α is too high then a photorefractive material clearly cannot provide any net beam coupling gain; at some point, the detected output power is too low to measure accurately and the signal is lost entirely.

$BaTiO_3$ has very large electrooptic coefficients and low absorption at red and infrared wavelengths, making it one of the most promising materials for nonvolatile

storage of high-diffraction-efficiency volume phase holograms. To this end, several workers have demonstrated techniques for fixing holograms in $BaTiO_3$ [8, 16]. Electrical fixing in $BaTiO_3$ was first demonstrated by Micheron and Bismuth [8] as well as in strontium barium niobate (SBN) [17]. They used a four-step technique: (1) a photorefractive hologram was written to saturation in a poled crystal; (2) a negative (opposite to the sense of the poling field) voltage pulse exceeding in magnitude the coercive field for ferroelectric switching ($\sim$ -1 kV/cm) was applied to form a fixed compensating secondary grating, resulting in a lowered diffraction efficiency as primary and secondary gratings cancelled out; (3) the crystal was illuminated uniformly to redistribute the carriers of the primary grating, revealing a fixed grating with a high diffraction efficiency; (4) erasure was accomplished by applying a positive repoling field which was several times the coercive field of the crystal. Micheron and Bismuth reported much higher diffraction efficiencies in SBN than in $BaTiO_3$, but recent workers have had difficulty achieving these values [18].

In $BaTiO_3$, fixing has also been accomplished by heating crystals to about 100°C without any applied field by Kirillov and Feinberg [16]. Kirillov and Feinberg have argued that the secondary grating in the thermal cycling experiments were ions [16], but did not report any attempts to erase their fixed gratings by applying an electric field. Practical problems encountered in their pioneering work led to low fixed-hologram diffraction efficiencies, and the most effective crystals used were of unknown composition [16].

The research reported in this dissertation confirms that thermal fixing can be effective in iron- and nickel-doped $BaTiO_3$, The orientations explored were limited by geometrical considerations in our original setup; we expect to see significant improvement in diffraction efficiency when the optimal orientation is found. Further, we

have noticed that the writing intensity can be varied to enhance the diffraction efficiency of the fixable holograms. By optimizing crystal composition, reduction state, orientation, writing temperature, writing intensity, readout/storage temperature and applied electric fields, we hope to obtain diffraction efficiencies in excess of 30% and storage times of months to years.

It is worth noting that thermal fixing processes generally have the following disadvantage: during high-temperature writing to update a fixed hologram, all other holograms stored in the same crystal begin to decay. Therefore, thermal fixing processes developed to date are most suitable for read-only applications. Electrical fixing also has the advantage of room-temperature operation; but application of electric fields can cause cracking near the electrodes in many ferroelectrics, limiting crystal lifetime.

Lithium Niobate ($LiNbO_3$) exhibits considerably higher fields than $BaTiO_3$ [34] (in fact, fields above the breakdown strength of the material can be generated). However, the photorefractive effect in $LiNbO_3$ is slow due to a low photoconductivity, and these fields take a relatively long time to develop [70]. BSO and similar cubic crystals such as BGO and BTO ($Bi_{12}TiO_{20}$), and the cubic semiconductors GaAs and InP, are fast, but have low linear electrooptic coefficients. In addition, the semiconductors exhibit high optical absorption even in the infrared, where they operate. $BaTiO_3$ a material with moderate speed but very high electrooptic coefficients and very low absorption in pure and appropriately reduced samples, was chosen as the active medium. Local materials science expertise in photorefractive $BaTiO_3$ and a large number of available samples for experimentation contributed to the effectiveness of this research.

Chapter 3

DEFECT CHEMISTRY

3.1 Overview

To optimize a photorefractive material for fixed hologram storage, we wish to control the ionic conductivity. At sufficiently low ion concentrations, the ionic contribution to the conductivity is given by the expression

$$\sigma_I = q_I N_I \mu_I. \tag{3.1}$$

Here q_I, N_I and μ_I are, respectively, the ionic charge, concentration and mobility. We need a dopant that efficiently produces mobile ions (for example, acceptors in $BaTiO_3$ are largely compensated by oxygen vacancies). Those vacancies also need to be free to move over long distances (hundreds of nanometers). Thus ions that are strongly associated with compensating defects do not contribute to the ionic conductivity. In addition, the mobility activation energy of the ions should be as high as possible, so that room-temperature storage time is maximized. Finally, the dopant must not ruin the photonic properties of the host material. Dopants can do that in at least two ways: high absorption and carrier trapping.

In this chapter, an attempt will be made to understand why Fe and Ni doping increase σ_I, and why reduction treatment can increase σ_I by orders of magnitude in

Fe-doped crystals. Conversely, we would like to understand why undoped crystals and crystals doped with Co, Rh, and V have very low σ_I, and in particular why even heavily-reduced $BaTiO_3$:Co (10^{-16} atm) has no measurable ionic conductivity.

3.2 Defect Chemistry of Acceptor-Doped $BaTiO_3$

The main assumption of this section is that oxygen-vacancy conductivity in as-grown and moderately-reduced acceptor-doped $BaTiO_3$ below 130°C is due to singly-ionized oxygen vacancies, a minority species. Oxygen vacancies in $BaTiO_3$ are donors. They can be neutral, singly-ionized (+1), or doubly-ionized (+2).[1] We expect $V_O^{\bullet}$ to be much more mobile than $V_O^{\bullet\bullet}$ in acceptor-doped material, at least at low temperatures. This is because, from coulombic considerations, $V_O^{\bullet}$ should form much weaker associations with acceptor impurities than $V_O^{\bullet\bullet}$. It has been found in absorption studies [72, 73] that doubly-ionized oxygen vacancies probably do associate with acceptors, specifically with Co^{3+}. (However, different +3-charge acceptor dopants in $SrTiO_3$ lead to different ion mobility activation energies [74]. This suggests that the association energy between an oxygen vacancy and an acceptor depends on more than coulombic attraction.) Since $V_O^{\bullet}$ is a minority species, the difference in association energies ΔE_{assoc} between $V_O^{\bullet}$ and $V_O^{\bullet\bullet}$ would have to be significant to allow $V_O^{\bullet}$ to dominate the conductivity. Assuming $[V_O^{\bullet\bullet}]/[V_O^{\bullet}] = 10^4$,

$$\Delta E_{\text{assoc}} > kT \ln(10^4) \times 0.3eV. \tag{3.2}$$

Association energies of $V_O^{\bullet\bullet}$ and $V_O^{\bullet}$ with Fe^{3+} and Ni^{2+} in $BaTiO_3$ were not found in the literature.

[1] We use Kroger-Vink notation [71], where $'$, $^{\bullet}$, and $^{\times}$ superscripts stand for -1, +1, and 0 charge with respect to the ionization state of the atom normally occupying the lattice site in question. For example, Fe^{3+} on a titanium (Ti^{4+}) site is written Fe'_{Ti}. A doubly ionized vacancy on an oxygen site is written $V_O^{\bullet\bullet}$ Concentrations are indicated by square brackets. For example, $[Fe''_{Ti}]$ stands for the concentration of Fe^{2+} on Ti^{4+} sites.

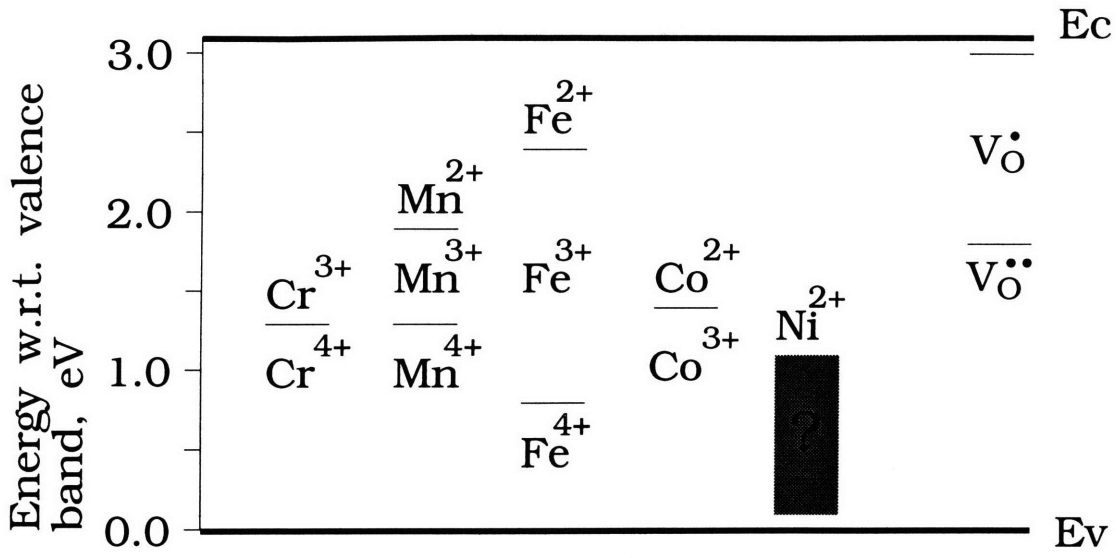

Figure 3.1: Schematic diagram of the energy levels used in defect chemistry calculations. In addition to the ionization energies shown, the formation energy for new oxygen vacancies is 4.7 eV. The energy of the Ni^{3+} level is unknown. (see Table 3.2).

Obtaining a large population of oxygen vacancies requires acceptor doping to produce compensating oxygen vacancies. In order to produce mobile $V_O^\bullet$ centers, we also need a Fermi level near the middle of the bandgap (see Fig. 3.1). This allows a significant number of oxygen vacancies to capture electrons, according to the reaction

$$V_O^\bullet \rightleftharpoons V_O^{\bullet\bullet} + e. \tag{3.3}$$

Acceptors (Fe, Co, Ni, Cr and Mn on Ti sites are examples) vary in their usefulness for producing the minority species $V_O^\bullet$. This is because all midgap states must be filled with electrons before the donor level $V_O^{\bullet\bullet}$ can begin to fill. Thus acceptors that have empty states near mid-gap (below the oxygen-vacancy levels) require much heavier reduction before $[V_O^\bullet]$ becomes significant.

This model also allows us to predict the effect of reduction and oxidation treatments on the ionic conductivity. Reduction raises the Fermi level toward the conduction band, boosting $[V_O^\bullet]$ and increasing the ionic conductivity. Oxidation treatment lowers

the Fermi level, thus reducing $[V_O^{\bullet}]$ and lowering ionic conductivity. In this section, quantitative support for these conclusions is presented.

The defect chemistry of sintered $BaTiO_3$ was investigated by Hagemann and Hennings using thermogravimetric measurements [75] and magnetic susceptibility measurements [76]. Schunemann et al. [77] investigated the application of Hagemann's model to single-crystal photorefractive $BaTiO_3$. Following their work, we can estimate the total oxygen vacancy concentration in acceptor-doped $BaTiO_3$. First of all, it is normally assumed that in p-type $BaTiO_3$, the majority species of oxygen vacancies is $V_O^{\bullet\bullet}$. This assumption allows us to conclude that:

1. Each 2 incorporated Fe atoms generate one oxygen vacancy in the as-grown to moderately-reduced states (10^{-10}–1 atm partial pressure O_2).

2. Each incorporated Ni atom generates one oxygen vacancy under the same conditions.

3. Each 2 Co atoms produce an oxygen vacancy.

Comparison with experiments conducted in the course of this thesis research shows that not all oxygen vacancies are mobile, however. For example, no ionic conductivity was detected ($< 10^{-14}(\Omega cm)^{-1}$) in $BaTiO_3$ doped with 50 ppm Co. In addition, a 1000 ppm Fe-doped crystal reduced in 10^{-4} atm O_2 at 800°C was found to have an ionic conductivity nearly 3 orders of magnitude higher than the that of an as-grown Fe-doped crystal taken from the same boule. Since concentrations of the majority species Fe' and $V_O^{\bullet\bullet}$ are insensitive to such moderate reduction and oxidation differences [78, 76], this experimental result strongly suggests that the ionic conductivity is due to a minority species. In earlier experiments the as-grown 1000 ppm Fe crystal showed color front motion due to drift of oxygen vacancies [35], so the minority

Reaction			Mass action equation			Eq.
O_O^x	$\rightleftharpoons$	$\frac{1}{2}O_2(gas) + V_O^{\times}$	$[V_O^{\times}]P_{O_2}^{1/2}$	=	$K_O \exp(-E_0/kT)$	(1)
V_O	$\rightleftharpoons$	$V_O^{\bullet} + e$	$[V_O^{\bullet}]n/[V_O^{\times}]$	=	$N_C \exp(-E_1/kT)$	(2)
$V_O^{\bullet}$	$\rightleftharpoons$	$V_O^{\bullet\bullet} + e$	$[V_O^{\bullet\bullet}]n/[V_O^{\bullet}]$	=	$N_C \exp(-E_2/kT)$	(3)
Fe'_{Ti}	$\rightleftharpoons$	$Fe_{Ti}^{\times} + e$	$[Fe^{\times}]n/[Fe']$	=	$2N_C \exp(-E_3/kT)$	(4)

Table 3.1: Defect-chemical reactions describing acceptor-doped $BaTiO_3$.

species responsible is probably singly ionized oxygen vacancies, $V_O^{\bullet}$.

Table 3.1 lists the reactions normally considered in defect chemistry models of acceptor-doped $BaTiO_3$ [79, 77, 80, 81]. In addition to the mass-action formulas listed in Table 3.1, creation of electron-hole pairs must be considered:

$$\text{nil} \rightleftharpoons e + h, \tag{3.4}$$

$$np = N_C N_V \exp(-E_g/kT). \tag{3.5}$$

where E_g is the thermal bandgap.

Assuming that $[Fe^{2+}] = [Fe'']$ is negligible [76, 77], the total iron concentration $[Fe]_{\text{tot}}$ is a constant that satisfies

$$[Fe]_{\text{tot}} = [Fe'] + [Fe^{\times}]. \tag{3.6}$$

Finally, charge balance must be satisfied:

$$n + [Fe'] = p + [V_O^{\bullet}] + 2[V_O^{\bullet\bullet}]. \tag{3.7}$$

(For the iron-doped crystals at the temperatures and partial pressures studied, the charge balance equation could be approximated by

$$[Fe'] \simeq 2[V_O^{\bullet\bullet}]. \tag{3.8}$$

Constant	Value	Reference
K_0	1.2×10^{31} cm^{-3}Pa$^{1/2}$	[76]
E_0	4.7 eV	[80]
E_1	0.1 eV	[80]
E_2	1.3 eV	[80]
E_3	2.4 eV	[77]
E_g	3.1 eV	[76]
N_C	1.6×10^{22} cm^{-3}	[76]
N_V	5×10^{22} cm^{-3}	[80]

Table 3.2: Constants used in the defect chemistry model of $BaTiO_3$:Fe.

Eq. (3.8) is a valid approximation to Eq. (3.7) at moderate reduction levels (approx. 10^{-10} to 1 atm) because electrons, holes and singly-ionized oxygen vacancies are minority species under these conditions.)

Once the constants K_0, E_0, E_1, E_2, E_3, E_g, N_C, N_V, and $[Fe]_{\text{tot}}$ are known, we have seven equations [Table 3.1 and Eqs. (3.5–3.7)]. This system can be solved for the seven concentrations $[Fe']$, $[Fe^{\times}]$, $[V_O^{\times}]$, $[V_O^{\bullet}]$, $[V_O^{\bullet\bullet}]$, n, and p. The values used for the constants $K_0 ... N_V$ are given in Table 3.2 (for Fe-doped $BaTiO_3$). The resulting numerical problem (finding the positive real root of a sixth order polynomial) is easily solved by computer for a given temperature, oxygen partial pressure, and acceptor concentration. Results of the computer calculations are shown in Figs. 3.2–3.6.

The central prediction of the defect chemistry solutions is that $[V_O^{\bullet}]$ (assumed to be the mobile ion concentration) is highest in Fe and Ni doped crystals treated at moderately low PO_2 (see Fig. 3.2). Fig. 3.3 shows in detail that a much higher level of reduction is necessary to obtain high $[V_O^{\bullet}]$ in samples doped with Co. Finally, the complete defect chemistry solutions for 1000, 50, and 1 ppma of Fe, Co and Ni in $BaTiO_3$ are plotted in Figs. 3.4, 3.5 and 3.6. (Species with concentrations less than 10^{10}cm^{-3} are not shown in those plots.) No ionization energy data were available

for $BaTiO_3$:Ni, but Hagemann and Ihrig found that the dominant valence state of Ni remained +2 from 10^{-22} to 150 atm PO_2 [76]. The calculations presented here for $BaTiO_3$:Ni were based on the assumption that the Ni levels are so close to the valence band that the Ni atoms are effectively all in the +2 state.

The results of the calculations agree qualitatively with the experimental data, suggesting that Ni is the most effective dopant (requires least reduction), and Co and undoped crystals require such heavy reduction that the crystal may become semiconducting (resulting in high absorption and very poor photorefractive response).

There are several sources of error in the defect chemistry model. Uncertainty of the bandgap and ionization energies used in the model makes unpredictable the exact PO_2 of the abrupt transitions from low to high $[V_O^{\bullet}]$. The relative locations of those transitions for different dopants should be qualitatively correct, however. For example, in $BaTiO_3$:Co nearly all Co^{3+} must be filled with electrons (becoming Co^{2+}) before significant quantities of $V_O^{\bullet}$ can be produced (see Fig. 3.1). Conversely, $BaTiO_3$:Fe and $BaTiO_3$:Ni have far fewer empty states between the as-grown Fermi energy and the ionization energy of the oxygen vacancies. Thus the Fermi level is much more easily raised by reduction in as-grown $BaTiO_3$:Fe and $BaTiO_3$:Ni than in as-grown $BaTiO_3$:Co. This has been borne out by experiments [75, 76].

Another source of error is contamination, inevitably present at levels $\geq$ 1 ppm in real samples. A related problem is the probable broadening of the density of states of the bands and the impurity levels due to inhomogeneities in the material (such as electric and strain fields sourced by dopant ions) [35, 82]. The effect of a spread of ionization energies within the bandgap would be to make the transitions between different charge compensation regimes less abrupt. In other words, the vertical "stair steps" where concentrations change by several orders of magnitude for a tiny change

in PO_2 are unrealistic. This is because the density of states does not really go to zero everywhere between the levels we have considered in our model. In real samples, the "stair steps" would look more like a series of small steps (due to additional discrete states in the bandgap) or gradual ramps (due to a continuous distribution of states).

The presence of unidentified "background acceptors" found in most defect studies of $BaTiO_3$, typically at concentrations around 100 ppm, [77, 79] also limits the quantitative accuracy of the defect chemistry model. Calculations were made for iron-doped $BaTiO_3$ with 100 ppm of ionized acceptors added, and the results differed little from the curves shown. (There was almost no effect in the 1000 ppm Fe case, where $V_O^{\bullet}$ is highest).

In addition, this model is only useful for predicting the ionic conductivity (σ_I) when σ_I is dominated (as assumed earlier) by mobile $V_O^{\bullet}$. The validity of this assumption is very difficult to test quantitatively. At low σ_I other ionic carriers may dominate. One case of competition between two distinct ionic species was identified in the laboratory and will be described in Chapter 5. However, the measured variation of σ_I by nearly 3 orders of magnitude with varying PO_2 implies that a mobile minority ionic species (such as $V_O^{\bullet}$) dominates at high σ_I.

The defect chemistry model predicts that the concentration of mobile ions will be effectively independent of temperature at low PO_2 but a strong function of temperature at higher PO_2. Thus the measured activation energy of the ionic conductivity may not indicate the mobility activation energy precisely but may also be affected by a varying carrier concentration. The (calculated) effect of temperature variation on $[V_O^{\bullet}]$ is shown in Fig. 3.7.

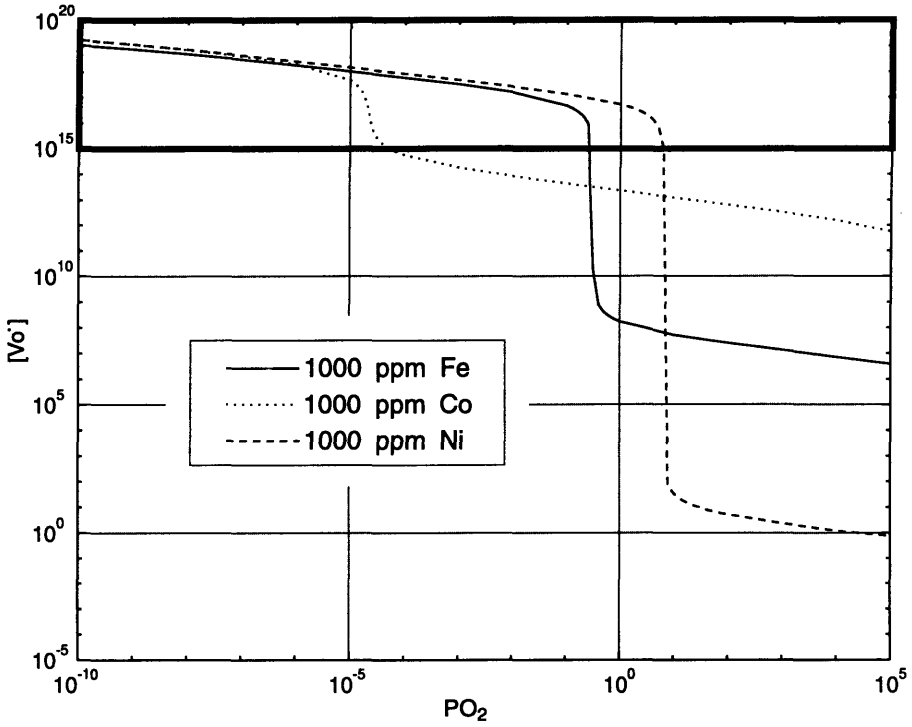

Figure 3.2: Theoretical comparison of $[V_O^{\bullet}]$ for Fe-, Co-, Ni-doped $BaTiO_3$ at 100°C vs. PO_2. The area inside the dark border roughly represents the regime where $[V_O^{\bullet}]$ is large enough to contribute measurably to the ionic conductivity. That area is shown in greater detail in Fig. 3.3. PO_2 is in Pa. Results for very low concentrations are only qualitative.

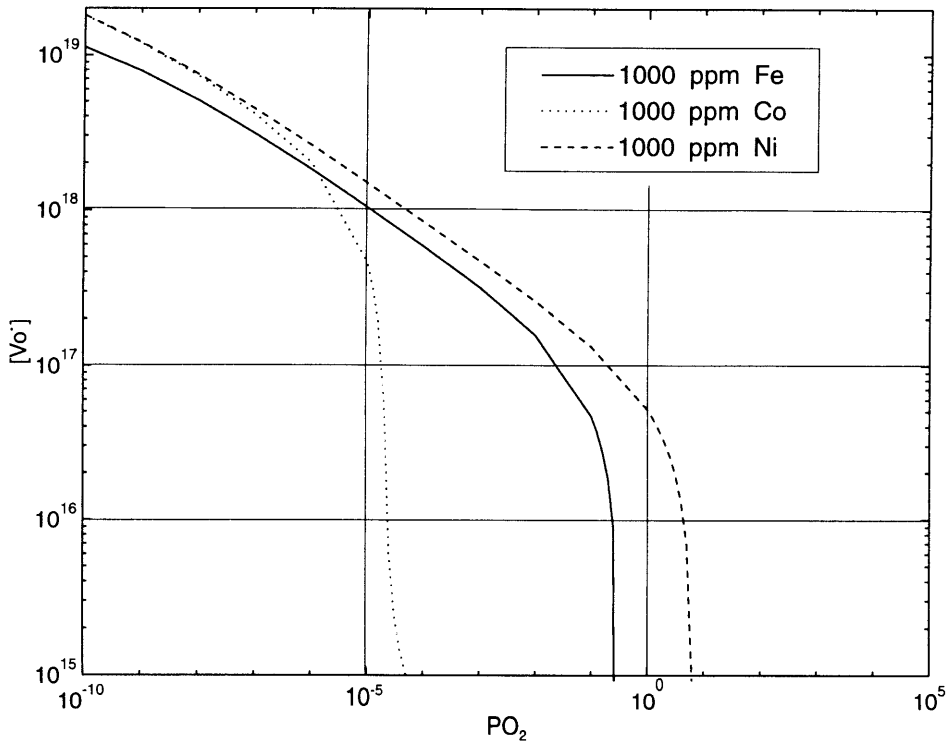

Figure 3.3: Detail of theoretical comparison of $[V_O^{\bullet}]$ for Fe-, Co-, Ni-doped $BaTiO_3$ at 100°C vs. PO_2. PO_2 is in Pa.

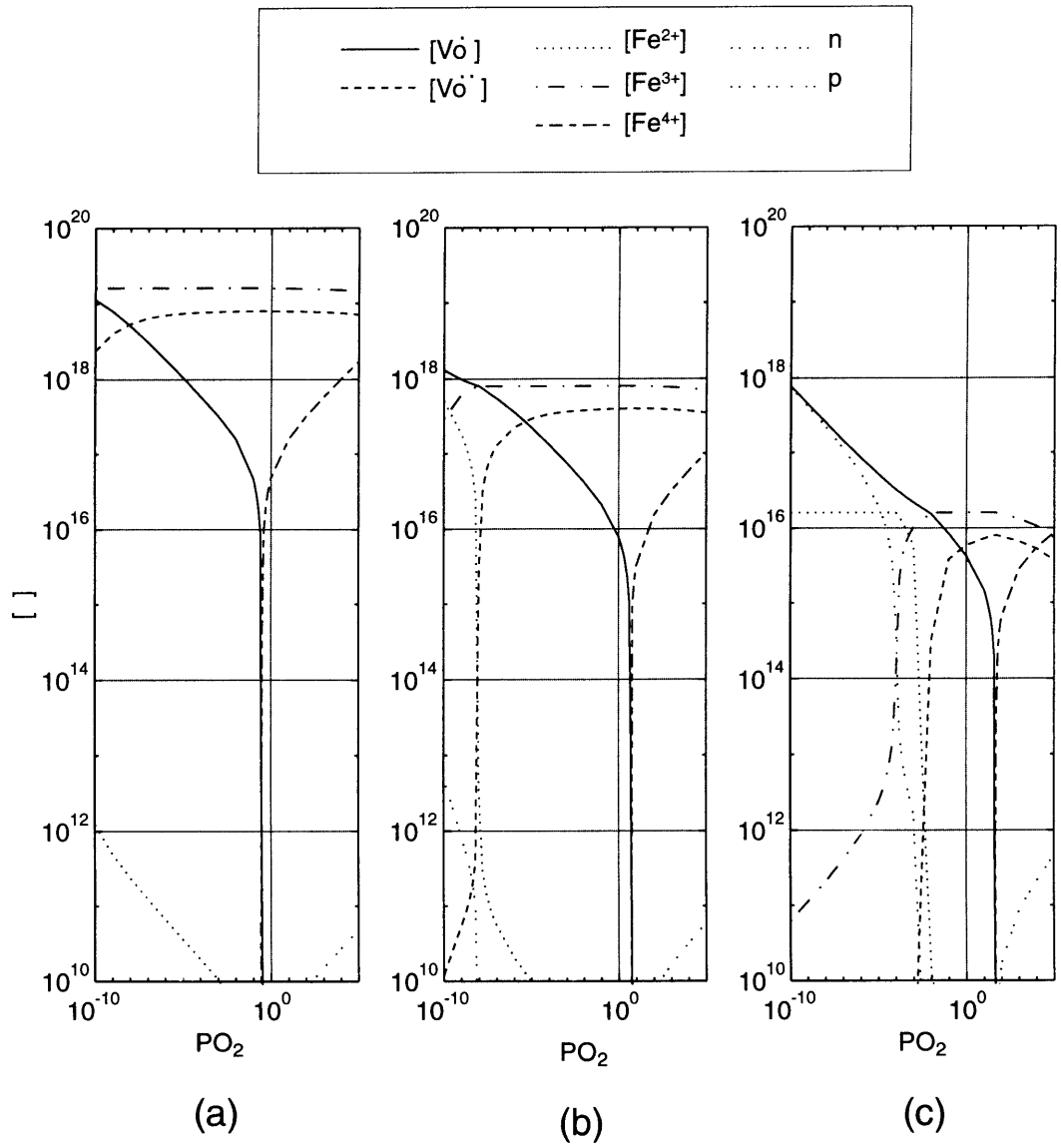

Figure 3.4: Full results of defect chemistry calculations for $BaTiO_3$:Fe, annealed at 800°C in varying PO_2 and quenched to 100°C. (a) 1000 ppma, (b) 50 ppma, (c) 1 ppma. PO_2 is in Pa.

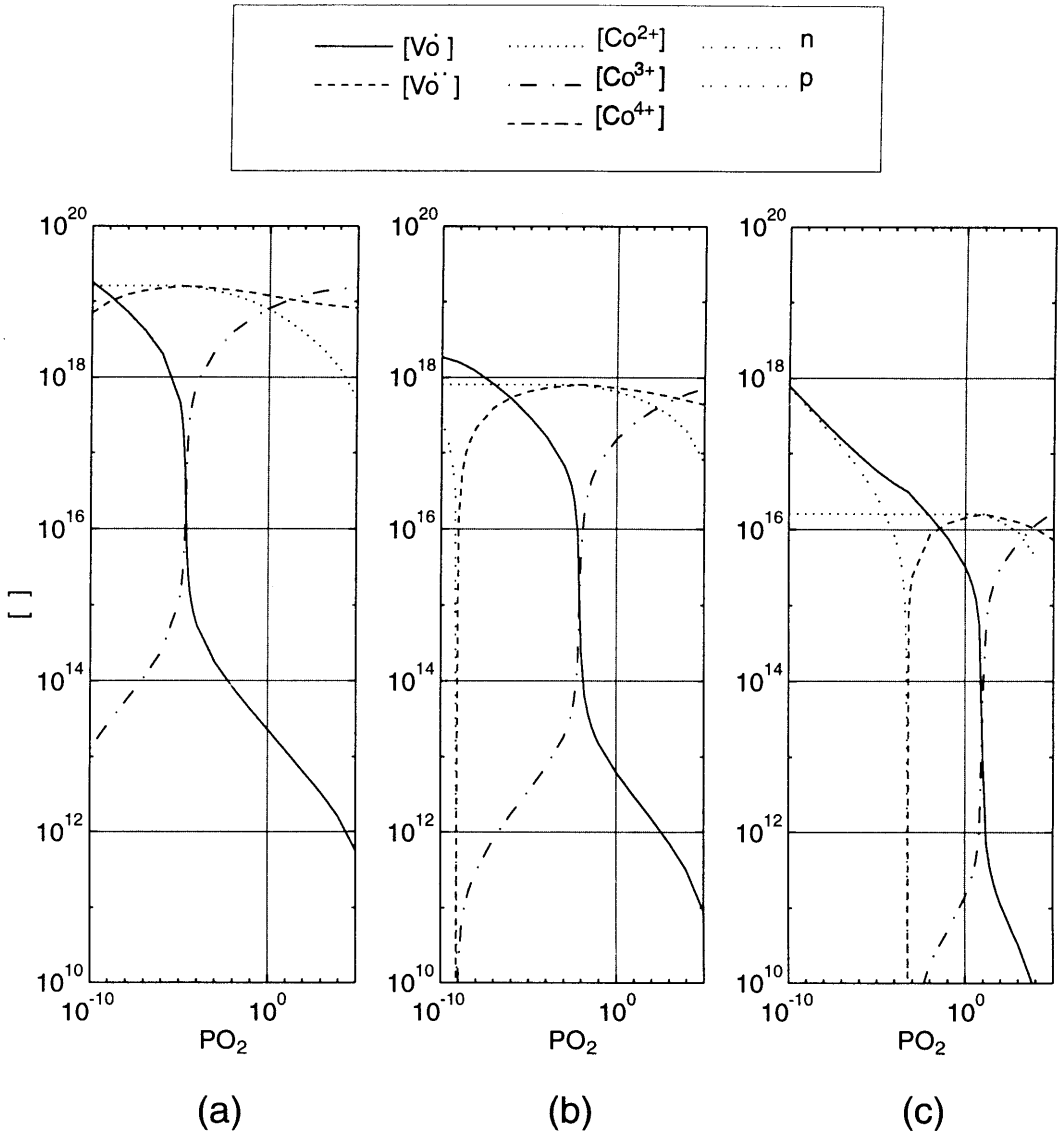

Figure 3.5: Full results of defect chemistry calculations for $BaTiO_3$:Co, annealed at 800°C in varying PO_2 and quenched to 100°C. (a) 1000 ppma, (b) 50 ppma, (c) 1 ppma. PO_2 is in Pa.

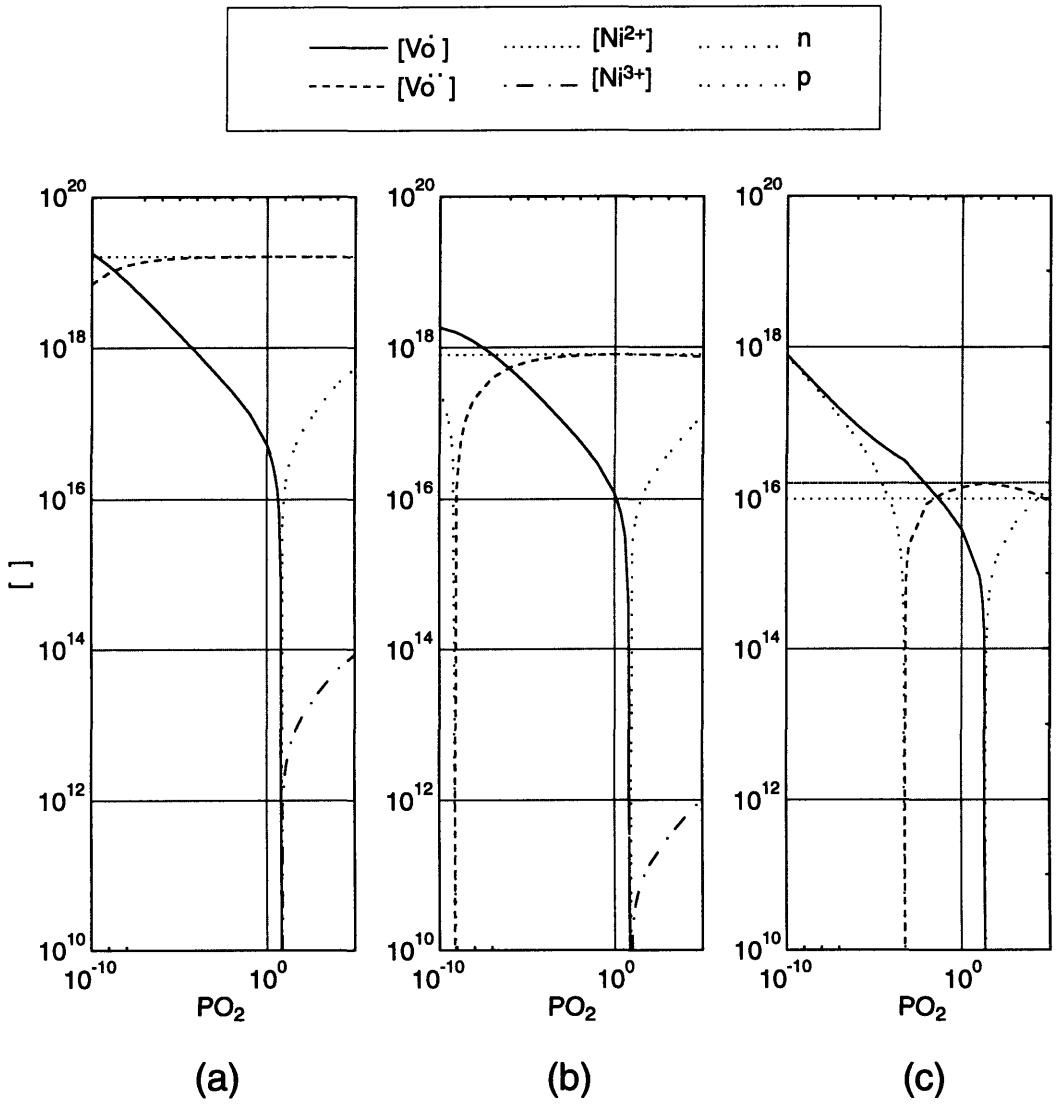

Figure 3.6: Full results of defect chemistry calculations for $BaTiO_3$:Ni. annealed at 800°C in varying PO_2 and quenched to 100°C. (a) 1000 ppma, (b) 50 ppma, (c) 1 ppma. PO_2 is in Pa.

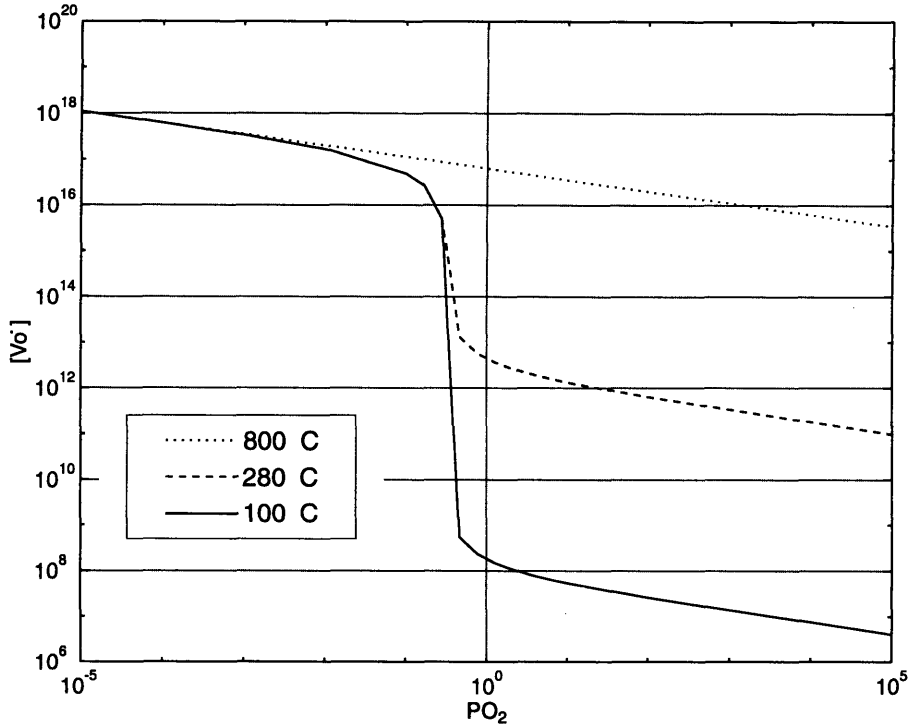

Figure 3.7: Effect of Fermi-level pinning during the quenching process (flat portions of the graph). Detail of defect-chemical calculation of $[V_O^{\bullet}]$ in $BaTiO_3$:Fe (1000 ppm) annealed at 800°C and quenched to different operating temperatures. PO_2 is in Pa.

3.3 Conclusions

We have presented a standard defect chemistry model of $BaTiO_3$. The model can explain why the ionic conductivity is very sensitive to PO_2 if we assume that the most mobile ionic charge carriers are singly-ionized oxygen vacancies. The model also sheds light on why Fe and Ni are effective dopants. Those elements leave the mid-gap region relatively free of states so that reduction treatment can easily supply electrons to doubly-ionized oxygen vacancies without wasting electrons on changing the ionization state of the dopant. Finally, as expected, pure crystals do not support large numbers of oxygen vacancies in the compensated (non-semiconducting) regime. Since photorefractive recording depends upon the semi-insulating nature of compensated crystals, obtaining high ionic conductivity simply by heavily reducing undoped or donor-doped crystals is unlikely to be useful. No ionic conductivity was measured in as-grown pure or 50 ppm vanadium (V) donor-doped $BaTiO_3$, or in reduced crystals from the same boules, in agreement with this prediction.

Finally, the model allows us to make a prediction about the ultimate ionic carrier concentration attainable for a given doping level. For the same reduced 1000 ppm Fe-doped crystal used in this study, Hathcock measured the ionic mobility by observing color front drift at 125°C [35]. From those measurements he estimated $\mu_I = 1.5 \times 10^{-9}$ cm^2/V·s. From activation energy plots presented in Chapter 5, we can estimate the ionic conductivity in the same crystal at 125°C to be $\sigma_I = q_I N_I \mu_I \simeq 1.7 \times 10^{-10} (\Omega\text{cm})^{-1}$. We can use these two results to check whether singly or doubly ionized oxygen vacancies might be present at the correct concentration to account for the observed ionic conductivity. Solving for N_I, we would need $[V_O^{\bullet\bullet}] = \sigma_I/(q_I\mu_I) = 3.5 \times 10^{17}\text{cm}^{-3}$ (here $q_I = +2|e|$). This is much smaller than

the expected concentration of the majority oxygen-vacancy species, $[V_O^{\bullet\bullet}] = \frac{1}{2}[Fe]_{\text{tot}}$ $= 8 \times 10^{18}\text{cm}^{-3}$. The concentration of iron (1000 ppm) and its dominant valence (+3) are both known accurately from impurity analysis and optical absorption data [77]. Thus we conclude that most oxygen vacancies in this crystal are immobile. If, however, we assume that the mobile ionic species is $V_O^{\bullet}$, we find $[V_O^{\bullet}] = 7 \times 10^{17}$, or about 9% of the total oxygen vacancy concentration. This conclusion is much more reasonable. We can also use this model to explain why an as-grown crystal from this boule has an ionic conductivity nearly three orders of magnitude lower than the reduced crystal just described, so that $[V_O^{\bullet}] \simeq 9 \times 10^{14}$. (The as-grown crystal is more p-type than the reduced sample so there are fewer electrons available to convert $V_O^{\bullet\bullet}$ into $V_O^{\bullet}$.) Our assumption that the ionic conductivity is due to singly ionized oxygen vacancies is consistent with the data available.

Chapter 4

FIXING THEORY

4.1 Writing fixable holograms

The setup used for holographic measurements was shown in Chapter 2, and is reproduced in Fig. 4.1.

In order to account for fixable gratings observed in $BaTiO_3$, we assume that there are two carrier types, holes and mobile ions. In this model the ionic conductivity is not affected by the light intensity: this accounts for the fact that the measured time constants of ionic gratings are not observed to vary for the intensity range studied. A picture of the ionic hologram writing process is shown in Fig. 4.2. The hole grating is written first. The space-charge field sourced by the trapped holes then drives ions to move. The ionic grating responds more slowly than the hole grating, so the diffraction efficiency reaches a relatively large value before falling off toward zero. If fixing is desired, then at this point, with the ionic grating saturated, the crystal is quickly cooled to freeze in the ionic grating.

Now we will review a quantitative model of the ionic hologram writing process. We assume that the mobile ions are positively charged. This assumption is consistent with both oxygen vacancies and hydrogen ions, two species of ions that are known to move as charge carriers in oxide crystals. Charge neutrality then requires a background of

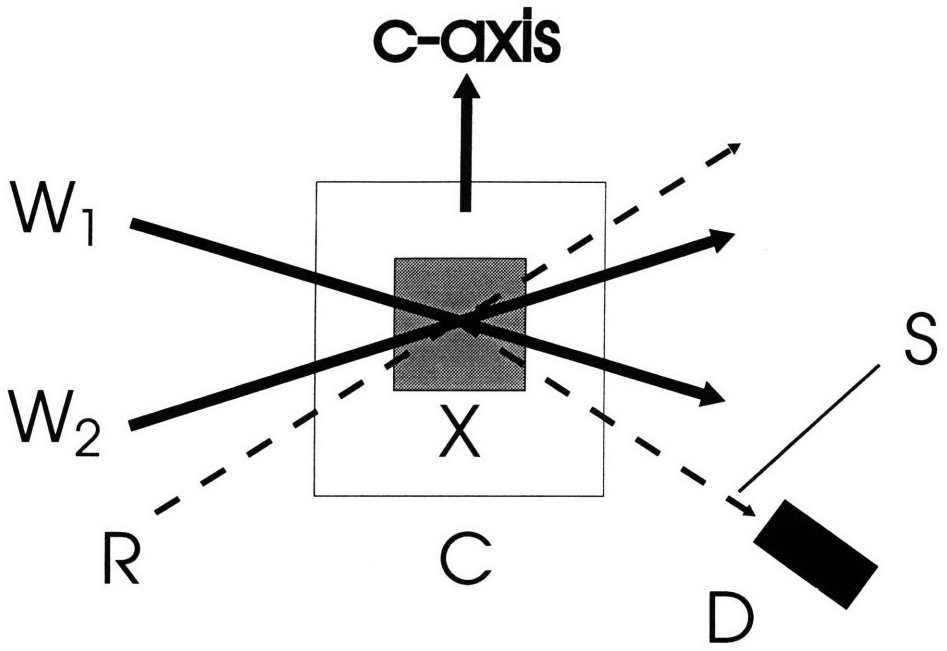

Figure 4.1: Experimental geometry for writing semipermanent holograms in $BaTiO_3$ at elevated temperatures. Legend: W_1 and W_2 are 514 nm writing beams, R is a 633 nm readout beam, S is the 633 nm beam diffracted by gratings in the crystal, F is a narrow-band interference filter centered at 633 nm, D is a detector, X is the $BaTiO_3$ crystal, and C is the temperature-controlled oil cell.

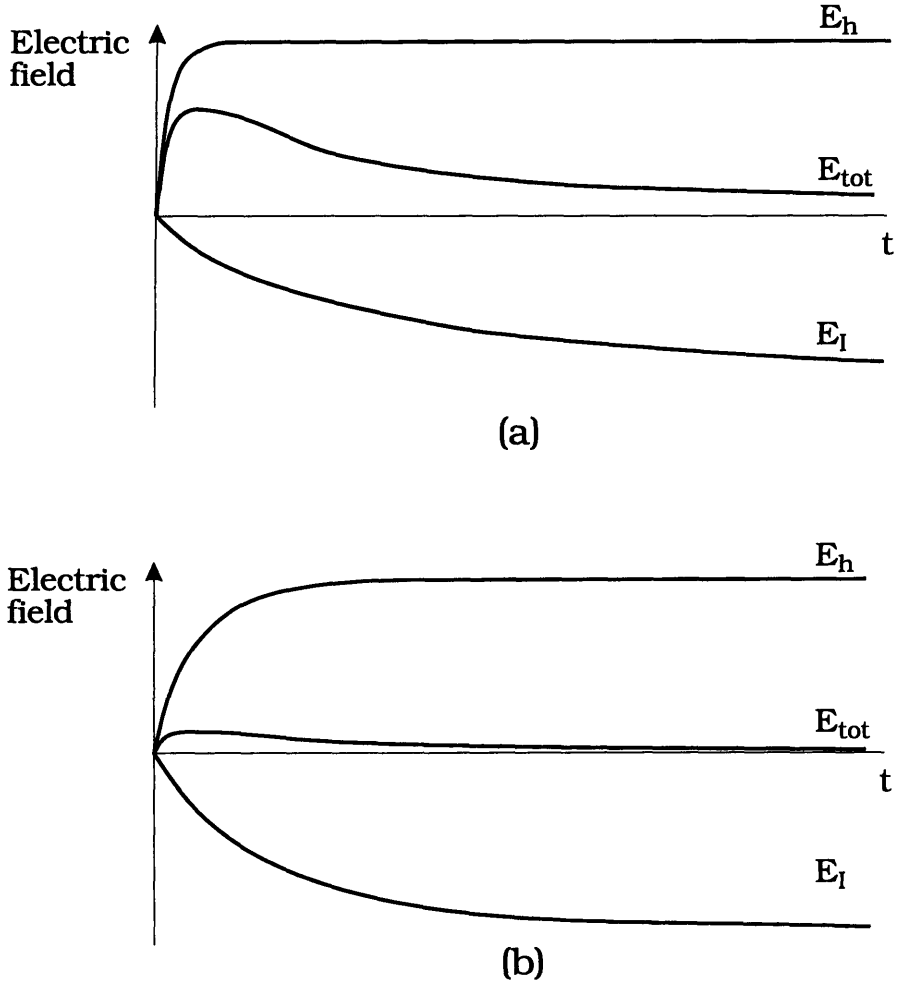

Figure 4.2: Components of the space-charge field during writing of the ionic grating. (a) $\tau_I >> \tau_h$. (b) $\tau_I \simeq \tau_h$.

negatively-charged ionized acceptors. These also function as hole traps (see Fig. 4.3). Electroneutrality is expressed by the relation

$$(N_T^-)_{\text{avg}} = (N_I^+ + p)_{\text{avg}}, \tag{4.1}$$

where the average is over the volume of the crystal. Here N_T, N_I and p are the concentrations of ionized acceptors, mobile ions, and holes, respectively.

A theoretical model of a similar ionic hologram fixing process in photorefractive potassium niobate ($KNbO_3$) was developed by Montemezzani et al. [14, 15]. The mathematical model can be written as a system of equations: (1) a rate equation for generation and trapping of holes, (2) a rate equation describing emptying and filling of traps from which the holes are excited, and (3) a continuity equation describing local accumulation of mobile ions by drift and diffusion. In the model, physical variables are assumed to change only in the x-direction, and the resulting formulas are as follows:

$$\frac{\partial p}{\partial t} = (sI + \beta)(N_A - N_A^-) - \gamma n N_A^- + \frac{1}{e}\frac{\partial J_h}{\partial x}, \tag{4.2}$$

$$\frac{\partial N_D^+}{\partial t} = (sI + \beta)(N_A - N_A^-) - \gamma n N_A^-, \tag{4.3}$$

$$\frac{\partial N_I}{\partial t} = -\frac{1}{e}\frac{\partial J_I}{\partial x}. \tag{4.4}$$

These are supplemented by equations for the hole and ion currents in terms of their drift and diffusion components:

$$J_h = e\mu_h p E - \mu_h k_B T \frac{\partial p}{\partial x}, \tag{4.5}$$

$$J_I = e\mu_I N_I E - \mu_I k_B T \frac{\partial N_I}{\partial x}. \tag{4.6}$$

Here the ions are assumed to be positively charged. Finally, Gauss' law is incorporated, with the variation in field and charge density still assumed to occur only in the

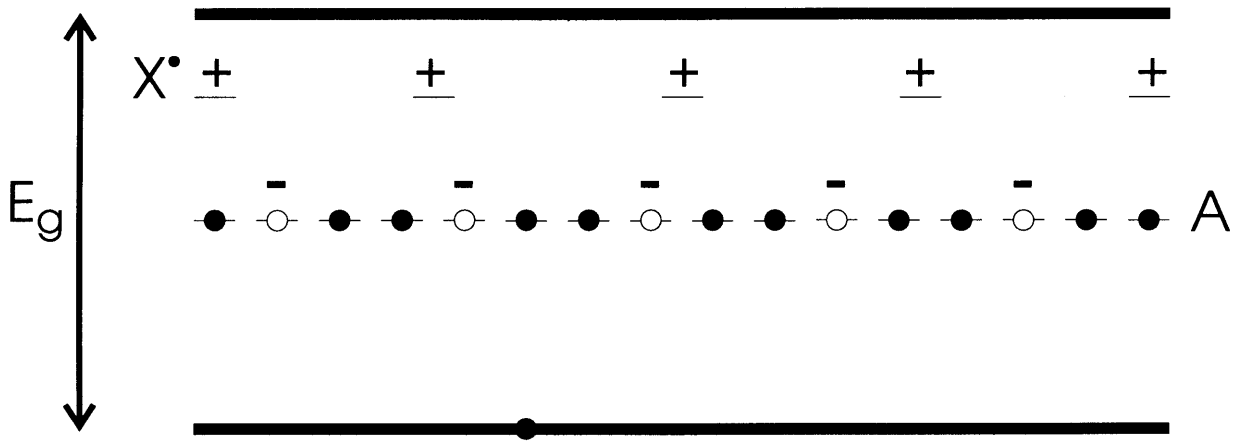

Figure 4.3: Energy-level diagram showing charge compensation. Negatively-charged ionized acceptors A^- (open circles), function as hole traps. Neutral full acceptors are shown as filled circles at level A in the bandgap. Positively-charged ions $X^{\cdot}$ (+), which are relatively mobile at high temperatures above 80°C. When the ions are mobile and a space-charge grating is written by hole transport, the ions drift in the space-charge field and partially compensate the hole grating.

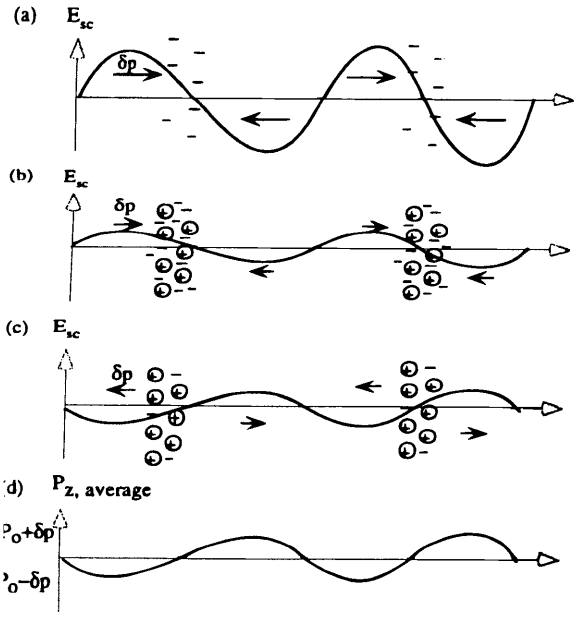

Figure 4.4: Iron- or nickel-doped barium titanate crystal under nonuniform illumination at high temperature. (a) Generation of spatially modulated electronic space charge field, which induces index grating through the lattice distortion δP. (b) Ions (denoted by circled +) slowly drift to compensate electronic space-charge field. (c) After cooling, if the electronic grating can be erased the ionic grating, 180 degrees out of phase, is revealed. (d) A permanent polarization modulation produces the fixed index grating. (After Kewitsch [20].)

x direction:

$$\epsilon\epsilon_0\frac{\partial E}{\partial x} = \epsilon\epsilon_0\frac{\partial E_h}{\partial x} + \epsilon\epsilon_0\frac{\partial E_I}{\partial x} = e(p + N_D - N_A^-) + e(N_I - N_{I0}). \tag{4.7}$$

The symbols used in equations (4.2)–(4.7) are defined as follows:

s	photoionization cross-section of the acceptors
p	hole concentration in the valence band
N_A	total acceptor concentration
N_A^-	concentration of ionized acceptors
N_D	concentration of ionized donors
J_h	hole current density
J_I	ion current density
E_A	trapped hole component of the space-charge field
E_I	ion component of the space-charge field
E	total space-charge field
I	light intensity

Continuing to follow the analysis of Montemezzani et al., we write the spatially varying quantities in the model as follows:

$$p(x,t) = p_0(t) + p_1(t)e^{jKx}, \tag{4.8}$$

$$N_A^-(x,t) = N_{A0}^-(t) + N_{A1}^-(t)e^{jKx}, \tag{4.9}$$

and so forth. In all cases, only the real parts of the quantities are of physical significance. Because optical measurements are carried out by first-order Bragg diffraction, for small modulation m the first spatial harmonics of the carrier concentrations are by far the most significant. For small m, we can linearize the dynamic system described by equations (4.2)–(4.7). The result is a set of three coupled first-order linear differential equations:

$$\frac{d}{dt}\begin{bmatrix} n_1(t) \\ N_{A1}^-(t) \\ N_{I1}(t) \end{bmatrix} = \begin{bmatrix} a_{11} & a_{12} & a_{13} \\ a_{21} & a_{22} & 0 \\ a_{31} & a_{32} & a_{33} \end{bmatrix}\begin{bmatrix} n_1(t) \\ N_{A1}^-(t) \\ N_{I1}(t) \end{bmatrix} + \begin{bmatrix} b \\ b \\ 0 \end{bmatrix} I_1(t). \tag{4.10}$$

In the third-order linear dynamic system described by equation (4.10), the physical

quantities that determine the response of the crystal are lumped into the parameters a_{ij} (see Table 4.1). a_{23} is equal to zero because the ionic grating does not directly affect the trapped carrier grating (carriers are immobile while trapped). $b_3 = 0$ because the light intensity does not directly affect the ionic grating. Montemezzani et al. proceeded from this point by solving the system of equations (4.10) exactly in terms of unknown eigenvalues and plotting the results against experimental data [15]. A curve fit was then used to find the three eigenvalues from the measured data.

In order for such a mathematical model to be useful, it is essential to find the relationships between the eigenvalues Γ_1, Γ_2 and Γ_3 and the coefficients a_{ij}. This is because it is the eigenvalues that appear in the solution for the step responses of the gratings. For example, the step response of the electric field grating is given by

$$E_1(t) = E_{1\text{sat}} + E_{1(\Gamma_1)} \exp(-\Gamma_1 t) + E_{1(\Gamma_2)} \exp(-\Gamma_2 t) + E_{1(\Gamma_3)} \exp(-\Gamma_3 t). \qquad (4.11)$$

Thus the eigenvalues Γ_i are rate constants. Their values can be found for real crystals by fitting the theoretical curve to time-dependent diffraction efficiency measurements. But the physical parameters we wish to measure when we fit our theoretical curve to the measured data are contained in the matrix coefficients a_{ij}.

Unfortunately the characteristic equation obtained from the third-order system of Montemezzani et al. is cubic. Factoring it exactly yields very complicated mathematical expressions, so those authors used a series expansion to relate the eigenvalues of the matrix

$$\begin{bmatrix} a_{11} & a_{12} & a_{13} \\ a_{21} & a_{22} & 0 \\ a_{31} & a_{32} & a_{33} \end{bmatrix} \qquad (4.12)$$

to its entries a_{ij}. This procedure was very complex, making it hard to use physical intuition for interpretation of the results. This is particularly true when we also

consider photorefractive coupling between the object and reference beams during hologram writing. For these reasons, we depart from the analysis of Montemezzani et al. and follow a different, simplified procedure.

The third-order system (4.10) for the carrier grating amplitudes can be reduced to a second-order system without significant loss of accuracy if the lifetime of holes in the valence band is much shorter than the other time scales in the problem. In our experiments, the light intensity $I(t)$ was always low enough to make this adiabatic approximation accurate. This allows us to treat the rate equation for the hole concentration as an algebraic equation determined at each instant by (1) the other system variables $N_{A1}^{-}(t)$ and $N_{I1}(t)$, (2) the input $I_1(t)$, and (3) the spatially constant parameters that determine the coefficients a_{ij}. The first row of the system (4.10) is replaced by

$$\frac{d}{dt}n_1(t) = 0 = a_{11}n_1(t) + a_{12}N_{A1}^{-}(t) + a_{13}N_{I1}(t) + bI_1(t). \tag{4.13}$$

The other two equations of the system, given by the second and third rows of (4.10), are unchanged. But now we have reduced the model to a second-order (two-pole) system. It will be shown later that characteristics of two-pole response can be seen clearly in the experimentally measured diffraction efficiency data taken during writing of fixable gratings at high temperatures. That will justify the approximation we have just made. The new system is:

$$\frac{d}{dt}\begin{bmatrix} N_{A1}^{-}(t) \\ N_{I1}(t) \end{bmatrix} = \begin{bmatrix} a'_{11} & a'_{12} \\ a'_{21} & a'_{22} \end{bmatrix}\begin{bmatrix} N_{A1}^{-}(t) \\ N_{I1}(t) \end{bmatrix} + \begin{bmatrix} b'_1 \\ b'_2 \end{bmatrix} I_1(t). \tag{4.14}$$

Now, since we have a two-pole model for grating dynamics, we can use a simplified time response for the state variables (and derived quantities such as the space-charge field). These quantities have only two significant exponentially decaying components:

$$E_1(t) = E_{1\text{sat}} + E_{1(\Gamma_1)}\exp(-\Gamma_1 t) + E_{1(\Gamma_2)}\exp(-\Gamma_2 t) \tag{4.15}$$

We can also relate the measured time constants Γ_1 and Γ_2 to the coefficients a_{ij} by a quadratic equation. That equation is easily solved analytically. The solutions are

$$\{\Gamma_1, \Gamma_2\} = \frac{a'_{11}a'_{22}}{2} \pm \frac{1}{2}\sqrt{(a'_{11} + a'_{22})^2 - 4a'_{21}a'_{12}}. \tag{4.16}$$

Typical responses for the case where ionic diffusion can be neglected ($N_I >> N_A^-$) are shown in Fig. 4.5. The conditions for these solutions are as follows: W_1 is a strong, constant beam; W_2 is turned on at $t = 0$ and off at $t = 12.5/\Gamma_1$. Under these conditions, the steady-state response always tends toward zero for constant input, as observed in most experiments. (This implies that the impulse response has zero total area.) The impulse response corresponding to the solution (4.15) is

$$h_{\Delta z}(t) = \gamma \Delta z \left(\Gamma_1 \exp(-\Gamma_1 t) - \Gamma_2 \exp(-\Gamma_2 t)\right), \tag{4.17}$$

where γ is a constant. The corresponding pole-zero plot is compared to that of a single-carrier medium in Fig. 4.6.

Now we can find a simple formula for the frequency response of a thick crystal where interaction of the writing beams is taken into account. In order to find the frequency response $H_{\Delta z}(s)$ for a weak probe beam transmitted through the crystal, we take the Laplace transform:

$$H_{\Delta z}(s) = \gamma \Delta z \left(\frac{1}{s + \Gamma_1} - \frac{\Gamma_2/\Gamma_1}{s + \Gamma_2}\right), \tag{4.18}$$

valid for $\Gamma_1 \neq \Gamma_2$. This expression has poles at $s = \{-\Gamma_1, -\Gamma_2\}$ and a zero at $s = 0$ (because the impulse function has zero area). Now we can use the result obtained in section 2.1.5 to obtain the frequency response, including interaction between the writing beams:

$$H_L(s) = \exp\left[\gamma L \left(\frac{\Gamma_1}{s + \Gamma_1} - \frac{\Gamma_2}{s + \Gamma_2}\right)\right], \tag{4.19}$$

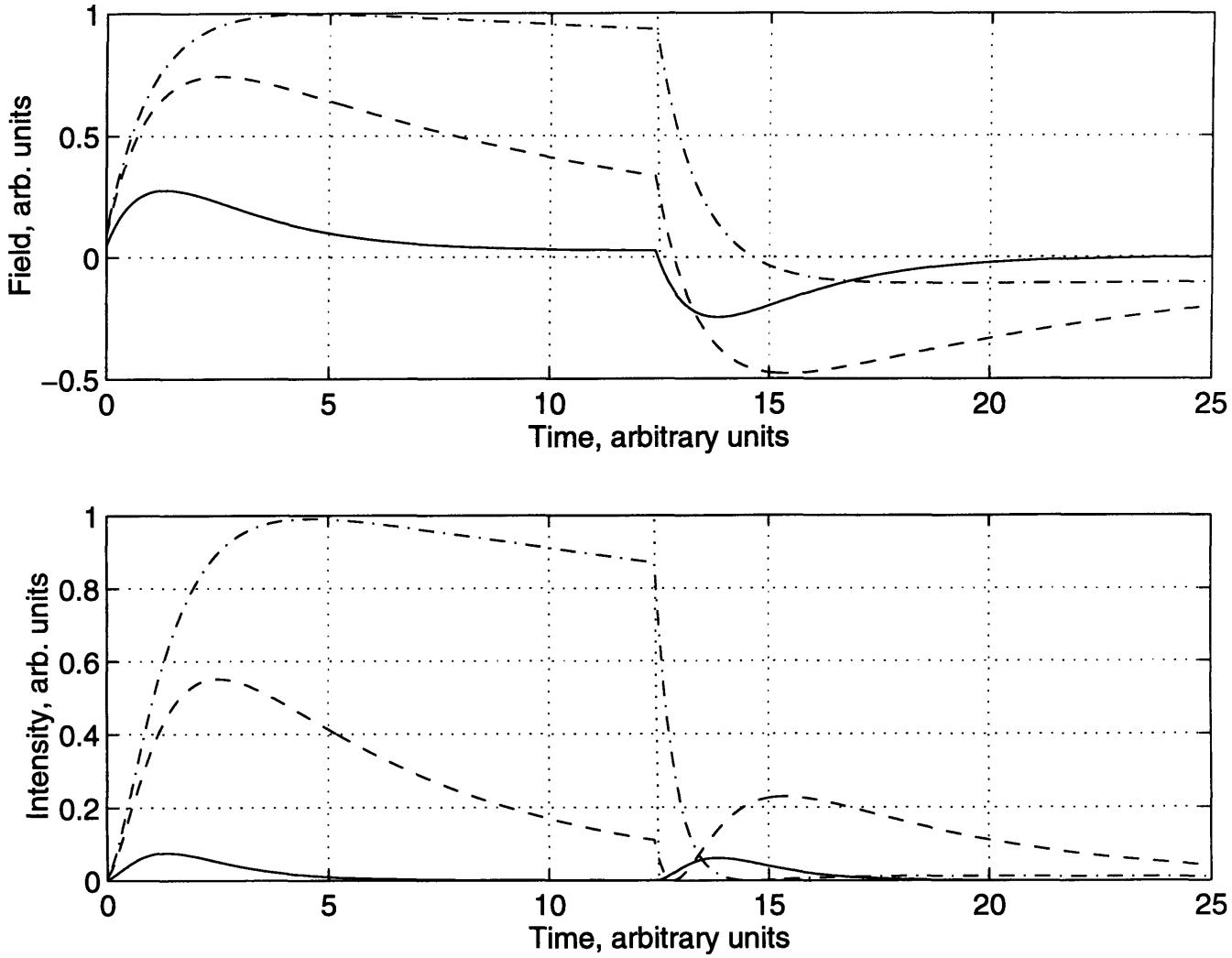

Figure 4.5: Time responses of the space-charge field and diffraction efficiency when the weaker writing beam, W_2 has the shape of a boxcar pulse beginning at $t = 0$ and ending at $t = 12.5/\Gamma_1$. Time (x-axis) is expressed in units of $1/\Gamma_1$. Three cases are plotted: $\Gamma_1/\Gamma_2 = 2$ (solid), 10 (dashed), and 100 (dot-dash). The photoconductive-grating amplitude is identical in all three cases. Ionic diffusion is neglected.

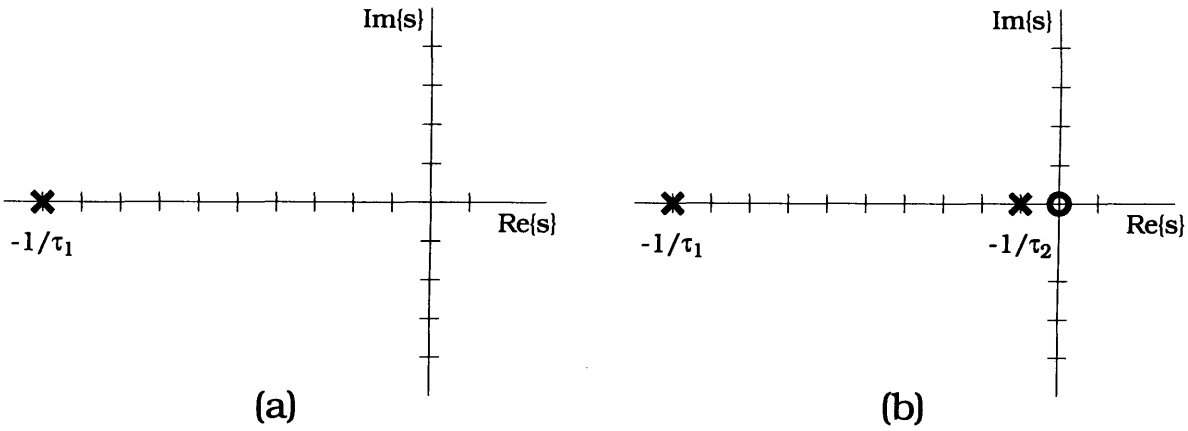

Figure 4.6: (a) Pole-zero plot for a single-carrier photorefractive material. (b) Pole-zero plot for a two-carrier photorefractive material where the light-insensitive carrier (e.g., mobile ion) has a long response time τ_2 and diffusion of the ions is negligible. If ionic diffusion becomes significant, the zero moves slightly to the left (but always lies to the right of both poles).

where L is the interaction length. This is a very easy function to handle, especially since the exponential can be broken up into a product. The expression (4.19) is valid in the undepleted pump approximation. The inverse transform is not so simple, but it is equal to the convolution of two impulse responses of the form reported by Horowitz et al. and reproduced in section 2.1.5, Eq. (2.30). Thus time-domain predictions for the time response of beam coupling during fixed-grating writing are easily calculated. Numerical software such as MATLAB can be used to perform the convolution.

4.2 Fixing holograms

4.2.1 Results of Theoretical Model

The case of fixing by cooling in the dark will be treated theoretically. This is the most important case for practical applications because it is essential for multiplex recording. In multiplex recording holograms are written sequentially at high temperature

and then fixed by cooling. There is no practical way to write all stored holograms continuously during cooling, so the crystal is best left dark. This allows screening to retard the drift component of the decay process.

High-efficiency fixed-hologram readout in a photorefractive crystal depends primarily on (1) successfully cooling an ionic charge grating with large unscreened ionic space-charge field

$$E_i = \frac{q\Lambda\Delta N_I}{2\pi\epsilon\epsilon_0} \tag{4.20}$$

(where ΔN_I is the a.c. component of the concentration of mobile ions), and (2) choosing experimental conditions to maximize the diffraction efficiency at the readout temperature. This section deals only with point (1); readout optimization is left until the following section.

The decay rate of a sinusoidal photorefractive grating is proportional to the mobility of the carriers that form the grating.

Since the mobility of the ions that form secondary gratings follows an activated temperature dependence, we can predict the final fixed diffraction efficiency if we know how the temperature changes over time. This information is very important when designing a hologram storage system, and experiments yielding information on the efficiency of the fixing process are reported in the Chapter 5. Since no mathematical model of the fixing process was found in the literature, a simple one was developed. The model, described in detail below, yields a very simple result. The final fixed charge density, ρ_f, is related to the initial charge density ρ_i by

$$\frac{\rho_f}{\rho_i} = \exp\left(\frac{-\tau_1}{\tau_0}\right). \tag{4.21}$$

Here τ_0 is the grating decay rate at the writing temperature. τ_1 is given by $(k_B T_0^2)/(E_A T')$, where k_B is Boltzmann's constant, T_0 is the writing temperature, E_A is the activation

energy of the ionic grating, and T' is the rate of change of the temperature over time as the crystal is cooled. Figure 4.21 is a plot of equation (4.21) for several initial temperatures, assuming an activation energy $E_A = 1.5$ eV and an initial time constant $\tau_0 = 1$ s at 110°C. Each curve shows the final (low-temperature) diffraction efficiency predicted by the model for a given cooling rate. The graph shows that faster cooling and lower writing temperatures lead to larger fixing efficiencies. Since $BaTiO_3$ crystals can tolerate only limited thermal gradients without cracking, practical cooling rates are limited. Thus the promise of very fast writing of fixable gratings at high temperatures is probably unrealistic. Shorter fixable grating writing times require faster cooling or higher ionic activation energies to maintain efficient fixing.

Higher ionic activation energy E_A leads to more efficient fixing because it reduces τ_1 in Eq. (4.21). Physically, this is because the ions "freeze" in place sooner if their activation energy is higher. In other words, the higher the activation energy, the more rapidly ionic mobility changes with temperature. Ions with lower activation energies are less suitable for fixing even if an acceptable storage time can be achieved, because faster cooling is necessary to fix low-E_A gratings.

4.2.2 Details of the Model

If a space-charge grating with a time-dependent amplitude $\rho(t)E$ is left in the dark, drift and diffusion currents will cause it to decay over time. This can be expressed mathematically as a first-order differential equation:

$$\frac{d}{dt}\rho(t) = -\frac{\rho(t)}{\tau}. \tag{4.22}$$

Here τ, the time constant, is assumed to be, in fact, constant. When the temperature changes during hologram decay, as in the fixing process, the decay rate is no longer

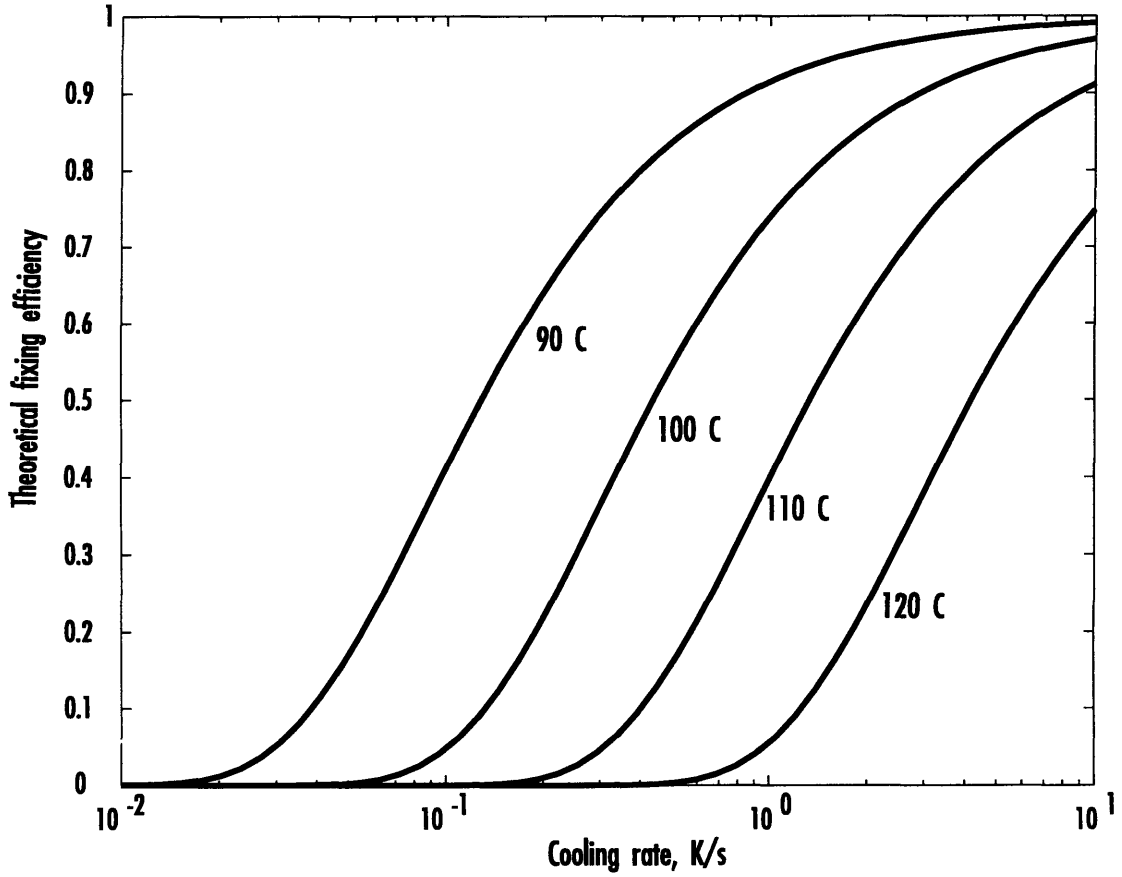

Figure 4.7: Theoretical fixing efficiency as a function of cooling rate for several initial temperatures.

constant:

$$\frac{d}{dt}\rho(t) = -\frac{\rho(t)}{\tau(t)}. \tag{4.23}$$

Equation (4.23) does not include the effects of the dependence of the dielectric constant on temperature, or pyroelectric currents. Those effects, while real, complicate this first-order model unnecessarily. Whether the decay rate changes over time or not, the differential equation for the decay is easy to solve:

$$\frac{1}{\rho}d\rho = -\int_0^t \frac{dt}{\tau(t)}; \tag{4.24}$$

$$\rho = \exp\left(-\int_0^t \frac{dt}{\tau(t)}\right). \tag{4.25}$$

Eq. 4.25 is the general solution to the time dependence of the amplitude of a single-carrier charge grating in the dark. (Here the carriers are ions; in the dark electron screening effects may change the time constant but the decay rate in experiments is seen to be exponential).

Assume that the cooling rate T' is constant: $T(t) = T_0 - T't$. Then the temperature-activated mobility yields a time constant $\tau(t)$ given by:

$$\tau(t) = \tau_\infty \exp\left[\frac{E_A}{k_B(T_0 - T't)}\right]. \tag{4.26}$$

If the initial absolute temperature T_0 is large compared to the total temperature change $T't$, we can use a linear approximation for the argument:

$$\tau(t) \simeq \tau_\infty \exp\left[\frac{E_A}{kT_0}\left(1 + \frac{T'}{T_0}t\right).\right] \tag{4.27}$$

This can be reduced to the more useful form

$$\tau(t) \simeq \tau_0 \exp(t/\tau_1), \tag{4.28}$$

where τ_0 is the initial decay rate and τ_1 is given by $(k_B T_0^2)/(E_A T')$. Physically, this approximation is reasonable if the cooling rate is maintained until $\rho(t)$ has essentially

become constant, and if the total temperature change necessary is at most a few tenths of the writing temperature.

Next we substitute the assumed form (4.28) for the time dependence of the decay rate into the general solution Eq. (4.25) of the differential equation (4.23). This is readily integrated, yielding

$$\rho(t) = \rho(0) \exp\left[\frac{\tau_1}{\tau_0}\left(\exp[-t/\tau_1] - 1\right).\right] \tag{4.29}$$

This relation is plotted in Fig. 4.8. The figure shows that indeed most of the decay of the space-charge grating takes place during the initial high-temperature phase of cooling.

Errors in this model: we have used a simple mathematical procedure to estimate the magnitude of the fixed grating that will remain in the crystal at temperatures where the decay time is very long. But since we were only concerned with a first-order approximation of the decay rate during a brief fixing interval when the decay rate was fairly large, we obtained a decay rate that approaches zero after fixing. Thus this is of course not an accurate way to predict hologram storage times. Even fixed gratings eventually decay. (Hologram decay is treated in section 4.1.

4.3 Reading out fixed holograms

4.3.1 Theory

New data in this study support the suggestion by Rytz et al. [21] that considerable deionization takes place on *heating* from 20°C to 120°C in undoped $BaTiO_3$. The observation is extended to Fe and Ni doped $BaTiO_3$ crystals. This is the proposed explanation for the reversible drop in diffraction efficiency of fixed charge gratings at low temperatures, which is reported in Chapter 5.

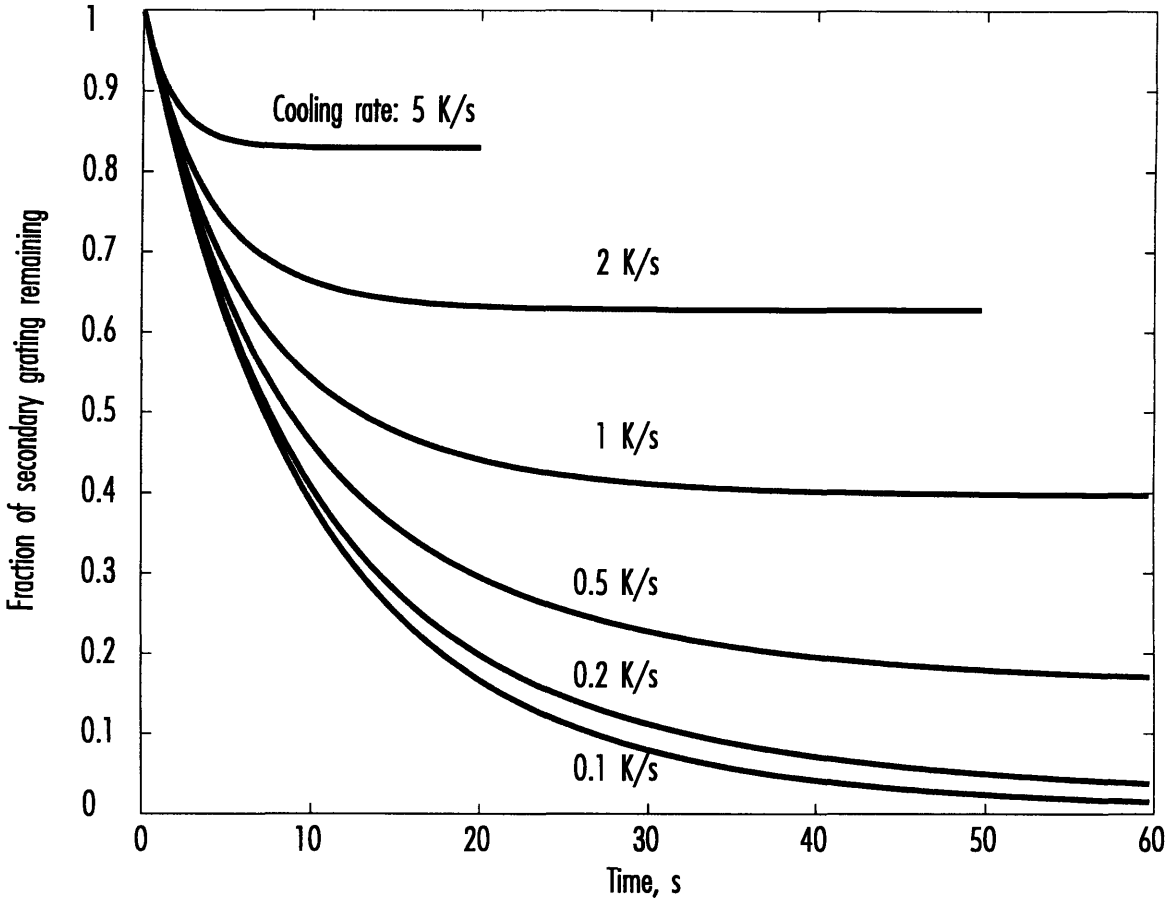

Figure 4.8: Predicted time-dependent decay during fixing process of a space-charge grating whose carriers have a temperature-activated mobility. Initial temperature is $T_0 = 110°C$; assumed decay time constant τ_0 at T_0 is 10 s. Various cooling rates are shown: faster cooling yields more efficient fixing.

During readout of fixed holograms in Fe- and Ni-doped $BaTiO_3$, the following phenomenon was observed. For a given grating period, crystal orientation and light intensity, there is a threshold temperature below which the fixed grating's diffraction efficiency drops precipitously (see Fig. 5.8). This loss of diffraction efficiency could not be repaired by adjusting the Bragg angle, so it was not simply due to the slight change in Bragg angle with temperature. The observation was not due to permanent erasure of the ionic grating. The diffraction efficiency could be restored by heating the crystal back above the threshold temperature. To explain this experimental observation, a screening theory with a temperature-dependent trap density has been developed.

The change in diffraction efficiency with temperature, typically about 2 orders of magnitude, is far too large to be explained by the temperature dependences of the electrooptic coefficient ϵ and dielectric constant r_{eff}. Further, the increase in diffraction efficiency is approximately independent of crystal orientation. This would not be possible if the phenomenon was caused by temperature dependences of ϵ and r_{eff}. A sketch of the steady-state diffraction efficiency of a fixed charge grating in a photorefractive crystal is shown in Fig. 4.9 where η_{max} is approximately independent of temperature. Here $K_D^2(T) = N_T(T)q_e^2/\epsilon(T)kT$ is the inverse Debye screening length (typically 0.2 to 2 μ m in photorefractive crystals). The increase is reversible on cooling and reheating.

It will be assumed that the low diffraction efficiency at room temperature is due to screening of the ionic grating by trapped holes. The trap density of the crystal must increase by at least an order of magnitude on cooling from 100°C to 20°C to explain our results. This assumption is consistent with measurements by Rytz et al. [21], showing that the effective photorefractive trap density in many $BaTiO_3$ crystals varies by more than an order of magnitude in this temperature range. The authors

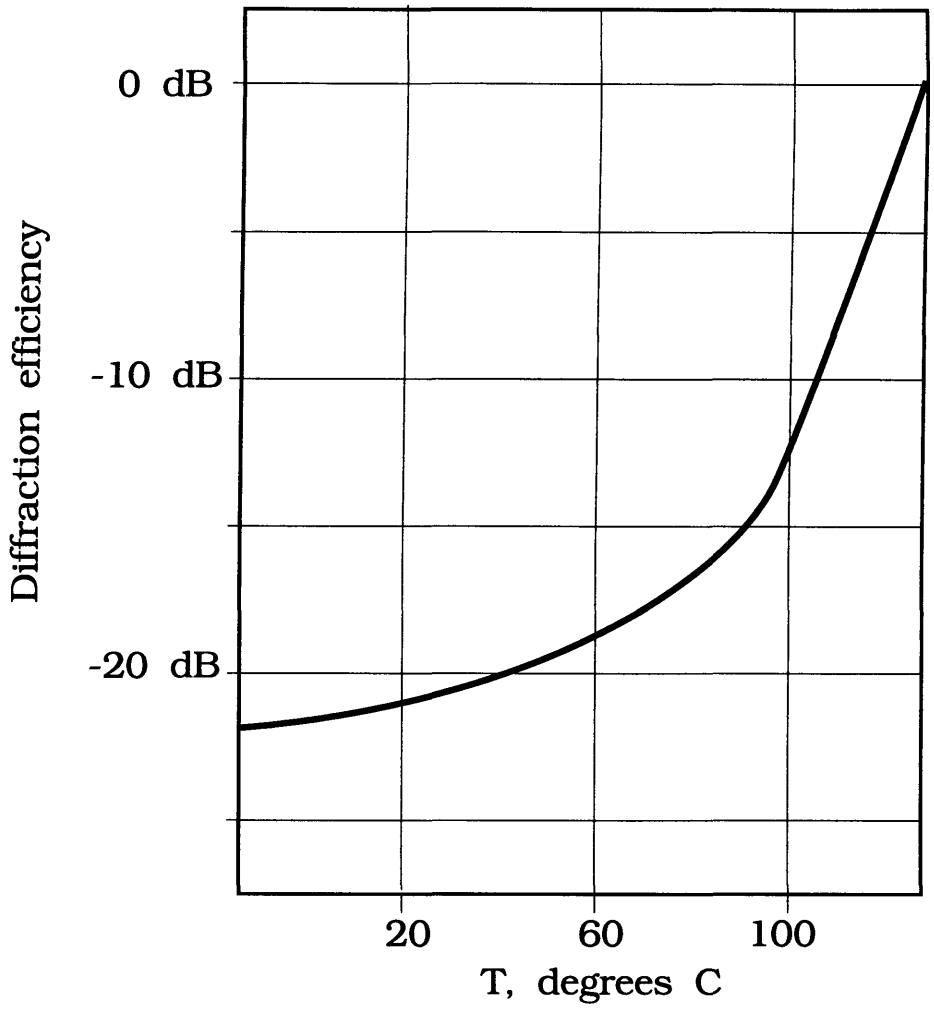

Figure 4.9: Sketch of fixed grating diffraction efficiency versus temperature

of that study offered no detailed model to explain their results, but suggested that charge storage in shallow hole traps (i.e., levels close to the valence band) could be responsible. Nolte et al. observed screening of the photorefractive effect at low temperatures in InP:Fe [83, 84]. The data plotted in Fig. 4.10 (from [83]) show temperature-dependent screening of a continuously-written photorefractive hologram. The effect has also been observed in undoped GaAs [83], undoped GaP [85, 86], and in $Bi_{12}GeO_{20}$ [87]. (A similar but more complex effect involving a metastable optically

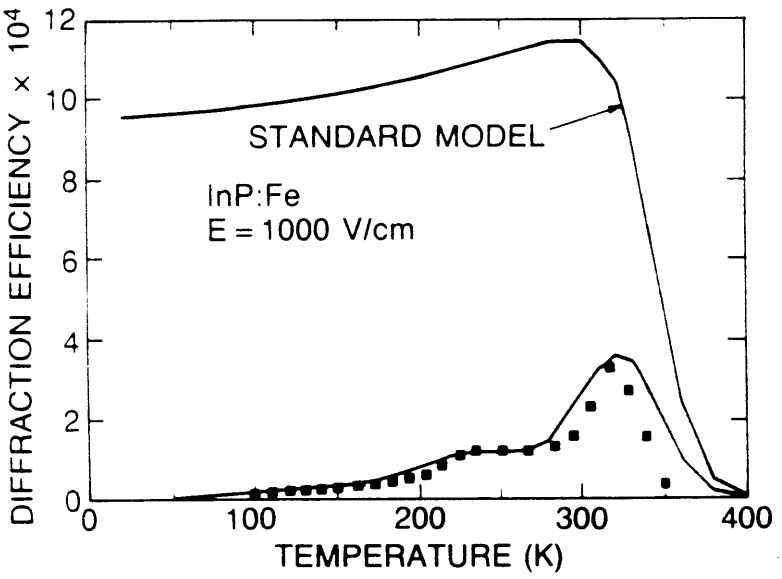

Figure 4.10: Measured screening of a photorefractive grating at long grating vector under an applied electric field (after [83])

excited state of the EL2 defect in undoped GaAs has also been observed [84, 88].) Screening (or "quenching") of the photorefractive effect should be measurable in many other compensated semiconductor photorefractive materials. It has not been observed in $BaTiO_3$ [21], apparently because the destructive phase transition at 5°C makes complete filling of the shallow (screening) traps difficult and because the strong photochromic effect in $BaTiO_3$ typically allows carriers to be photoexcited directly from the shallow traps. This causes photorefractive gratings to be written in the shallow traps as well, opposing the screening effect but still producing a measurable increase in trap concentration at high intensity and low temperature [67].

The present work is apparently the first report of nonequilibrium temperature-dependent screening of fixed holograms, but the effect should be present to some degree whenever holograms are fixed in a photorefractive material. This is especially true if mobile ions are produced by any dopant (such as Fe in $BaTiO_3$ [82]) that also introduces shallow ($\leq$ 1 eV) trap levels. This type of temperature-dependent screening has apparently not been observed in $LiNbO_3$. This is consistent with the fact that shallow trap filling effects such as sublinear response time and the photochromic effect are not normally observed in $LiNbO_3$ [67].

Physically, screening of the photorefractive space charge occurs in the nonequilibrium situation obtained by illuminating the sample. When the thermal emission rate from a shallow trap level becomes low enough that the level can be half-populated with photoexcited carriers, its capacity to screen space-charge fields is maximized. In both our experiments and those of Rytz et al., charge is apparently being redistributed between localized states in the bandgap on heating. Counter to the usual expectation, the degree of ionization increases on cooling. The screening of fixed gratings observed in this study is consistent with the screening of the photorefractive

effect described by Nolte et al. [83, 84].

Following Nolte et al. , we can calculate the depth of the shallow trap level involved from the onset temperature of the screening. (We assume here that shallow traps are primarily emptied thermally, not optically. This assumption is only qualitatively true in $BaTiO_3$, and depends on doping. But it allows us to derive an answer that does not depend on the photoionization cross-section of the shallow traps.) Let N_1, s_1, σ_1 be the concentration, photoionization cross section and recombination cross sections of the deep traps, and N_2, s_2, σ_2 the equivalent numbers for the shallow traps. Then the fraction of occupied traps is given by equation (3) in [83]:

$$\frac{N_2^-}{N_2^0} = \left(\frac{s_1}{\sigma_1 v_{th}} I_0\right) \frac{\exp(E_2/k_B T)}{N_c}, \tag{4.30}$$

where N_c is the band-edge density of states and v_{th} is the thermal velocity. (Nolte writes the above expression for electrons, but shallow hole traps can screen the space-charge field of a fixed grating just as easily. Thus we will define the shallow-trap binding energy E_2 with respect to the valence band.) The first factor on the right is the concentration of holes, $p(I,T)$. Thus (4.30) can be rewritten:

$$\frac{N_2^-}{N_2^0} = \frac{p}{N_c} \exp(E_2/k_B T). \tag{4.31}$$

We can use Eq. (4.31) to estimate the shallow trap binding energy. In $BaTiO_3$:Fe (1000 ppm), with $\mathbf{k} \,||\hat{c}$, data presented in the following chapter show that the onset of screening occurs at about 110 °C (see Fig. 5.9). The measured photoconductivity at that temperature is $1.44 \times 10^{-11}(\Omega \cdot \mathrm{cm})^{-1}$. This yields $p = 9 \times 10^7 \mathrm{cm}^{-3}$. (Here we have assumed that the mobility is approximately 1 $\mathrm{cm}^2/V \cdot s$.) The concentration of filled shallow traps needed to screen the grating in question can be found from the formula for Debye screening:

$$K_D = \sqrt{\frac{q^2 N_2}{\epsilon \epsilon_0 k T}}, \tag{4.32}$$

where we assume that at the onset of screening the grating vector $k = 2\pi/1.4\mu$m is equal to K_D. This gives us $N_2 = 9 \times 10^{15}\text{cm}^{-3}$. We assume that the shallow traps responsible for the low-temperature screening are the Fe' ($Fe^{3+}_{Ti^{4+}}$) levels (which can accept one hole). The total concentration of these shallow states, N_2^0, is known to be $[Fe'] = 1.6 \times 10^{19}\text{cm}^{-3}$. Given the above assumptions, we can calculate the binding energy of the shallow trap level responsible for the screening.

$$E_2 = k_B T \ln\left(\frac{N_c}{p}\frac{N_2^-}{N_2^0}\right) = 0.83eV. \tag{4.33}$$

This is in close agreement with Hagemann's value of 0.8 eV between the Fe' level and the valence band. The energy just calculated changes by only 76 meV for an order-of-magnitude error in the argument of the logarithm, so it is probably reliable to within 0.15 eV. This is strong evidence that low-temperature non-equilibrium screening is indeed responsible for the dependence of the diffration efficiency of fixed gratings on temperature. If we calculate the shallow trap depth for all three measured orientations (0°, 6°, 14° between $\mathbf{k}$ and $\hat{c}$), we get 0.83 eV, 0.77 eV and 0.76 eV, respectively. The errors in these values may be partly because of inaccuracies in the calculated off-axis dielectric constant.

We can use a similar argument to find the binding energy of the shallow levels responsible for screening in the Ni-doped crystals (see Fig.5.8). In this case, we obtain 1.0 eV for the depth of the shallow traps if we assume that the shallow trap levels are associated with the Ni" centers. The same value (1.0 eV) is obtained for both grating periods measured. More experiments would be needed before we could conclude that the Ni^{2+}/Ni^{3+} level lies 1.0 eV above the valence band.

We now discuss more details of the screening mechanism, once the screening trap density is known. Let ρ_{fixed} be the space charge in the interaction region due to a fixed concentration of ions with a small spatially harmonic part. Assume the material

contains a concentration N_A^- of charged states (probably serving as empty traps) lying near the Fermi level. Then in steady-state there will be a screening charge ρ_{scr} so that the total space charge is given by $\rho_{tot} = \rho_I + \rho_{scr}$. The screening charge ρ_{scr} is given by

$$\rho_{\text{scr}} = -\frac{K_D^2}{K^2 + K_D^2}\rho_{\text{fixed}}, \tag{4.34}$$

where K is the grating vector and $K_D^2 = N_2^- q^2/(\epsilon k_B T)$. ($K_D$ is the inverse Debye screening length [89].) Thus if $K >> K_D$, very little screening takes place and the total charge is approximately equal to the ionic charge. On the other hand, if $K < K_D$, screening is substantial and for $K << K_D$ the total charge approaches zero. These regimes are illustrated in Fig. 4.11 (a).

Since we cannot observe the space charge directly, we must rely on diffraction of a beam of light to measure the refractive index variation due to the space-charge field of the grating. The amplitude of the refractive index grating is

$$n_1 = \frac{1}{2} n^3 r_{\text{eff}} |E_1|, \tag{4.35}$$

where n is the average refractive index and r_{eff} is the effective Pockels electrooptic coefficient. r_{eff} depends on the direction of the $\bar{K}$ vector with respect to the crystal axes. E_1 is the first Fourier component of the space-charge field,

$$E_1 = \frac{\rho_I + \rho_{scr}}{jK\epsilon\epsilon_0}. \tag{4.36}$$

The diffraction efficiency of a volume phase-only grating at the Bragg angle is given by [7]

$$\eta = \sin^2\left(\frac{\pi n_1 L}{\lambda \cos\theta_0}\right) \simeq \left(\frac{\pi n_1 L}{\lambda \cos\theta_0}\right)^2. \tag{4.37}$$

Here L is the interaction length (equal to the crystal thickness), λ is the wavelength of the light, n_1 is the amplitude of the refractive index variation, and θ_0 is half the

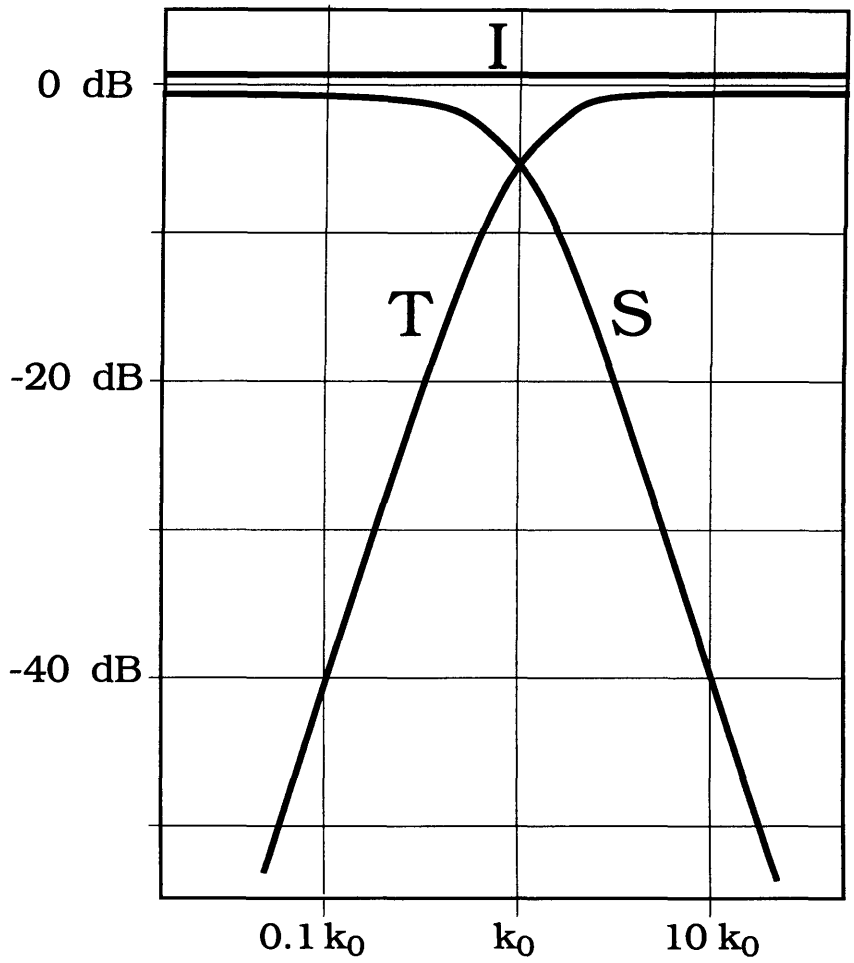

Figure 4.11: (a) Ionic (I), screening (S), and total (T) space charge as a function of grating vector. In the proposed model, $k_0 = (q^2 N_2^- / \epsilon\epsilon_0 kT)^{\frac{1}{2}}$ is a function of temperature, primarily because of the temperature dependence of N_2^-

.

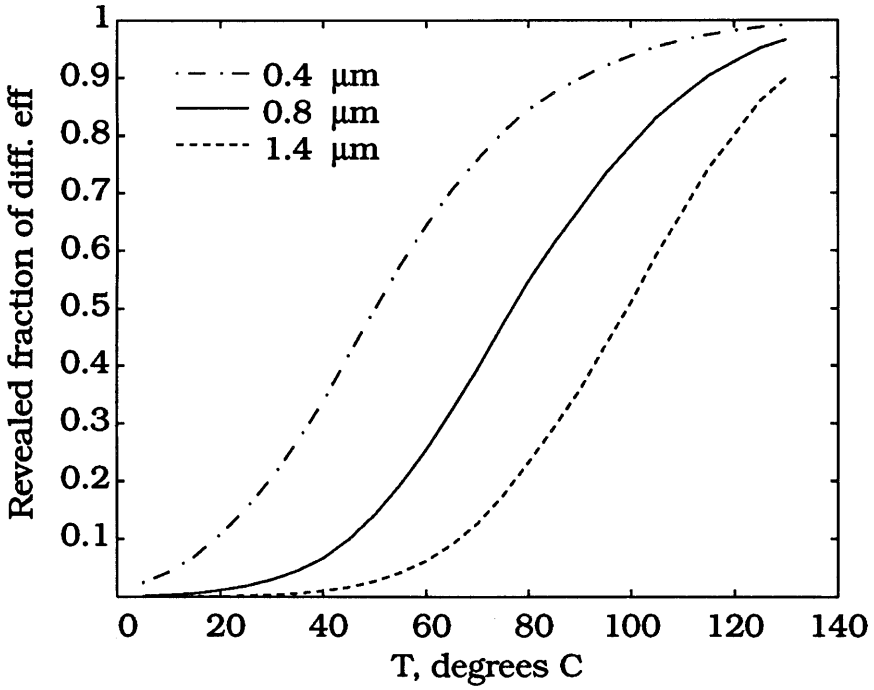

Figure 4.12: Predicted diffraction efficiency as a function of temperature in $BaTiO_3$:Fe (1000 ppm, reduced), $I \simeq 500mW/cm^{-2}$, for grating vectors of 0.4, 0.8, and 1.4 μm (for measured parameters see section 5.4).

angle between the writing beams inside the crystal. The approximation is valid when $\eta << 1$.

The formula for the diffraction efficiency of the screened ionic grating is

$$\eta \simeq \left(\frac{\frac{1}{2}\pi n^3 L}{\lambda \cos(\theta_0)}\right)^2 \frac{\rho_I^2}{\epsilon_0^2} \frac{r_{\text{eff}}^2}{\epsilon^2} \frac{K^2}{(K^2 + K_D^2)^2}, \tag{4.38}$$

valid for $\eta << 1$. This can be derived by combining Eqs. (4.34)–(4.37). The diffraction efficiency can be related to the trap concentration by observing that the ratio r_{eff}/ϵ is approximately constant with respect to temperature. Numerical results for various experimental conditions are plotted in Figs. 4.12–4.14.

Figs. 4.12–4.14 agree qualitatively with the data plotted in the following chapter, Figs. 5.8 and 5.9. There are still several clear discrepancies between theory and exper-

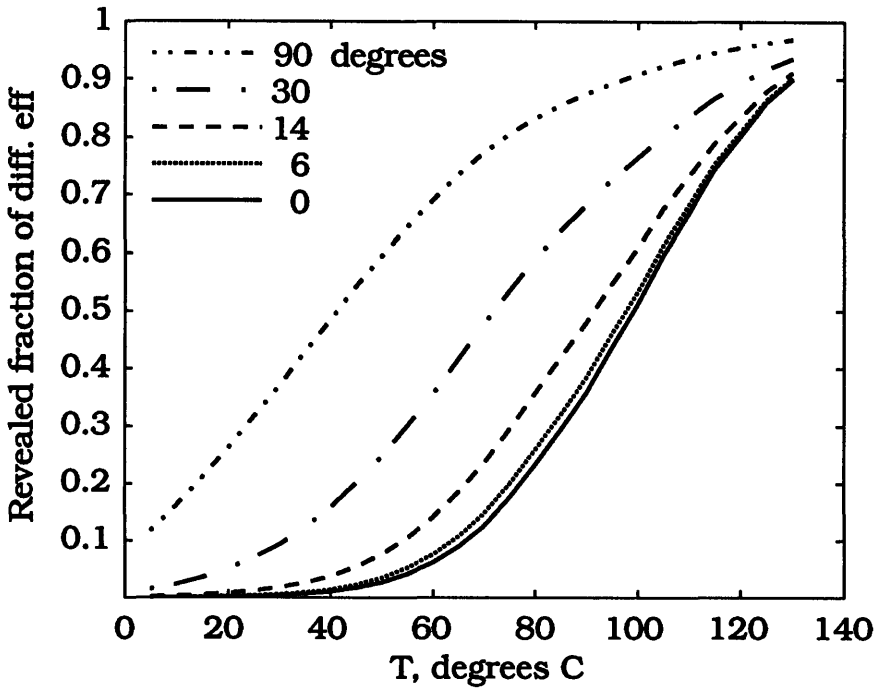

Figure 4.13: Predicted diffraction efficiency as a function of temperature in $BaTiO_3$:Fe (1000 ppm, reduced), $I \simeq 500 mW/cm^{-2}$, for orientations of 90° $k \perp \hat{c}$, 30°, 14°, 6°, and 0°(for measured parameters see section 5.4).

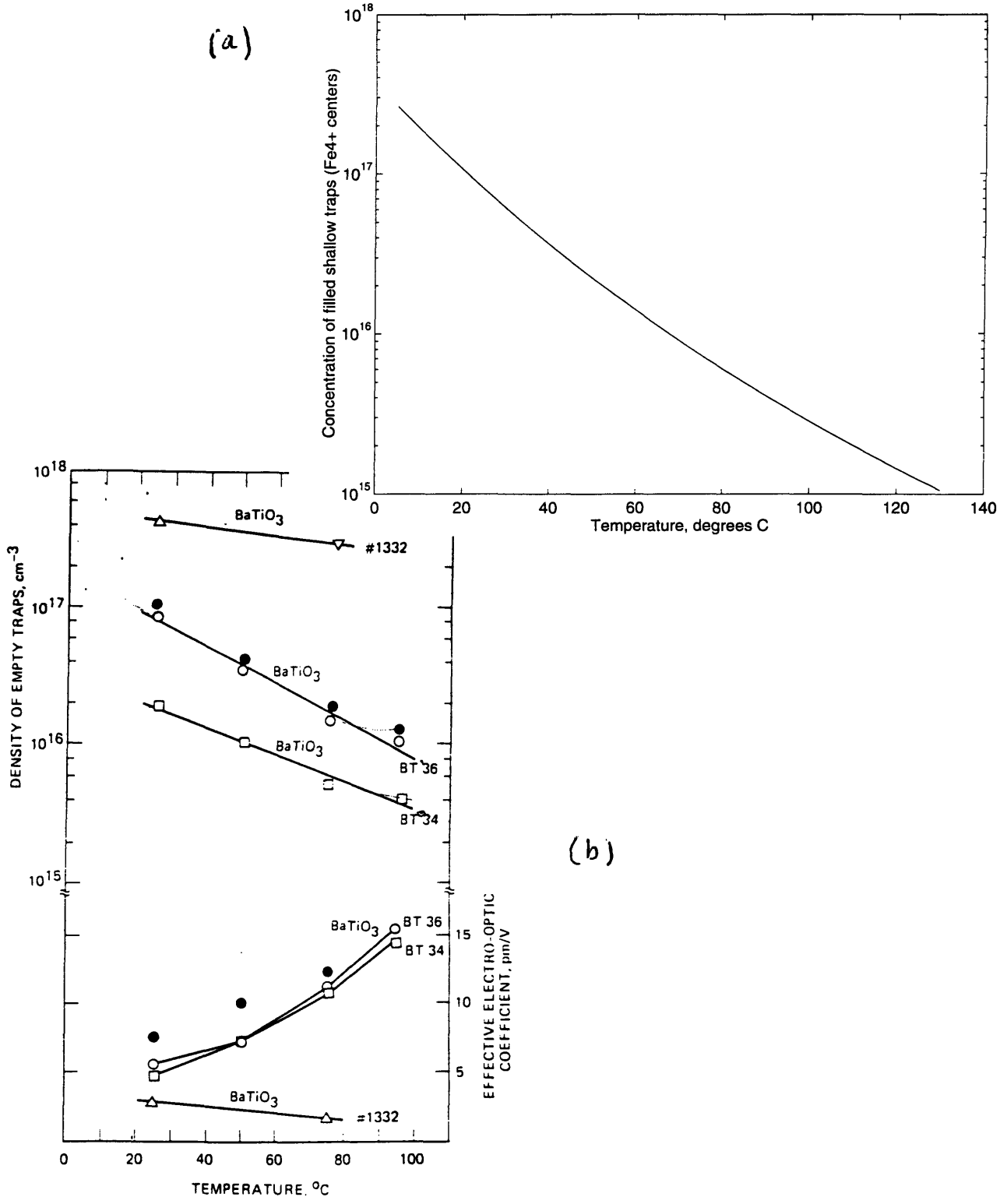

Figure 4.14: (a) Predicted filled shallow trap concentration in $BaTiO_3$:Fe (1000 ppm, reduced), $I \simeq 500 mW/cm^{-2}$, (for measured parameters see section 5.4). (b) Measured photorefractive trap concentrations as functions of temperature (after [21]).

iment, however. The theoretical plots shown here have less abrupt transitions from high to low diffraction efficiency than were observed in some experimental measurements. This may be partly because the Bragg angle was not continually adjusted for each temperature, but only spot-checked after each 5 or so data points and at the highest and lowest temperatures. Thus transitions from high to low $\eta(T)$ may in fact be less abrupt than they appear from the data. In addition, Fig. 4.13 shows considerably less dependence on crystal orientation angle than was observed experimentally. The actual improvement in performance was much better than predicted by our theory. One reason for this may be inaccuracy of the approximation involved in simply using the unclamped dielectric constants at each temperature and neglecting the effect of mechanical stress on the d.c. polarizability.

4.3.2 Discussion

Low readout temperatures are essential for obtaining long storage times. Therefore any means of lowering the threshold temperature for high-diffraction-efficiency readout of fixed gratings will offer increased storage time at minimal cost in diffraction efficiency. The proposed phenomenological model is that the higher effective dielectric constant seen at oblique grating angles in $BaTiO_3$ reduces the space-charge field, making trapped space charge less able to screen the fixed grating field. This in turn means that lower temperatures can be tolerated before the (temperature-dependent [83, 84]) effective trap density becomes too large and the fixed grating suffers heavy screening. The reduced electric field is unimportant for the diffraction efficiency because the ratio r_{eff}/ϵ is roughly constant over temperature and angle.

Experimental results obtained so far for all of these orientations were published in [19] and are given more completely in Chapter 5.

4.4 Storing and erasing fixed holograms

Storage and erasure are similar processes for ionic gratings–one is the obverse of the other. The storage time τ_s can be defined as the decay time constant of the ionic grating at low temperature. The erasure time τ_e depends on the degree of erasure required. For 30 dB (a 1000-fold decrease in diffraction efficiency), τ_e is 6.9 time constants at high temperature.

The storage time of fixed holograms in $BaTiO_3$ depends strongly on temperature, but is also a function of orientation and grating period. (Fortunately, illumination by a readout beam causes little or no erasure.)

Holograms fixed in $BaTiO_3$ crystals are erased by reheating to the writing temperature and waiting for the diffraction efficiency to decay to zero. In our physical model, this occurs because the spatially nonuniform ionic carrier concentration decays into a uniform concentration through drift and diffusion. Quantitatively, therefore, erasure follows the same time response as the decay shown in the right-hand half of the plots shown in Fig.4.5.

Chapter 5

EXPERIMENTAL HOLOGRAM FIXING STUDIES IN $BaTiO_3$

5.1 Overview

In this chapter, detailed experimental results on hologram fixing by thermal cycling in $BaTiO_3$ are reported. A wide variety of dopants, crystal orientations and temperatures were investigated.

In past work, thermally activated fixing in $BaTiO_3$ has only been reported by a few workers, in a few crystals [8, 16]. Recently, Kirillov and Feinberg [16] reported that crystal impurities were apparently an important factor in fixing. But the particular impurities present in their crystals were completely unknown. Their fixed-hologram diffraction efficiencies were very low, less than 0.1% .

Original results reported in this chapter include:

1. For the first time, high diffraction efficiencies ($> 10\%$) were obtained from thermally fixed holograms in $BaTiO_3$.

2. Two distinct temperature-activated mobile ions have been found in $BaTiO_3$. One is consistent with the expected behavior of oxygen vacancies in $BaTiO_3$. The other may be H^+ ions bound to oxygen atoms within the crystal structure.

3. Fixing is correlated with Fe and Ni doping in $BaTiO_3$. It has not been observed in pure crystals or those doped with Co, V, or Rh at levels of 50-100 ppm.

4. The diffraction efficiency of fixed holograms in $BaTiO_3$ was found to depend strongly on temperature and crystal orientation.

5. Diffraction efficiency of holograms fixed by thermal cycling can be improved by using distinct storage and readout steps in the fixing process.

6. Holograms fixed with their electric fields parallel to the $\hat{\mathbf{c}}$ axis of $BaTiO_3$ crystals cannot always be read out after cooling. It is shown that this is a phase-matching problem due to the temperature dependence of the birefringence $n_e - n_o$ in $BaTiO_3$.

5.2 Crystal selection and preparation

The crystals used for the fixing experiments described in this chapter were selected from a variety of single-crystal $BaTiO_3$ samples. These crystals were grown in our own laboratory by the top-seeded solution growth (TSSG) method [90] over the past ten years (with the exception of the Ni-doped samples, which were grown at Lockheed Sanders Inc., Nashua, NH, also by TSSG). Doping of the crystals was accomplished by adding impurities to the melt before growth. With the exception of the Rh-doped crystals, an equal number of moles of Ti were removed from the melt and the doping levels given are parts per million atomic in the melt except where otherwise noted. After growth, the crystals were oriented by x-ray diffraction and then cut into pieces up to $5 \times 5 \times 5$ mm. Since $BaTiO_3$ is a tetragonal ferroelectric polar crystal at room temperature but is grown at high temperature in the cubic phase, 90° and 180° domain boundaries are initially found in the crystals. Before final polishing, therefore,

the crystals were poled by application of electric fields parallel to the desired $\hat{\mathbf{c}}$ axis, and mechanical stress perpendicular to $\hat{\mathbf{c}}$. Finally, the crystals were polished with diamond paste on an aluminum foil surface adhered to a quartz optical flat.

Crystals were chosen by conducting preliminary thermal fixing experiments so as to have several pure crystals, at least one crystal for each dopant available, and several crystals containing any dopant that proved to be promising for fixing. When reduced crystals were available in addition to unprocessed as-grown crystals, they were also included. Details on the composition and post-growth treatment histories of the crystals on which detailed follow-up fixing experiments were done are summarized in Table 5.1.

5.3 Recording Fixable Holograms

5.3.1 Experimental Procedures and Results

In the hologram writing system shown schematically in Fig. 5.1, writing beams W_1 and W_2 (514 nm wavelength) from a single argon-ion laser interfered to produce a sinusoidal intensity pattern in a photorefractive $BaTiO_3$ crystal X. The intensities of both writing beams were approximately 600 mW/cm^2, so that the fringe modulation, $m = 2(I_1 I_2)^{1/2}/(I_1 + I_2)$, was approximately unity. Shutters were arranged so that the beams could be turned on and off at will. The resulting refractive index grating was read out at the Bragg angle by a 633 nm helium-neon laser beam R, which was Bragg matched to the index grating. The diffracted beam S was monitored by detector D. During writing of the fixable grating, the temperature of the $BaTiO_3$ crystal was set and maintained between 80°C and 110°C by a Peltier-effect heating/cooling module thermally coupled to miniature oil cell C (1 cc in volume). Once the cell settled (about 2 min after changing temperatures), the selected oil temperature was maintained by

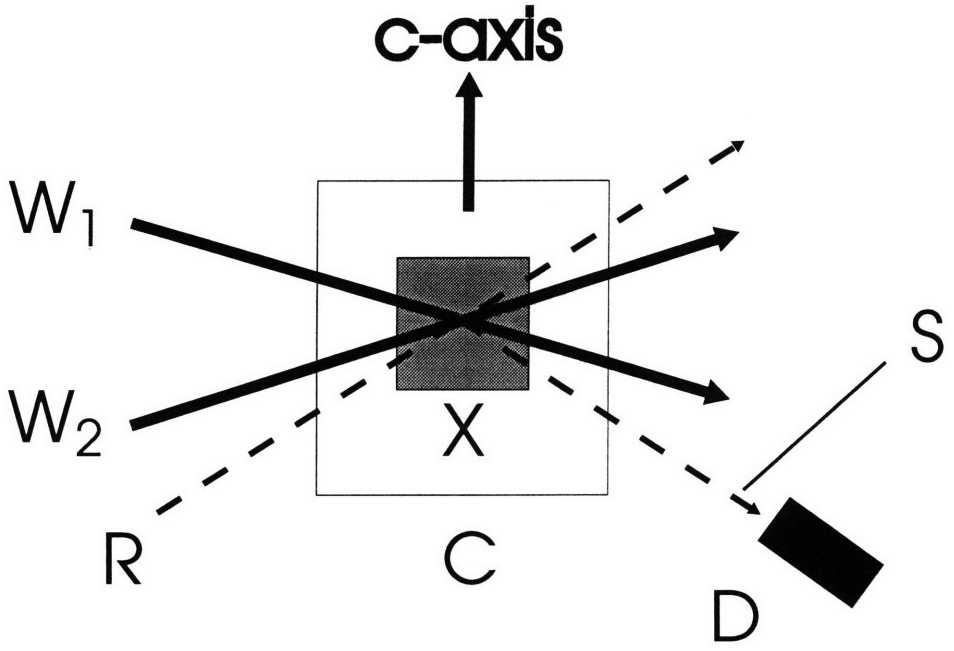

Figure 5.1: Experimental geometry for writing semipermanent holograms in $BaTiO_3$ at elevated temperatures. Legend: W_1 and W_2 are 514 nm writing beams, R is a 633 nm readout beam, S is the 633 nm beam diffracted by gratings in the crystal, F is a narrow-band interference filter centered at 633 nm, D is a detector, X is the $BaTiO_3$ crystal, and C is the temperature-controlled oil cell.

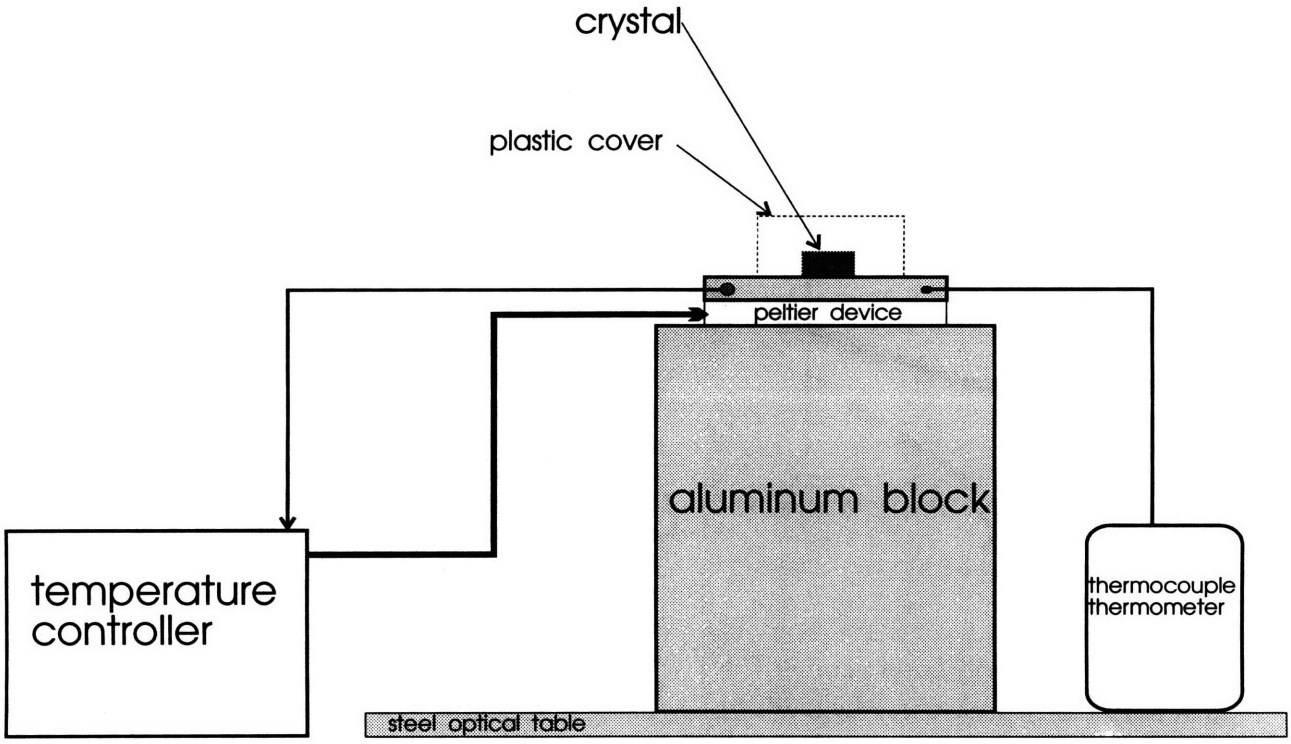

Figure 5.2: Temperature control setup for writing, fixing, and erasing secondary gratings in $BaTiO_3$.

a linear proportional controller to ± 0.2 C°. The oil cell was surrounded by a small insulating box with glass windows to let the beams pass in and out (see Fig. 5.2). We did not apply any voltage to the crystal during these experiments.

At low temperatures ($T < 80°C$), with W_1 and R left on at all times, the diffraction efficiency rose monotonically (see Fig. 5.3) when writing beam W_2 was turned on. After writing beam W_2 was turned off, we observed a rapid monotonic decay of the diffraction efficiency.

In several of the crystals investigated, heating above about 80°C lead to a dramatic change in the time evolution of the diffraction efficiency. Experimental results are shown in Fig. 5.4 for a reduced 1000 ppm Fe-doped crystal heated to 100.3°C. The diffraction efficiency initially rose but then slowly dropped off. After 80 sec., W_2 was turned off and the uniform intensity of W_1 quickly erased any photoconductive gratings. Nevertheless, the diffraction efficiency rebounded quickly to a peak before decaying slowly to zero (see Fig. 5.4).

5.3.2 Discussion

Because of the drastic change in decay time of the secondary gratings over the temperature range investigated, it is reasonable to assume that the secondary gratings in this crystal were due to a temperature-activated ionic mobility of the form

$$\mu(T) = \mu_\infty e^{-T_0/T}, \tag{5.1}$$

where μ_∞ and T_0 are constants determined by a least-squares fit to the decay curves shown in Fig. 5.5. The quantity $E_A = k_B T_0$ is the activation energy which must be overcome for a mobile ion to hop to a new site. (k_B is the Boltzmann constant.) E_A is equal to the slope of the mobility curve on the Arrhenius plot (Fig. 5.6). As Fig. 5.6 shows, the best-fit activation energy for the ionic mobility was approximately 1.8 eV.

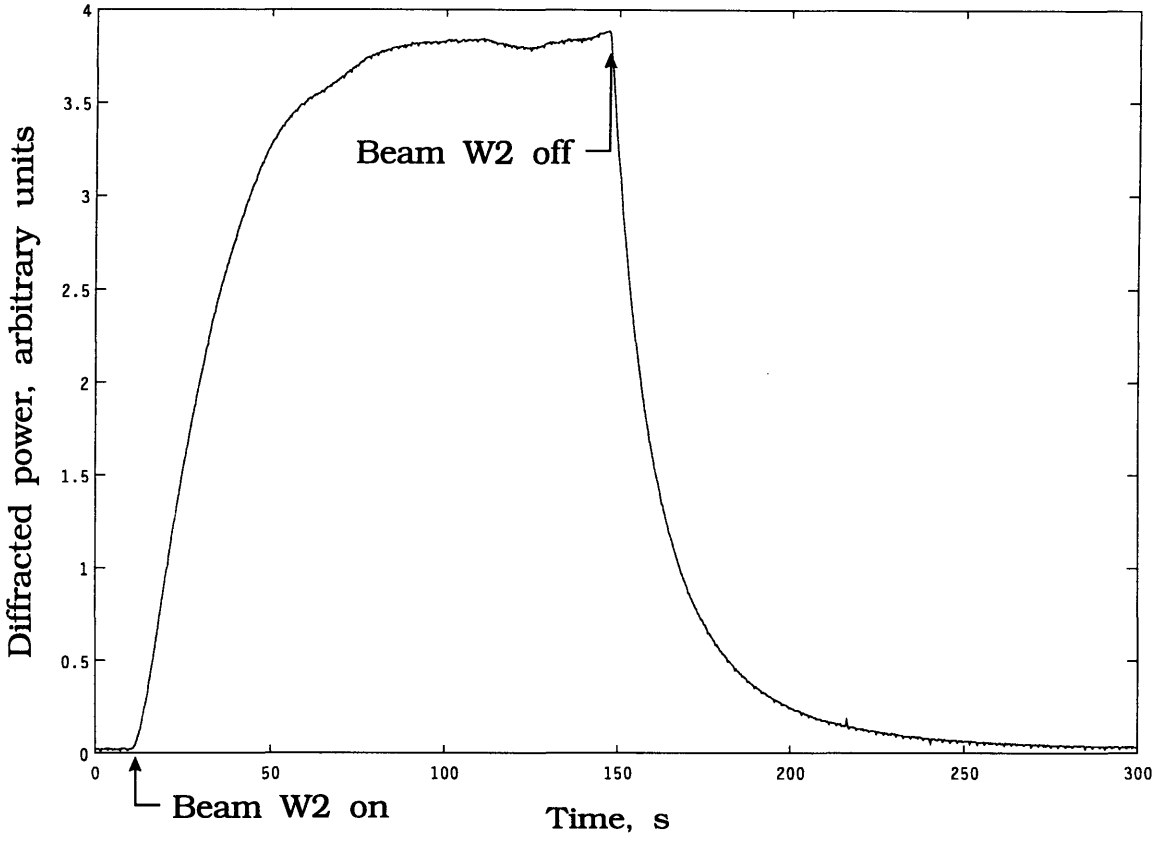

Figure 5.3: Measured diffracted power from a He-Ne laser at 633 nm (see Fig. 5.1) versus time in a reduced $BaTiO_3$:Fe (1000 ppm) time at low temperature (T = 60.1°C), where no ionic gratings form. Writing beam W_1 ON during entire run. When writing beam W_2 was turned on the diffraction efficiency rose. When it was turned off, the diffraction efficiency decayed.

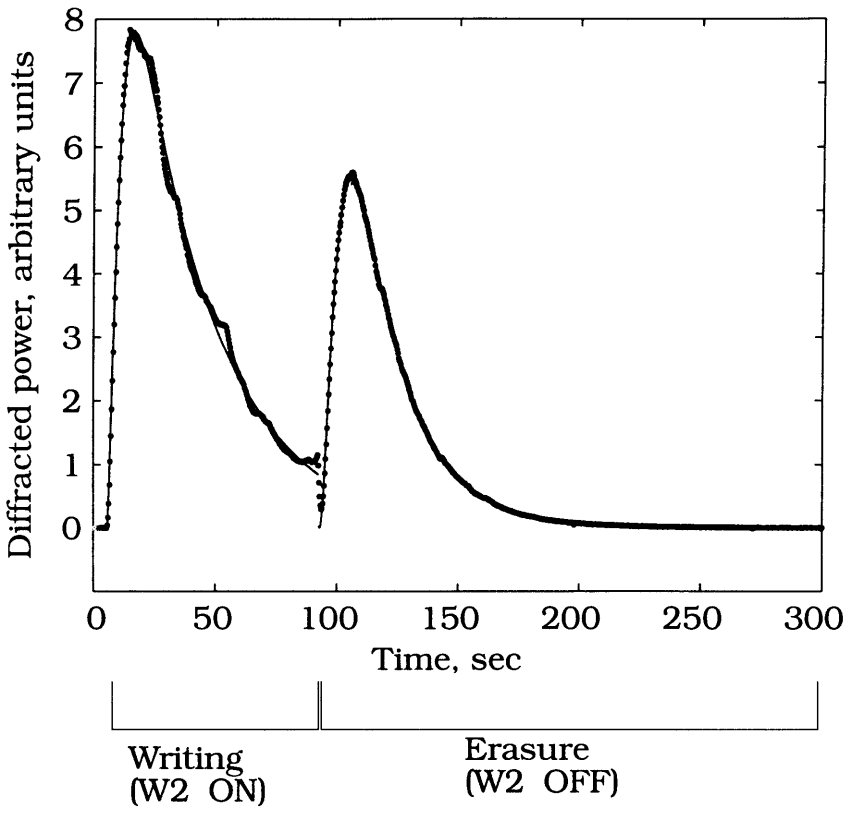

Figure 5.4: Points: Diffracted power from a He-Ne laser at 633 nm in a reduced $BaTiO_3$:Fe (1000 ppm) crystal over time, showing effects of large ionic gratings at 100.3°C. W_1 was on at all times. Thin lines: theoretical fits obtained by convolving the impulse response [Eq. (4.17)] with a boxcar function representing the optical field of W_2, then squaring to obtain intensity. The fitting parameters are: writing, $\tau_1 = 3.48$ s, $\tau_2 = 69.0$ s; erasure, $\tau_1 = 5.41$ s, $\tau_2 = 39.9$ s. The erasure response is much less noisy since it does not depend on 2-beam interference.

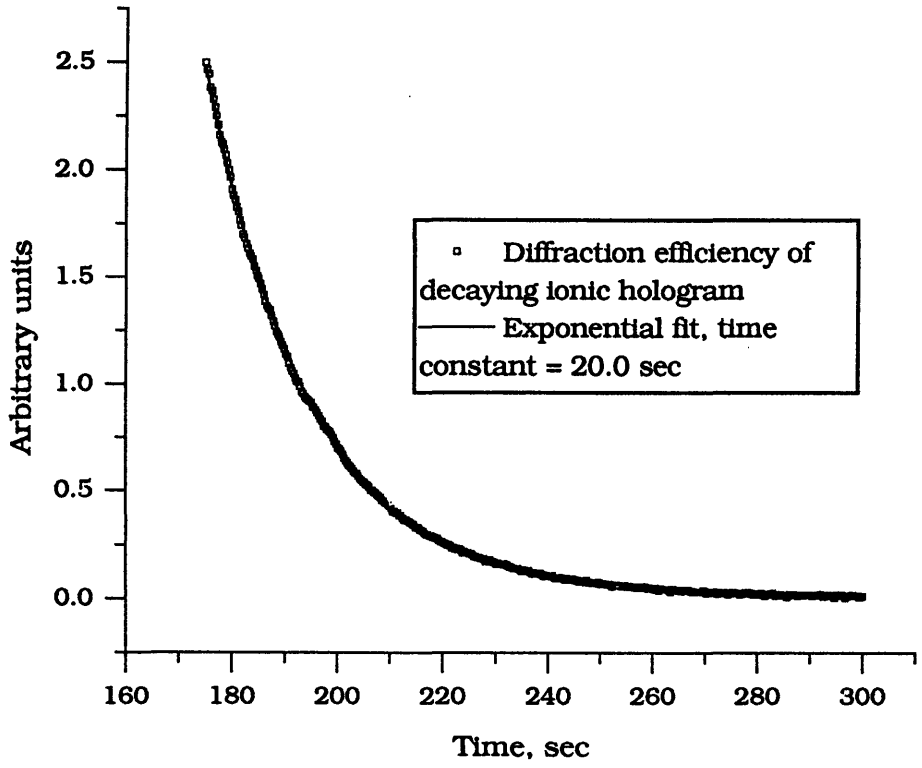

Figure 5.5: Sample time response of diffraction efficiency in the reduced $BaTiO_3$:Fe (1000 ppm) crystal #1462c during erasure of an ionic hologram at a grating period of 1.34μm. Fit: $\tau_I = 20.0$ sec.

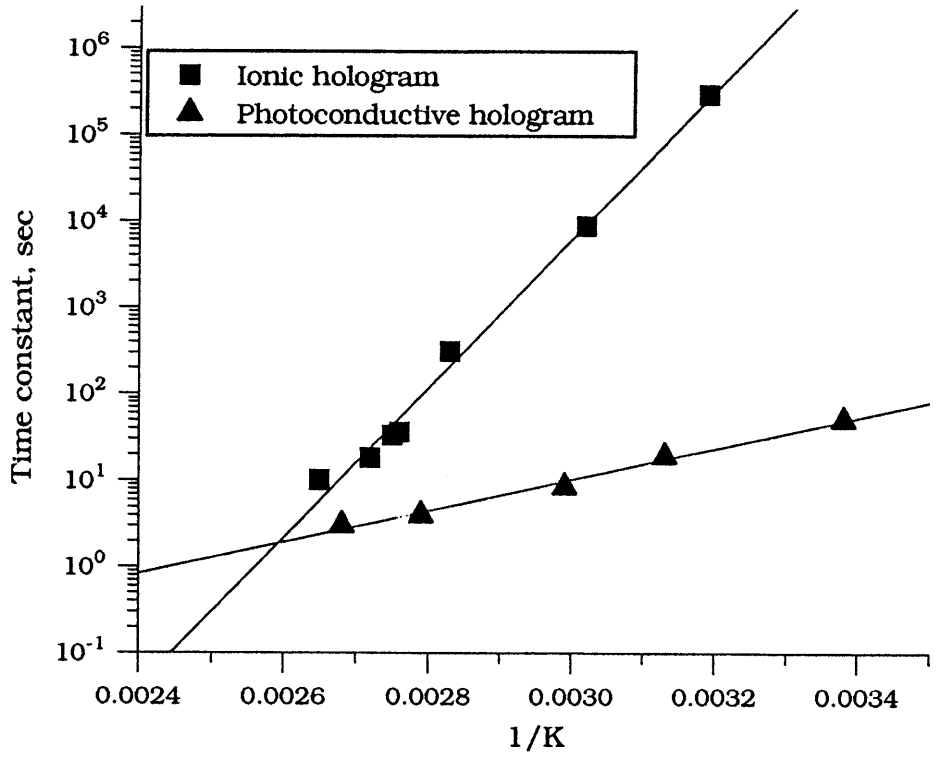

Figure 5.6: Squares: ionic hologram decay time constant as a function of inverse temperature. Fit: $E_A = 1.77$ eV. Triangles: photoconductive (driving) hologram decay times. Fit: $E_A = 0.36$ eV. Departure from activated time constant can be seen where the two time constants approach the same value (approximately 2 s).

Finally, we observed a different secondary grating response in another crystal, $BaTiO_3$:Fe (1000 ppm), as-grown (crystal 1462). In this crystal, significant secondary gratings became apparent at 55°C (see Fig. 5.7), while in other crystals temperatures of 80°C or more were necessary, and the complementary grating response clearly saturated short of completely cancelling the photorefractive grating.

5.3.3 Discussion

The differences between low- and high-temperature responses can be explained by the presence of a second charge-carrying species, mobile only at high temperatures [10, 15]. The ions drift in the space-charge field formed by motion of the holes. Since the secondary carriers are attracted toward primary carriers of the opposite sign, the secondary carriers form a complementary grating which partially cancels the electric field of the primary grating, explaining the first slow decay of the diffracted power. Erasing the primary grating at high temperature revealed slowly-decaying complementary gratings formed by carriers insensitive to light (perhaps mobile ionized defects), thus explaining the second rise in diffracted power seen in Fig. 5.4 [15]. We found no evidence of a coercive field threshold: complementary gratings showed similar response shapes at small and large amplitudes. Thus secondary gratings are apparently due to mobile ionized defects rather than local depoling of the crystal.

The activation energies of the two ionic species inferred from our measurements are 1.77 eV and 0.76 eV. In the literature, Wernicke reported a value of 2.05 eV for the activation energy of the mobility of $V_O^{\bullet\bullet}$ in $BaTiO_3$ ceramics at high temperatures [91]. Ionic transport measurements in $BaTiO_3$ and $SrTiO_3$ reflect an ambipolar diffusion process where holes (mostly occupying shallow traps) and ions move simultaneously [92]. The high concentration of trapped holes allows the high activation energy of

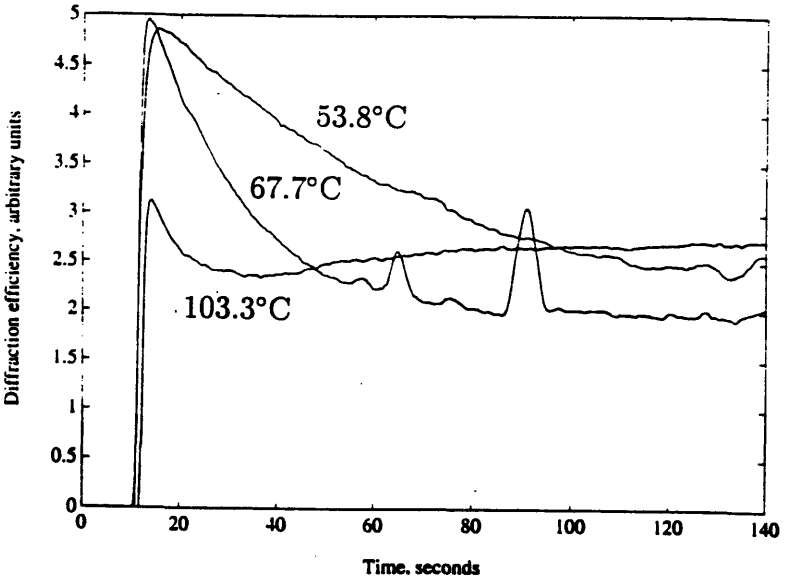

Figure 5.7: Time response of diffraction efficiency in the as-grown $BaTiO_3$:Fe (1000 ppm) crystal #1462 as a function of temperature at a grating period of 1.4μm, showing saturated complementary gratings, apparently due to a second type of ionic carrier, highly mobile even at 54°C. The complementary gratings can be seen to respond more rapidly at higher temperatures.

the ionic mobility to be measured in diffusivity measurements such as conductivity change on PO_2 jump [93]. Otherwise, at high temperatures the measured activation energy can be considerably lower due to ambipolar diffusion. In the experiments reported here, the temperatures are low enough that we expect to measure values of activation energy dominated by the ionic mobility activation energy. The reported mobility activation energy for protons is near 1.5 eV in $BaTiO_3$ ceramics and 1.1 eV in $SrTiO_3$ single crystals [93]. For both ionic species, it is expected that the activation energy will be lower in $BaTiO_3$ single crystals than in ceramics [94].

The presence of light at levels around 1 W/cm^2 in our experiments increases the concentration of excited but trapped holes, making the high-temperature activation energy appropriate [95].

Not all crystals showed this departure from a single-carrier time response at high temperature (see Table 5.1). Our Fe- and Ni- doped samples showed significant fixable secondary gratings at the highest doping levels (1000 ppma and 50 ppma, respectively), while undoped or lightly doped crystals from each of these series showed little or no fixing. The reduced 1000 ppma Fe-doped sample showed much stronger fixing than the as-grown 1000 ppma Fe-doped sample. Pure and Co-, Rh-, and V-doped samples likewise showed little or no secondary grating formation or fixing. The reasons for these apparent composition and processing dependences are not yet understood.

5.4 Readout of Fixed Holograms

The complementary gratings described above were fixed by rapidly cooling the crystal to temperatures between 10° and 40°C with the writing beams W_1 and W_2 either both on or both off. In our experiments so far, the usual write-fix-readout-erase cycle for

Crystal	σ_I	Fractional fixable diffraction efficiency	Temp.,°C	Λ (Grating Period)
1000 ppm Fe, reduced (1462c)		29%	100	3.9 μm
	1.1×10^{-11} $(\Omega cm)^{-1}$	80%	108	1.4 μm
1000 ppm Fe, as grown (1462)	1.8×10^{-14} $(\Omega cm)^{-1}$	NONE	110	3.9 μm
50 ppm Fe, reduced (1446B)		<0.1%	110	3.9 μm
50 ppm Ni (146A)	4.1×10^{-14}	15%	108	0.4 μm
		48%	100	0.6 μm
		20%	103	1.4 μm
		NONE	100	3.9 μm
25 ppm Ni (144A)		4.5%	106	1.4 μm
		NONE	101	3.9 μm
25 ppm Ni (144B)		small (<1%)	84	0.6 μm
10 ppm Ni (141C)		NONE	86	0.6 μm
Undoped,reduced (1434A)		very small	85	0.6 μm
Purified,reduced (2oF#16-2)		NONE	86	0.6 μm
50 ppm V (1o#25A)		NONE	110	1.4 μm
			100	3.9 μm
50 ppm V,reduced (1o#25A)		NONE	110	1.4 μm
			100	3.9 μm
'Blue' $BaTiO_3$ (2oF#18)		NONE	108	3.9 μm

Table 5.1: Fixing properties of selected $BaTiO_3$ crystals as a function of doping and experimental conditions.

ionic gratings has been as follows:

1. **Write:** With the crystal maintained at a constant temperature (typically between 80 and 110°C), writing beams W_1 and W_2 are unblocked, and the diffracted beam S is monitored until steady-state is reached.

2. **Fix:** With the writing beams still on, the crystal is quickly (within 30 s) cooled to below the writing threshold temperature Θ_W (about 80°C for 1000 ppm reduced $BaTiO_3$:Fe) so the ionic grating will no longer decay rapidly. Then W_1 and W_2 are blocked and cooling is continued until the selected readout temperature is reached.

3. **Store:** With crystal temperature maintained as low as possible within the tetragonal phase (i.e. greater than about 9°C), the fixed gratings can be stored for very long periods. However, we have observed that readout will be inefficient below a readout temperature threshold Θ_R (about 40°C for the reduced 1000 ppm Fe-doped crystal with its c-axis oriented 14° from the grating vector).

4. **Readout:** With crystal temperature maintained at the desired readout value above Θ_R, the diffracted signal beam S can be read out nondestructively by the reference beam R. The readout Bragg angle may be slightly different from its former value at the writing temperature, due to thermal expansion and other effects. Storage time is longer at lower temperatures.

5. **Erase:** The crystal is reheated to the writing temperature with the writing beams still blocked, and the diffracted signal beam is monitored until it effectively drops to zero. At this point the ionic grating recorded in steps 1–3 above has been erased and the cycle can be repeated.

In the Fe- and Ni-doped crystals with substantial complementary-grating response, gratings could be fixed by rapid (about 30 s) cooling to temperatures below 80°C (see Fig. 5.10). Good fixing results were obtained with the writing beams either on or off during cooling. As shown in the Fig. 5.10, 514 nm light cannot erase the fixed grating, at least at intensities near 1 W/cm^2. In fact, for the crystal orientation shown the He-Ne laser diffraction efficiency actually increased on exposure to the 514 nm writing beam W_1. We believe that this might be explained by photorefractive two-beam coupling between the 514 nm writing beam and the beam diffracted from the writing beam by the fixed grating [10, 96]. In our model: (1) a single writing beam is diffracted by the fixed grating, reconstructing the other writing beam within the crystal, (2) beam coupling takes place between the original and the reconstructed writing beams, (3) a photorefractive grating is written: if the diffracted beam propagates toward the +c-axis of the crystal, the photorefractive grating written as W_1 and the diffracted beam interfere to selectively reinforce the fixed grating; (4) the 633 nm readout beam diffracts from the combined fixed and photorefractive gratings more efficiently than it did from the fixed grating alone.

We also found that when a crystal supporting fixed gratings is cooled to room temperature, the diffraction efficiency is very low ($\ll 1\%$). But when the crystal is reheated to the writing temperature, the diffraction efficiency of the fixed grating briefly recovers to values comparable to those of the complementary gratings originally observed before cooling (see Fig. 5.8). (Of course the ionic hologram is no longer fixed at this temperature, so this initially high diffraction efficiency decays.) In this experiment, the Bragg readout angle was maintained by re-maximizing the diffracted beam at several different temperatures (to compensate for thermal expansion). In particular, no amount of care in the Bragg angle adjustment gave any significant

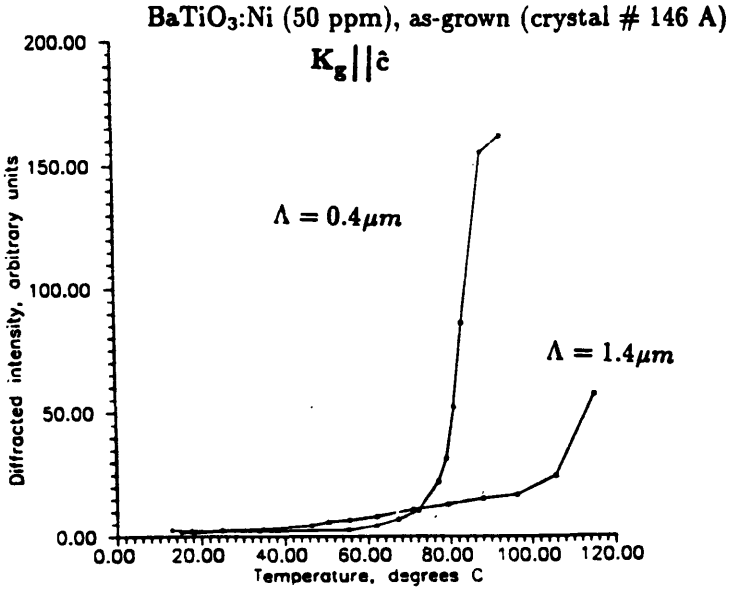

Figure 5.8: Diffraction efficiency of a fixed grating in an as-grown $BaTiO_3$:Ni (50 ppm) crystal as a function of reheating temperature for several grating periods, at constant intensity. Because these curves are reversible without rewriting the grating, charge compensation at low temperatures is believed to be responsible for the drop-off in diffraction efficiency.

improvement in the room-temperature diffraction efficiency (which was very low). The near disappearance of the diffracted beam at low temperatures and its return at high temperatures could be observed repeatedly without rewriting the grating. The proportional rise is far too great to be explained by the temperature dependence of the refractive index and electrooptic coefficient. This suggests that our initial cooling was rapid enough to fix most of the charge of the complementary grating in place before it could decay, but that a temperature-dependent compensation mechanism cancels the fixed component of the electric field at room temperature. Temperature-dependent reinforcing gratings due to beam coupling between the readout and diffracted beams may also be a factor.

The curve of diffraction efficiency as a function of temperature, shown in Fig. 5.8, was found to depend upon the period of the fixed grating. Impractically small grating periods would have been required to obtain high diffraction efficiency at or near room temperature for this crystal orientation.

Since high diffraction efficiency simultaneous with long storage time (which demands low-temperature operation) was not possible in the standard orientation ($\mathbf{K}||\hat{\mathbf{c}}$), fixing experiments were carried out in several oblique orientations. In these experiments, the angle θ between the grating vector and the c-axis, zero in the standard orientation, was increased by rotating the crystal about its vertical a-axis (see Fig. 5.9). The goal here was to increase the effective dielectric constant $\epsilon_{\text{eff}} = \epsilon_c \cos^2\theta + \epsilon_a \sin^2\theta$, where $\epsilon_c \simeq 150$ and $\epsilon_a \simeq 3600$ at room temperature. The results were very rewarding (see Fig. 5.9). We found that the temperature threshold for efficient readout could be lowered from $\sim$80°C at least to $\sim$40°C by rotating the crystal to make $\theta = 14°$. (Further rotation was not practical in the setup used.) This made the long storage time shown in Fig. 5.10 possible in conjunction with reasonably high diffraction efficiency.

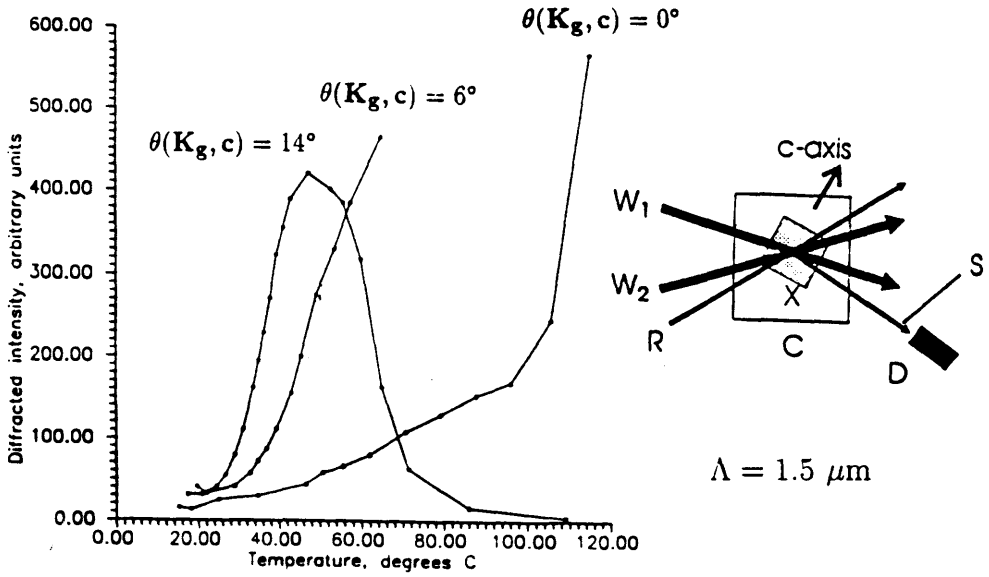

Figure 5.9: Power diffracted by a fixed grating as a function of reheating temperature for several crystal orientations, at constant intensity. Reduced $BaTiO_3$:Fe (1000 ppm).

Another advantage of oblique orientations is that the large electrooptic coefficient ($r_{42} \simeq 1640$ pm/V at room temperature) can be accessed for efficient readout of the charge gratings.

5.5 Storing and erasing fixed holograms

5.5.1 Experiments and Results

We also conducted erasure experiments where the decay of the diffraction efficiency was measured as a function of time for several temperatures. As shown in Fig. 5.11, the best-fit activation energy was approximately 0.76 eV. This activation energy is also substantially lower than that of the "high-temperature" secondary gratings typically observed above 80°C (1.77 eV). This same as-grown iron-doped crystal also showed weak complementary gratings of the type seen in the other Fe- and Ni-doped $BaTiO_3$ crystals in our study. Complementary gratings recorded above 100°C in this crystal persisted for hours at 55°C, while those recorded below 80°C decayed in minutes at 55°C. Finally, we observed a "double rebound" in the decay of secondary and 'tertiary' gratings in this crystal (see Fig. 5.12).

5.5.2 Discussion

The transient response shown in Fig. 5.12 cannot be obtained from a second-order system with two poles on the real axis, since the rebound in the step response in that case consists of cancellation between two decaying exponentials with different time constants. Three poles are necessary to explain two rebounds. Thus the simplest possible step response which will explain the data consists three distinct decaying exponentials, corresponding to a crystal supporting three distinct gratings. In view of the above observations, it is reasonable to assume that two distinct light-insensitive

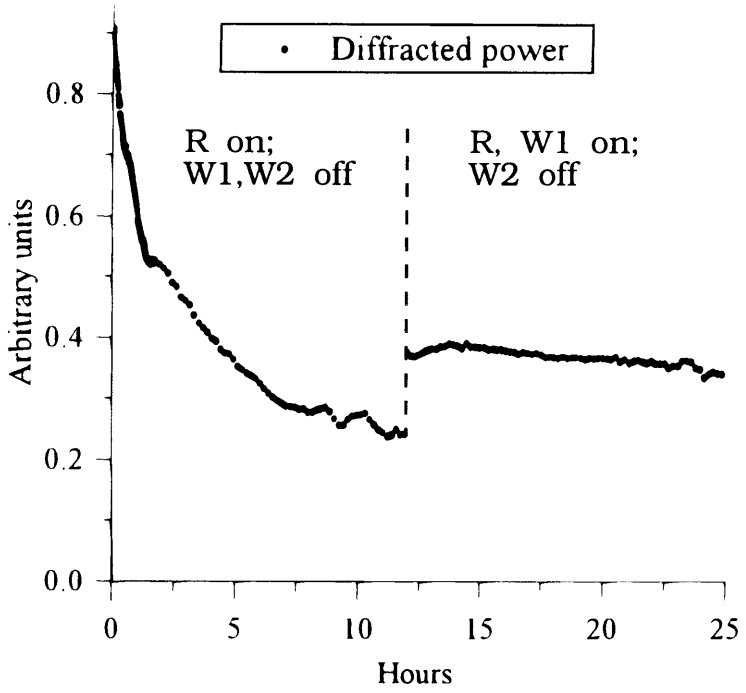

Figure 5.10: Diffraction efficiency versus time after fixing by cooling to a readout temperature of 39.7°C, for an ionic grating formed oblique to the c-axis ($\theta(\mathbf{k}_g, \hat{\mathbf{c}}) = 14°$) of a reduced $BaTiO_3$:Fe (1000 ppm) crystal. The single 514 nm beam W_1 was off for the first 12 hours and on for the last 12 hours. W_2 was always off. The peak diffraction efficiency shown was measured to be roughly 2% The storage time is predicted to be 300 days at 15°C in this crystal. Lighter doping leads to longer storage times.

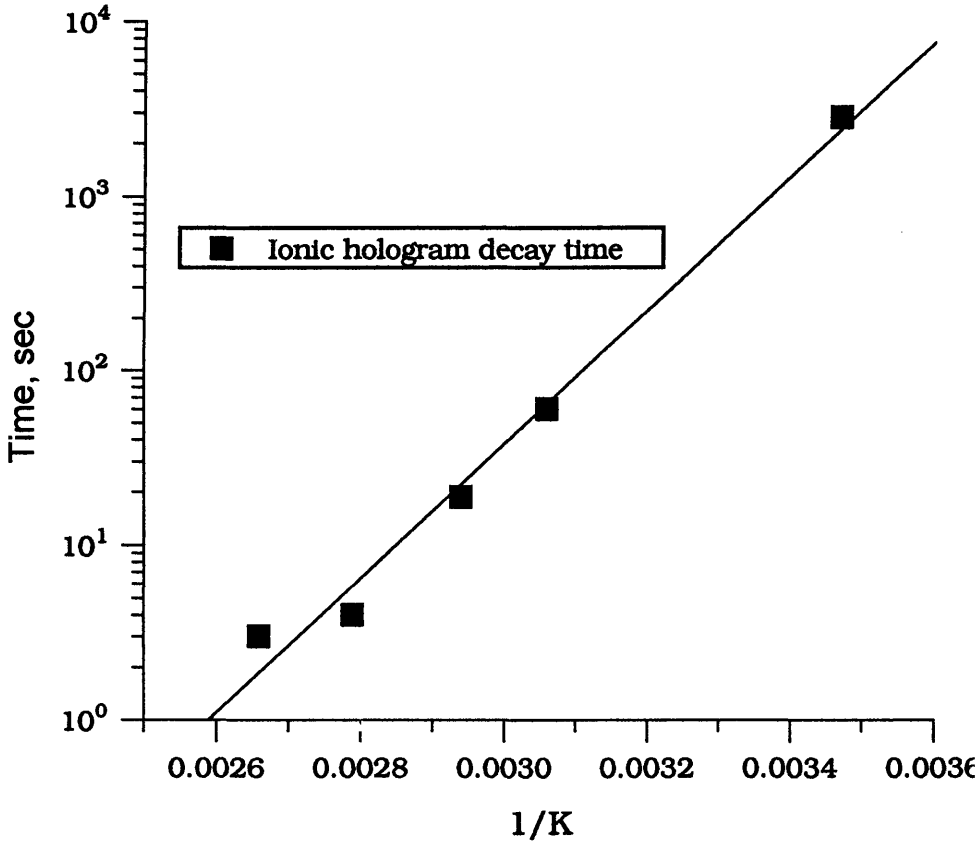

Figure 5.11: Log measured secondary grating decay time constant as a function of inverse temperature. A least-squares fit line with a slope corresponding to an activation energy of 0.76 eV is also shown.

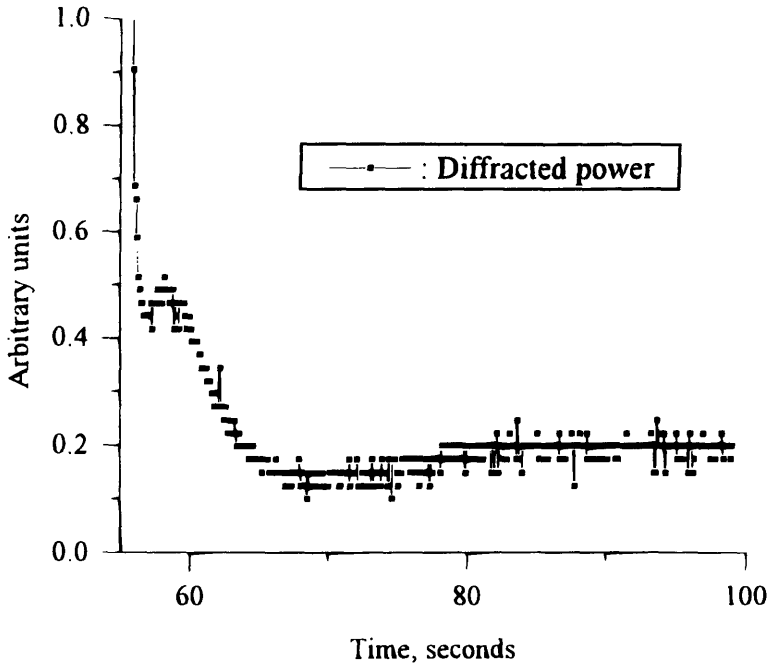

Figure 5.12: Double rebound of the diffracted power versus time in as-grown iron-doped $BaTiO_3$ crystal #1462 at 103.3°C. The writing beams were turned off at $t = 0$ sec. This response is consistent with the expected response of a crystal with two ionic gratings having different decay times.

charge carriers can be activated in $BaTiO_3$:Fe. Since a high activation energy allows a greater range of ionic conductivity between the writing and storage temperatures for fixed gratings, the type I carriers are clearly more suitable for fixing applications.

5.6 Conclusions

This chapter has covered the experimental work done in order to (1) determine how to control doping, orientation, temperature and timing to obtain a combination of short writing times, long storage times and high diffraction efficiency, and (2) asses the suitablility of $BaTiO_3$ as a holographic storage medium. A number of new qualitative and quantitative questions about using $BaTiO_3$ for hologram fixing were answered by looking at the data reported in this chapter. The main points were:

1. The playback diffraction efficiency decreases reversibly as the crystal is cooled. Storage time increases as the crystal is cooled. Therefore optimum storage and readout temperatures are not necessarily equal in $BaTiO_3$.

2. The temperature dependence of the diffraction efficiency can be controlled by changing grating period and crystal orientation.

3. Pure crystals are not useful for fixing. There is a correlation between Fe and Ni doping and fixing.

4. Two species of thermally activated secondary light-insensitive charge carriers with different activation energies have been identified.

5. Ionic conductivities and activation energies have been measured by optical holographic experiments, using a curve-fitting formula to analyze the measured step response of the diffraction efficiency.

6. Ionic number density estimates have been made for the $E_A = 0.76eV$ ionic carriers (possibly H^+ ions) and for the $E_A = 1.77eV$ ionic carriers (probably singly ionized oxygen vacancies $V_O^{\bullet}$). (The only other likely ionic carriers in $BaTiO_3$ are barium vacancies, with an activation energy of about 2.4 eV [80].) These results and impurity doping information have been used to obtain information about the identities of the carriers.

A thermally activated hologram fixing process was developed in order to optimize $BaTiO_3$ crystals as erasable and rewriteable nonvolatile hologram storage media. The stored holograms can represent digital data, analog images, or optical interconnects. In order to make such a medium as useful and versatile as possible, the following functions should be available (and should be obtainable without removing the crystal from its optical system): (1) recording, (2) fixing, (3) playback, (4) storage, (5) erasure.

The full record-fix-playback-store-erase cycle is as follows. First, a completely erased crystal is heated to the writing temperature (usually above 100°C). An information-bearing wave and a reference wave are interfered to record a photorefractive hologram in the $BaTiO_3$ crystal. If a single hologram is being stored, the recording process is allowed to reach steady-state. If instead many multiplexed holograms are being stored, the recording time for each is chosen according to a schedule designed to ensure equal diffraction efficiencies. When recording is completed, the light beams are blocked and the crystal is quickly (about 1°C per second) cooled to the selected playback temperature (usually below 40°C). Now the holograms can be read out at high diffraction efficiency and without optical erasure. Storage time is not optimal, however, until the temperature has been lowered as far as possible. With this in mind, a storage function can be implemented. To obtain the longest possible storage time, the crystal is

cooled to approximately 10°C, approaching the tetragonal-orthorhombic phase transition (near 5°C in undoped crystals). Because diffraction efficiency decreases when the temperature is lowered, however, the best temperature for long-term storage may not always be high enough for efficient hologram playback. This trade-off will of course depend upon the requirements of each application. The playback/storage operations can be cycled until the stored holograms fade. Finally, all holograms stored in a given crystal can be erased together by reheating to the recording temperature and allowing a suitable amount of time to pass (a few seconds to a few minutes).

Chapter 6

CONCLUSIONS

6.1 Fixing in $BaTiO_3$

Original experimental results reported in this thesis include: (1) High diffraction efficiciency (> 10 %) was obtained in thermally fixed holograms in $BaTiO_3$. Unlike electrically fixed holograms [9], these holograms can be read out as often as desired. (2) A correlation was found between specific dopants (Fe and Ni) and strong fixable complementary grating response. (3) The diffraction efficiency of fixed holograms in $BaTiO_3$ was shown to be strongly dependent on temperature, grating period and crystal orientation. This is apparently due to nonequilibrium low-temperature screening by shallow traps [83, 84]. (4) The thermal fixing process in $BaTiO_3$ was improved by separating the readout and storage steps. (5) Two different thermally-activated mobile ionic species have been used to fix holograms in a single $BaTiO_3$ crystal. Evidence is presented to suggest that the two ions are (a) singly-ionized oxygen vacancies (E_A=1.77 eV), and (b) hydrogen ions bound to oxygen atoms in the lattice (E_A=0.76 eV).

From an applications point of view, point (3) was the most important and novel. It was shown that crystal orientation can be used as a non-destructive substitute for the revealing field of thousands of V/cm otherwise needed to obtain high diffraction effi-

ciency at room temperature from fixed holograms in $BaTiO_3$ [9]. The same technique should apply to other highly anisotropic photorefractive media with shallow traps (such as doped SBN and $KNbO_3$). The activation energy of the oxygen vacancies is considerably higher than for mobile ions in $LiNbO_3$ (1.77 vs. 1.33 eV [97]). Current experimental work on storing images [5] and data [98] has mostly been performed with $LiNbO_3$. The fixing process in $LiNbO_33$ is well-understood [97, 99, 100, 11, 12]. Shallow-trap nonequilibrium screening effects [83, 84] during readout in $LiNbO_3$ are much less prevalent than in $BaTiO_3$, probably due to the much shorter excited carrier lifetime. In $BaTiO_3$, a very high storage/write time ratio ($\tau_s/\tau_w = 10^8$) can be obtained in a relatively small temperature range (15°C to 120 °C). Fixing in $LiNbO_3$ requires much higher writing temperatures. Everything else being equal, it is better not to write holograms at 200°C. Finally, the largest electrooptic coefficient that can be obtained from space charge in $BaTiO_3$ is approximately $1.5 \times 10^{-8} cm^2/C$ (with E 15° from the c axis). This can be compared with the maximum value in $LiNbO_3$ of $0.6 \times 10^{-8} cm^2/C$. Since the diffraction efficiency of a photorefractive hologram is proportional to the square of the electrooptic coefficient, equal space charge yields a diffraction efficiency that is 6 times in higher $BaTiO_3$ than in $LiNbO_3$.

Some theoretical results were also derived: (6) A general solution to the beam coupling problem in the undepleted pump regime was found. This solution applies formally to any beam coupling medium, including the two- and three-carrier photorefractive media encountered when writing ionic holograms. (7) A standard defect chemistry model was used to support the hypothesis that the mobile ions detected in most $BaTiO_3$ samples were singly-ionized oxygen vacancies. (8) A simplified theory has been developed from the one proposed by Montemezzani et al. [14, 15]. The theory assumes writing and erasure of secondary gratings in photorefractive crystals

are due to transport of ions in the space-charge field of the primary photorefractive grating. In the simplified theory, photoconductivity is treated in the steady-state, reducing the number of dynamic variables to two. In the usual case where the two time constants are clearly distinct (by a ratio $\simeq$ 5:1 or more), then one applies to the hole grating and the other to the ion grating. A two-pole system response follows in the linearized case, and excellent agreement was observed between the theory and measured data. In some crystals two different secondary gratings have been observed. This corresponds to a three-pole response and was explained by a straightforward extension of the theory.

6.2 Optimal operating temperature in $BaTiO_3$

High writing temperatures are essential to any thermal fixing process for photorefractive holograms. In order to record holograms effectively, we rely on our understanding of the photorefractive process. A fact of life that accompanies thermal fixing is that photorefractive properties are temperature dependent, and engineering decisions based on low-temperature measurements are almost certain to be faulty. In order to deal with this situation, the photorefractive properties of the crystals used for storage of fixed holograms were characterized as a function of temperature. Several interesting facts came to light as a result of these investigations. First, as reported by other workers [21], the maximum photorefractive sensitivity of $BaTiO_3$ increases one to two orders of magnitude in the neighborhood of 100°C with respect to its value at room temperature. Second, the optical absorption spectrum changes its shape with temperature in a surprising fashion. Exponential absorption tails are observed to grow more spread out as $BaTiO_3$ crystals are cooled. This is contrary to the temperature dependence associated with the Urbach tail mechanism often used to explain

band-tail phenomena.

6.3 Future work

Certainly further crystal growth and annealing studies would be very helpful in verifying the information presented in this thesis on doping and annealing for high ionic conductivity in $BaTiO_3$. In particular, a series of progressive reduction treatments on the remaining heavily Fe- and Ni-doped crystals would be of value. Unfortunately, there are only one sample each of 1000 ppm Fe and 50 ppm Ni remaining, so conducting a series of reduction experiments would be risky. Annealing treatments should also be capable of eliminating H^+ ions by drying the crystals, confirming or eliminating H^+ as the identity of the low-temperature 0.76-eV ions.

A technique that might be explored is to apply a d.c. electric-field parallel to the K vector during readout of *screened* fixed gratings at room temperature [10]. This process would take advantage of the nonuniform carrier lifetime which results from excess carrier storage in (lifetime-limiting) traps. If the ionic grating has been fully screened, this means that (assuming the ionic writing process was drift-dominated), the density of empty deep traps will be

$$N_A^-(x) = [N_A^-]_0(1 + m\cos Kx), \tag{6.1}$$

just as during ionic-drift-dominated writing (Eq. (6.1)). Since the carrier lifetime is inversely proportional to the number of traps, Eq. (6.1) implies a spatially varying resistivity $\rho(x)$ under uniform light intensity I:

$$\rho(x) = \frac{1}{q\mu p} = \frac{1}{q\mu}\frac{\gamma N_A^-(x)}{sIN_A^0} = \frac{1}{q\mu}\frac{\gamma}{sIN_A^0}[N_A^-]_0(1 + m\cos Kx), \tag{6.2}$$

where sIN_A^0 is the generation rate and $(\gamma N_A^-)^{-1} = \tau_R$ is the carrier lifetime.

If a dc electric field E_0 is applied to the crystal in the direction of the grating vector, in steady-state a constant current will flow. The electric field within the crystal will be proportional to the resistivity. At suffiently small m, the electric field within the crystal will be (from (6.2)):

$$E(x) = E_0(1 + m\cos Kx). \tag{6.3}$$

Eq. (6.3) states that the amplitude of the space-charge field will be a fraction m of the applied field. Since (6.3) is only quantitatively correct for $m << 1$, it will be necessary to perform experiments to determine what fraction of the applied field can actually be observed in the a.c. space-charge field as $m \to 1$.

Reduction of storage time on application of a revealing electric field has been reported by other workers [101]. Special care should be taken to measure this effect, if it is observed. If the applied field significantly influences decay times, this would seem to invalidate the ionic conductivity hypothesis for fixed grating storage and support a partial-depoling hypothesis.

A major goal of the fixing experiments preformed in this thesis was to remove the lower bound on the readout temperature (imposed by low-temperature screening). This goal was achieved without resorting to application of high voltage to the crystals (high voltage can cause damage to brittle semiinsulating crystals).

There are two other important factors that must be considered for efficient readout:

1. Choice of electrooptic coefficients r_{eff} for readout of the fixed space-charge electric field. This is determined by crystal orientation. (The refractive index change which can be achieved is $\Delta n = \frac{1}{2}n_0^3 r_{eff} E_{sc}$, where n_0 is the zero-field refractive index and r_{eff} is the effective linear electrooptic coefficient.)

2. Minimization of the two-beam coupling gain between the writing beams (be-

cause the intensity ratio of coupled writing beams cannot be maintained at a constant, optimized value as the beams propagate through the crystal [70]).

Our fixed-grating readout experiments both with and without an applied electric field have been concentrated on oblique orientations (k_g neither parallel nor perpendicular to $\hat{\mathbf{c}}$) which allow access to the largest electrooptic coefficient r_{42} for an extraordinary-ray readout beam. The writing beams can then be of ordinary polarization so that their mutual coupling gain will not be too large. As a special case, in the anisotropic writing configuration ($k_g \perp \hat{\mathbf{c}}$), beam coupling between the writing beams is forbidden but efficient, low-noise cross-polarization scattering readout through r_{42} becomes possible. [102]. This orientation has also been investigated in our fixing experiments. Unfortunately the fixed gratings recorded in this orientation decay in a few hours in $BaTiO_3$. Kirillov and Feinberg also noted this fact [16]. Further efforts to understand why room-temperature erasure is possible in this orientation would probably be valuable.

Finally, the worst feature of $BaTiO_3$ for data storage applications at this time is its extremely high cost. $BaTiO_3$ is well suited to this application because of its enormous electrooptic coefficients, but it is a difficult material to grow and process, when compared to $LiNbO_3$ or most other photorefractive materials. Techniques developed in this research might be used to enhance fixing in less expensive materials, or select candidate materials.

Appendix A

INFRARED-SENSITIVE GREEN AND BLUE $BaTiO_3$

A.1 Rhodium doping for infrared sensitization

Recently, we have grown $BaTiO_3$:Rh crystals which have high gains and fast writing response at near-infrared wavelengths. These blue crystals, originally produced by accident when Pt-Rh wire attaching the seed crystal to the pulling rod fell into a growth melt in a Pt crucible, have been reproduced by adding measured amounts of Rh metal to an otherwise undoped $BaTiO_3$ growth melt. The absorption spectrum of one of these blue crystals is shown in Fig. A.1. The absorption at 850 nm is several inverse centimeters, which could account for the greatly enhanced photoconductivity at 850 nm as compared with crystals grown from the same original source material before Rh doping. Face reflections were accounted for by assuming a single reflection at each interface and using the Sellmeier formula and coefficients given by Wemple et al. [55].

The dominant impurity concentrations detected in a spark-source mass spectroscopy analysis of this material are listed in Table A.1. The boules were aligned by x-ray diffraction, then sawed into rectilinear crack-free pieces. These pieces were poled by the etching method [103] and polished on opposite faces for optical characterization.

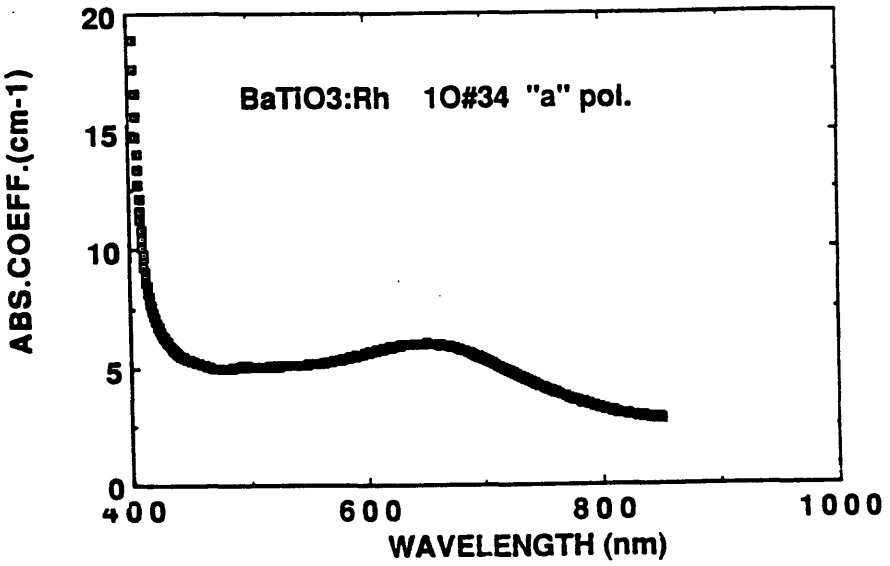

Figure A.1: Absorption spectrum of as-grown blue $BaTiO_3$:Rh crystal #1o34, showing peak at 650 nm.

A.2 Infrared photorefractive characterization of blue $BaTiO_3$: Rh

Because no convenient safe readout wavelength could be found for diffraction-efficiency measurements in these infrared-sensitive crystals, photorefractive characterization was carried out by two-beam coupling (see Fig. A.2). We measured the extraordinary-wave beam-coupling gain of the blue $BaTiO_3$:Rh crystal #1o34 at 840 nm, for several grating vectors parallel to the c-axis. The intensity of the pump beam W_1 was 550 mW/cm^2 and the intensity of the probe beam W_2 was 71 mW/cm^2. Both beams were controlled by shutters. The crystal under test was placed in an oil-filled cuvette to minimize heating by absorbed laser light. The K-vector of the grating was kept

Element	PPM by weight, undoped $BaTiO_3$ crystal 2oF#4	PPM by weight, blue $BaTiO_3$:Rh crystal 2oF#18	Ratio: ppmw after Rh doping/ ppmw before Rh doping
Na	≤ 25	≤ 25	~ 1
Mg	≤ 25	≤ 25	~ 1
Al	0.3	10	30
Si	≤ 3	≤ 3	~ 1
S	1	1	1
Cl	0.8	0.8	1
Ca	30	6	0.2
V	0.2	<0.2	~ 1
Fe	0.6	1	1.7
Ni	≤ 0.7	0.7	~ 1
Cu	0.3	0.3	1
Sr	>2000	>2000	uncertain
Rh	0.5	2	4
La	≤ 0.9	≤ 0.9	~ 1
Pb	0.5	<0.5	~ 1

Table A.1: Measured impurity concentrations by weight in undoped $BaTiO_3$ crystal 2oF#4 and blue $BaTiO_3$ crystal 2oF#18 (impurities present at levels ≥ 0.2 ppmw, as measured by spark-source mass spectroscopy analysis). The third column shows ratios of detected impurity concentrations before and after doping. The high level of Al is due to the alumina seed rod making contact with the melt. Infrared sensitive blue crystals have been reproduced by adding Pt-Rh wire to the melt without allowing this Al contamination to occur. Measurements performed by Northern Analytical Laboratories, Merrimack, NH.

parallel to the c-axis of the crystal at all times, and the grating period was varied by moving a symmetrical pair of mirrors. To ensure that the two infrared writing beams were mutually aligned, they were first both adjusted to shine through a pinhole adjacent to the crystal. After this was done, the pinhole, cuvette and crystal were moved sideways together on a micrometer-driven translation stage so that the pinhole was replaced by the crystal, and the writing beams intersected accurately within the crystal. In each beam-coupling run, the detected intensity was first allowed to stabilize with beam W_2 on and W_1 off. After this occurred, W_1 (the pump beam) was turned on and the time evolution of the detected intensity was monitored using a silicon photodiode.

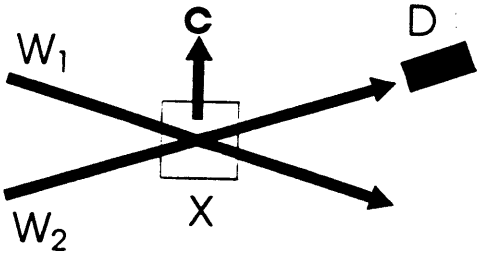

Figure A.2: Setup for measuring the infrared beam coupling response of $BaTiO_3$:Rh at 840 nm. Legend: W_1 and W_2 are 840 nm writing beams, D is a detector, X is the $BaTiO_3$ crystal, and C is an oil-filled cuvette at room temperature.

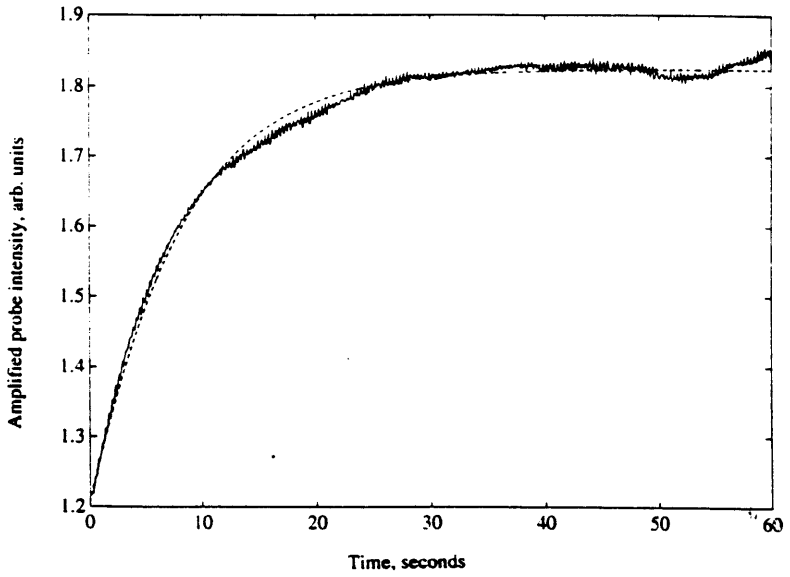

Figure A.3: Extraordinary-wave beam coupling time response of as-grown blue $BaTiO_3$:Rh crystal #1o34 at a wavelength of 830 nm, a spatially-averaged intensity of 620 mW/cm^2 and a grating period of 1.2 μm (solid curve). Dashed curve: least-squares theoretical fit yielding time constant $\tau = 7.5$ s and gain $\gamma = 3.2$ cm^{-1}. The crystal thickness is 1.2 mm.

Fig. A.3 shows the time evolution of the transmitted probe beam in a representative beam coupling measurement using an extraordinarily polarized 830 nm wavelength

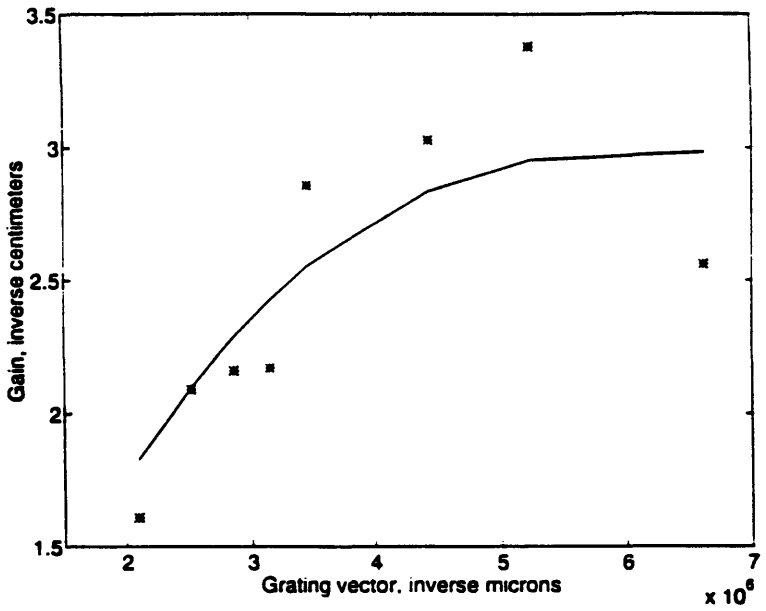

Figure A.4: Preliminary beam coupling gain data for blue crystal at 850 nm, as a function of grating period. Also shown is a least squares curve fit to the function [27] $\gamma(k) = 2\gamma_0 k_0 k/(k^2 + k_0^2)$, where $\gamma_0 = 3.0$ cm^{-1} is the peak gain on the theoretical fit curve, $k_0 = 6.15$ cm^{-1}, and k is the grating vector.

beam from a laser diode. The dashed curve in Fig. A.3 is a theoretical fit to the derived form of the beam-coupling response [35, 44]

$$I(t) = I_0 \exp\left(\gamma d[1 - \exp(-t/\tau)]\right), \tag{A.1}$$

where I_0 is the detected intensity before the pump is turned on, the interaction length $d = L/\cos\theta_i$, L is the crystal thickness, θ_i is the half-angle between the beams inside the crystal, and the gain γ and rise time τ are parameters determined by the least-squares fit between the measured response and Eq. A.1. The beam coupling gain of our blue crystal as a function of grating vector was measured by repeating this experiment, varying the angle between the writing beams. Shown in Fig. A.4 is the dependence of the beam-coupling gain on the grating wavevector. At a spatially-averaged intensity of 620 mW/cm^2, extraordinary-polarization beam coupling gain (i.e., the second-smallest electrooptic coefficient, r_{33}, was used) was

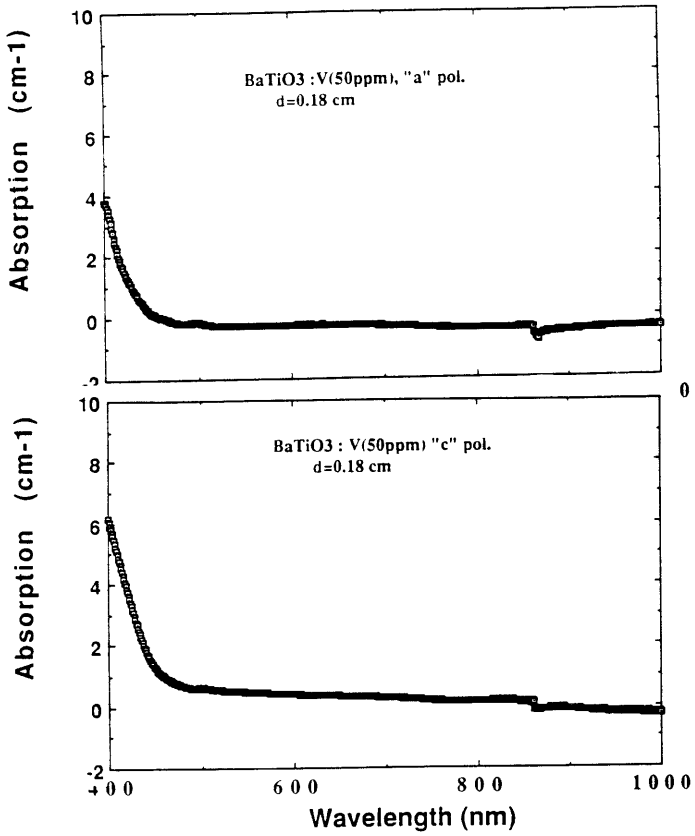

Figure A.5: Absorption spectrum of $BaTiO_3$:V, 50 ppm (crystal 1o#25) in the as-grown state.

$\sim$ 3.2 cm^{-1}. The response time was $\sim$ 7.5 s, which is much faster than had been previously reported for beam coupling in doped or undoped $BaTiO_3$ in the infrared at similar intensities. The photorefractive sensitivity $S = \gamma\lambda/4\pi\alpha I\tau_{PR}$, was calculated to be 0.04 cm^3/kJ. Optimizing the Rh doping level and reduction treatment should allow further improvements in speed beyond that measured to date.

A.3 Infrared photorefractive characterization of green reduced $BaTiO_3$:V

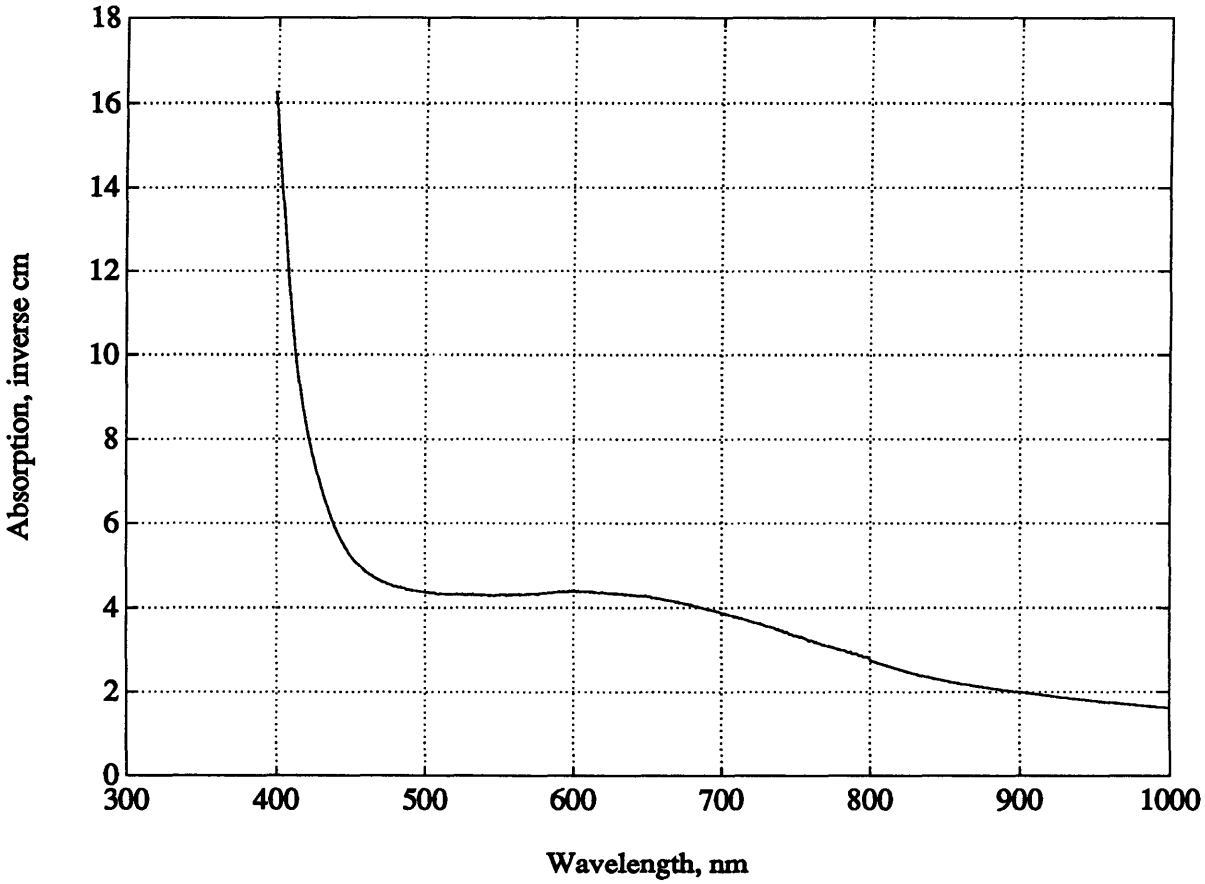

Figure A.6: Absorption spectrum of $BaTiO_3$:V, 50 ppm (crystal 1o#25), reduced at 800°C in approximately 10^{-16} atm. PO_2.

A 50 ppm V-doped $BaTiO_3$ sample was grown, poled and polished. Its absorption spectrum was measured in the as-grown state (Fig. A.5). [1] The photorefractive properties of the crystal were characterized using a laser diode (λ = 830 nm) at an intensity of 1 W/cm^2. The beam coupling gain and risetime were measured at room temperature with total laser intensity $I \simeq 600$ mW/cm^2. The probe/pump intensity ratio was approximately 10:1. The grating period was 0.6 μm. The measured gain was extremely low ($\gamma = 0.1\text{cm}^{-1}$). The response time was also extremely long, τ_{PR} = 420 sec. Similarly low gains (< 0.5 cm^{-1}) were measured at 514.5 nm using an argon laser. This near absence of the photorefractive effect was observed in as-grown $BaTiO_3$:V doped at 25 ppm and 100 ppm as well. Thus the as-grown V-doped $BaTiO_3$ crystals apparently have very low photoconductivity and trap concentration. The photorefractive sensitivity $S = \gamma\lambda/(4\pi\alpha I\tau_{PR})$, defined as the light energy needed per unit refractive index modulation, was calculated to be $S = 2\times10^{-4}\text{cm}^3/kJ$ under these conditions.

The $BaTiO_3$:V crystal was far more sensitive to the diode laser light at 830 nm after reduction treatment. The 50 ppm V-doped $BaTiO_3$ sample was reduced at 800°C in approximately 10^{-16} atm. PO_2. A green-grey sample resulted. The absorption spectrum of the reduced crystal is shown in Fig. A.6. The grating period was Λ = 0.65 μm, nearly the same as that used for the as-grown crystal. The average risetime and average gain were calculated over 5 runs. The resulting measured gain was γ =1.2 cm^{-1} and the risetime at $I \simeq 2$ W/cm^2 was τ_{PR} = 0.37 sec. The photorefractive sensitivity at 830 nm was calculated to be S = 0.08 cm^3/kJ, more than two orders of magnitude higher than in the as-grown crystal. This sensitivity

[1]The crystal doping, growth and annealing were performed in 1993 by Dr. Irina Mnushkina, then with the Crystal Physics and Optoelectronics Laboratory at MIT. It was at her suggestion that these characterization experiments were performed.

is also roughly 2 times higher than that measured in the blue $BaTiO_3$:Rh at the same wavelength. These preliminary results are the only known report of high infrared sensitivity in $BaTiO_3$:V at this time. Vanadium on a titanium site is a donor in $BaTiO_3$. It is known that the electron mobility is higher than the hole mobility in $BaTiO_3$, and n-type photoconductivity may partly explain the fast response of reduced $BaTiO_3$:V. Presumably the low trap density and low photoconductivity in the as-grown $BaTiO_3$:V crystals are due to near compensation between the donors (V) and the background acceptors usually present in $BaTiO_3$ at levels around 100 ppm. Further doping, annealing and optical characterization work on both reduced $BaTiO_3$:V and $BaTiO_3$:Rh would be necessary to determine which dopant is more useful at a particular near-IR wavelength.

Bibliography

[1] S. Redfield and L. Hesselink. Enhanced nondestructive holographic readout in strontium barium niobate. *Opt. Lett.*, 13:880–882, 1988.

[2] D. Brady, K. Hsu, and D. Psaltis. Periodically refreshed multiply exposed photorefractive holograms. *Opt. Lett.*, 15:817, 1990.

[3] H. Sasaki, Y. Fainman, J.E. Ford, Y. Taketomi, and S.H. Lee. Dynamic photorefractive optical memory. *Opt. Lett.*, 16:1874, 1991.

[4] S. Boj, G. Pauliat, and G. Roosen. Dynamic holographic memory showing readout, refreshing, and updating capabilities. *Opt. Lett.*, 17:438, 1992.

[5] F.H. Mok. Angle-multiplexed storage of 5000 holograms in lithium niobate. *Opt. Lett.*, 18:915, 1993.

[6] R.G. Zech. Volume hologram optical memories: mass storage future perfect? *Optics & Photonics News*, page 16, August 1992.

[7] H. Kogelnik. Coupled wave theory for thick hologram gratings. *Bell Syst. Tech. J.*, 48:2909, 1969.

[8] F. Micheron and G. Bismuth. Electrical control of fixation and erasure of holographic patterns in ferroelectric materials. *Appl. Phys. Lett.*, 20:79–81, 1972.

[9] M.H. Garrett. Electrically fixed holograms in $BaTiO_3$. *Opt. Lett.*, 1995.

[10] J.J. Amodei and D.L. Staebler. Holographic pattern fixing in electro-optic crystals. *Appl. Phys. Lett.*, 18:540–542, 1971.

[11] S. Kapphan H. Vormannn, G. Weber and E. Kratzig. Hydrogen as origin of thermal fixing in $LiNbO_3$:Fe. *Solid State Commun.*, 40:543, 1981.

[12] W. Bollmann and H.-J. Stöhr. Incorporation and mobility of OH^- ions in $LiNbO_3$ crystals. *Phys. Stat. Sol. (a)*, 39:477, 1977.

[13] L. Arizmendi. Thermal fixing of holographic gratings in $Bi_{12}SiO_{20}$. *J. Appl. Phys.*, 65:423–427, 1989.

[14] G. Montemezzani and P. Günter. Thermal hologram fixing in pure and doped $KNbO_3$. *J. Opt. Soc. Am. B*, 7:2323, 1990.

[15] G. Montemezzani, M. Zgonik, and P. Günter. Photorefractive charge compensation at elevated temperatures and application to $KNbO_3$. *J. Opt. Soc. Am. B*, 10:171, 1993.

[16] D. Kirillov and J. Feinberg. Fixable complementary gratings in photorefractive $BaTiO_3$. *Opt. Lett.*, 16:1520, 1991.

[17] F. Micheron and G. Bismuth. Field and time thresholds for the electrical fixation of holograms recorded in $(Sr_{0.75}Ba_{0.25})Nb_2O_6$ crystals. *Appl. Phys. Lett.*, 23:71, 1973.

[18] Y. Qiao, S. Orlov, D. Psaltis, and R. Neurgaonkar. Electrical fixing of photorefractive holograms in $Sr_{0.75}Ba_{0.25}Nb_2O_6$. *Opt. Lett.*, 18:1004, 1993.

[19] T.W. McNamara, S.G. Conahan, I. Mnushkina, M.H. Garrett, H.P. Jenssen, and C. Warde. Fixing and IR sensitivity of doped barium titanate. In P. Yeh, editor, *Photorefractive Materials and Devices, SPIE Vol. CR-48*, 1993.

[20] A. Kewitsch, M. Segev, A. Yariv, and R. Neurgaonkar. Selective page-addressable fixing of volume holograms in $Sr_{0.75}Ba_{0.25}Nb_2O_6$ crystals. *Opt. Lett.*, 18:1262, 1993.

[21] D. Rytz, M.B. Klein, R.A. Mullen, R.N. Schwartz, G.C. Valley, and B.A. Wechsler. High-sensitivity fast response in photorefractive $BaTiO_3$ at 120°C. *Appl. Phys. Lett.*, 52:23, 1988.

[22] D. Rytz, B.A. Wechsler, R.N. Schwartz, C.C. Nelson, C.D. Brandle, A.J. Valentino, and G.W. Berkstresser. Temperature dependence of photorefractive properties of strontium-barium niobate ($Sr_{0.6}Ba_{0.4}Nb_2O_6$). *J. Appl. Phys.*, 66:1920, 1989.

[23] M.A. Powell and C.R. Petts. Temperature enhancement of the photorefractive sensitivity of BSO and BGO. *Opt. Lett.*, 11:36, 1986.

[24] P. Nouchi, J.P. Partanen, and R.W. Hellwarth. Temperature dependence of the electron mobility in photorefractive $Bi_{12}SiO_{20}$. *J. Opt. Soc. Am. B*, 9:1428, 1992.

[25] P. Günter and J.-P. Huignard, editors. *Photorefractive Materials and their Applications I: Fundamental Phenomena.* Springer, 1987.

[26] F.S. Chen. A laser-induced inhomogeneity of refractive indices in KTN. *J. Appl. Phys.*, 38:3418–3420, 1967.

[27] P. Günter. Holography, coherent light amplification, and optical phase conjugation in photorefractive materials. *Phys. Reports*, 93:199, 1982.

[28] D.L. Staebler. *Ferroelectric Crystals.* Springer-Verlag, Berlin, 1977.

[29] P. Günter. Holography, coherent light amplification and optical phase conjugation with photorefractive materials. *Phys. Rep.*, 93:199, 1982.

[30] P. Yeh. Two-wave mixing in nonlinear media. *IEEE J. Quant. Electron.*, QE-25:484–519, 1989.

[31] N.V. Kukhtarev. Kinetics of hologram writing and erasure in electro-optic crystals. *Sov. Tech. Phys. Lett.*, 2:438–440, 1976.

[32] N. V. Kukhtarev, V.B. Markov, S.G. Odulov, M.S. Soskin, and V.L. Vinetskii. Holographic storage in electrooptic crystals I: Steady state. *Ferroelectrics*, 22:949–960, 1979.

[33] G.C. Valley and M.B. Klein. Optimal properties of photorefracive materials for optical data processing. *Optical Engineering*, 22:704, 1982.

[34] A.M. Glass, D. von der Linde, and T.J. Negran. High-voltage bulk photovoltaic effect and the photorefractive process in $LiNbO_3$. *Appl. Phys. Lett.*, 25:233–235, 1974.

[35] Ronald Scott Hathcock. *Optical and Photorefractive Properties of Iron-Doped Barium Titanate.* PhD thesis, Massachusetts Institute of Technology, 1989.

[36] P. Günter and U. Flükiger. Optically induced refractive index changes in $KNbO_3$:Fe. *Ferroelectrics*, 13:297–299, 1975.

[37] M. Cronin-Golomb. Analytic solution for photorefractive two-beam coupling with time varying signal. In *Photorefractive Materials, Effects and Devices*, volume 17, pages 142–145. OSA Technical Digest Series, 1987.

[38] D.Z. Anderson and J. Feinberg. Optical novelty filters. *IEEE J. Quant. Electron.*, 25:635–647, 1989.

[39] M. Cronin-Golomb, A.M. Biernacki, C. Lin, and H. Kong. Photorefractive time differentiation of coherent optical images. *Opt. Lett.*, 12:1029–1031, 1987.

[40] A. Hermanns, C. Benkert, D.M. Lininger, and D.Z. Anderson. The transfer function and impulse response of photorefractive two-beam coupling. *IEEE J. Quant. Electron.*, 28:750, 1992.

[41] M. Horowitz, D. Kligler, and B. Fischer. Time-dependent behavior of photorefractive two- and four-wave mixing. *J. Opt. Soc. Am. B*, 8:2204–2217, 1991.

[42] C.T. Field and F.M. Davidson. Photorefractive two-wave mixing in the presence of high-speed optical phase modulation. *Applied Optics*, 32:5285–5298, 1993.

[43] M. Abramowitz and I.A. Stegun, editors. *Handbook of Mathematical Functions.* Dover, 1964.

[44] D.W. Vahey. A nonlinear coupled-wave theory of holographic storage in ferroelectric materials. *J. Appl. Phys.*, 46:3510, 1975.

[45] A. Marrakchi, A.R. Tanguay Jr., J. Yu, and D. Psaltis. Physical characterization of the photorefractive incoherent- to- coherent optical converter. *Opt. Eng.*, 24:124–131.

[46] J. Feinberg, D. Heiman, Jr. A.R.Tanguay, and R.W. Hellwarth. Photorefractive effects and light-induced charge migration in barium titanate. *J. Appl. Phys.*, 51,52:1297–1305,537, 1980,1981.

[47] J. Feinberg. Self-pumped, continuous-wave phase conjugator using internal reflection. *Opt. Lett.*, 7:486–488, 1982.

[48] F.C. Jahoda, P.G. Weber, and J. Feinberg. Optical feedback, wavelength response, and interference effects of self-pumped phase conjugation in $BaTiO_3$. *Opt. Lett.*, 9:362–364, 1984.

[49] B.A. Horwitz and F.J. Corbett. The prom–theory and applications for the pockels readout optical modulator. *Opt. Eng.*, 17:353–364, 1978.

[50] M.P. Petrov, A.V. Khomenko, M.V. Krasin'kova, V.I. Marahonov, and M.G. Shlyagin. The priz image converter and its use in optical data processing systems. *Sov. Phys. Tech. Phys.*, 26:816–821.

[51] P. Aubourg, J.P. Huignard, M. Hareng, and R.A. Mullen. Liquid crystal light valve using bulk monocrystalline $Bi_{12}SiO_{20}$ as the photoconductive material. *Appl. Opt.*, 21:3706, 1982.

[52] C. Kittell. *Introduction to Solid State Physics.* Wiley, 1986.

[53] T. Mitsui and S. Nomura, editors. *Landolt-Börnstein Numerical Tables and Functional Relationships, New Series*, volume Group III, Vol. 16 (a). Springer, 1981.

[54] A.R. Johnston. Dispersion of electro-optic effect in $BaTiO_3$. *J. Appl. Phys.*, 42:3501–3507, 1971.

[55] S.H. Wemple, Jr. M. Didomenico, and I. Camlibel. Dielectric and optical properties of melt-grown $BaTiO_3$. *J. Phys. Chem. Solids*, 29:1797, 1968.

[56] W.N. Lawless and R.C. DeVries. Accurate determination of the ordinary-ray refractive index in $BaTiO_3$. *J. Appl. Phys.*, 35:2638–2639, 1964.

[57] J.F. Nye. *Physical Properties of Crystals, their Representation by Tensors and Matrices.* Clarendon Press, 1957.

[58] D. Berlincourt and H. Jaffe. Elastic and piezoelectric coefficients of single-crystal barium titanate. *Phys. Rev.*, 111:143, 1958.

[59] G. Godefroy, G. Ormancey, P. Jullien, W. Ousi-Benomar, and Y. Semanou. Effect of iron on the photorefractive properties of $BaTiO_3$ single crystals. In *IEEE Sixth International Symposium on Applications of Ferroelectrics.* IEEE Inc., 1986.

[60] M.G. Cohen, M. DiDomenico Jr., and S.H. Wemple. *Phys. Rev. B*, 1:4334, 1970.

[61] S. Ducharme, J. Feinberg, and R.R. Neurgaonkar. Electrooptic and piezoelectric measurements in photorefractive barium titanate and strontium barium niobate. *IEEE J. Quant. Electron.*, QE-23:2116–2121, 1987.

[62] A.R. Johnston. The strain-free electro-optic effect in single-crystal barium titanate. *Appl. Phys. Lett.*, 7:195–198, 1965.

[63] I.P. Kaminow. Barium titanate light phase modulator. *Appl. Phys. Lett.*, 7:123–125, 1965.

[64] E. Nakamura, editor. *Landolt-Börnstein Numerical Tables and Functional Relationships, New Series*, volume Group III, Vol. 28 (a). Springer, 1990.

[65] A. Partovi, A. Kost, E.M. Garmire, G.C. Valley, and M.B. Klein. Band-edge photorefractive effect in semiconductors. *Appl. Phys. Lett.*, 56:1089–1091, 1990.

[66] M. B. Klein and G. C. Valley. Beam coupling in $BaTiO_3$ at 441 nm. *J. Appl. Phys.*, 57:4901, 1985.

[67] D. Mahgerefteh and J. Feinberg. Explanation of the apparent sublinear photoconductivity of photorefractive barium titanate. *Phys. Rev. Lett.*, 64:2195, 1990.

[68] P Tayebati and D. Mahgerefteh. Theory of the photorefractive effect for $Bi_{12}SiO_{20}$ and $BaTiO_3$ with shallow traps. *J. Opt. Soc. Am. B*, 8:1053, 1991.

[69] V.I. Belinicher and B.I. Sturman. The photogalvanic effect in media lacking a center of symmetry. *Sov. Phys. Usp.*, 23:159–223, 1980.

[70] J. Hong and R. Saxena. Diffraction efficiency of volume holograms written by coupled beams. *Opt. Lett.*, 16:182, 1991.

[71] F.A. Kroger and H.J. Vink. *Relations between the concentrations of imperfections in crystalline solids*, pages 307–435. Academic Press, Inc., New York, 1956.

[72] Jenq-Yang Chang. *Effects of Cobalt-Doping, Oxygen-Reduction and Crystllographic Orientation on the Photorefractive Properties of Barium Titanate.* PhD thesis, Massachusetts Institute of Technology, 1992.

[73] F.M. Michel-Calendini and P. Moretti. Electronic structures of Co(II) and Co(III) impurities in cubic perovskite hosts. *Phys. Rev. B*, 27:763–770, 1983.

[74] R. Waser, T. Baiatu, and K.H. Härdtl. D.c. electrical degradation of perovskite-type titanates: Ii, single crystals. *J. Am. Cer. Soc.*, 73:1654–1662, 1990.

[75] H.-J. Hagemann and D. Hennings. Reversible weight change of acceptor-doped $BaTiO_3$. *Journal of the American Ceramic Society*, 64:590–594, 1981.

[76] H.-J. Hagemann and H. Ihrig. Valence change and phase stability of 3d-doped $BaTiO_3$ annealed in oxygen and hydrogen. *Phys. Rev. B*, 20:3871–3878, 1979.

[77] P.G. Schunemann. Growth and characterization of high purity and iron doped photorefractive barium titanate. Master's thesis, Massachusetts Institute of Technology, 1987.

[78] P.G. Schunemann, D.A. Temple, R.S. Hathcock, H. L. Tuller, H. P. Jenssen, D.R. Gabbe, and C. Warde. Role of iron centers in the photorefractive in barium titanate. *J. Opt. Soc. Am. B*, 5:1682, 1988.

[79] N.-H. Chan and D.M. Smyth. Defect chemistry of $BaTiO_3$. *J. Electrochem. Soc.*, 123:1584–1585, 1976.

[80] J. Daniels and K.H. Härdtl. Electrical conductivity at high temperature of donor-doped barium titanate ceramics. *Philips Res. Repts.*, 31:489–504, 1976.

[81] N.G. Eror and D.M. Smyth. Nonstoichiometric disorder in single-crystalline $BaTiO_3$ at elevated temperatures. *Journal of Solid State Chem.*, 24:235–244, 1978.

[82] D. Temple. *Photo-Induced Absorption and Photorefractive Gratings in Barium Titanate.* PhD thesis, Massachusetts Institute of Technology, 1988.

[83] D.D. Nolte, D.H. Olson, and A.M. Glass. Nonequilibrium screening of the photorefractive effect. *Phys. Rev. Lett.*, 63:891–894, 1989.

[84] D.D. Nolte and A.M. Glass. Non-equilibrium charge transfer and low-temperature photorefractive effects. *Optical and Quant. Electron.*, 22:S47–S60, 1990.

[85] Y. Okazaki and K. Kuroda. Temperature dependence of the photorefractive effect in GaP. *Opt. Commun.*, 104:357–362, 1994.

[86] K. Horiuchi and K. Kuroda. Photorefractive and photochromic effects in undoped GaP at high temperature. *Opt. Commun.*, 113:487–492, 1995.

[87] I. Foldvari, J.J. Martin, C.A. Hunt, R.C. Powell, R.J. Reeves, and A. Peter. Temperature dependence of the photorefractive effect in undoped $Bi_{12}GeO_{20}$. *J. Appl. Phys.*, 74:783–789, 1993.

[88] Ph. Delaye and B. Sugg. Temperature enhancement of the photorefractive effect in GaAs due to the metastable state of the EL2 defect. *Phys. Rev. B*, 50:16973–16984 (really), 1994.

[89] R. Feynman. *The Feynman Lectures in Physics, Vol. II.*

[90] V. Belruss, J. Kalnajs, A. Linz, and R.C. Folweiler. Top-seeded solution growth of oxide crystals from non-stoichiometric melts. *Mat. Res. Bull.*, 6:899, 1971.

[91] R. Wernicke. The kinetics of equilibrium restoration in barium titanate ceramics. *Philips Res. Repts.*, 31:526–543, 1976.

[92] T. Bieger, J. Maier, and R. Waser. Kinetics of oxygen incorporation in $SrTiO_3$ (Fe-doped: an optical investigation. *Sensors and Actuators B*, 7:763–768, 1992.

[93] R. Waser. Diffusion of hydrogen defects in $BaTiO_3$ ceramics and $SrTiO_3$ single crystals. *Ber. Bunsenges. Phys. Chem.*, 90:1223–1230, 1986. Article is in English.

[94] R. Waser, T. Baiatu, and K.H. Härdtl. Degradation of dielectric ceramics. *Materials Science and Engineering A*, A109:171–182, 1989.

[95] T. Bieger, J. Maier, and R. Waser. Optical investigation of oxygen incorporation in $SrTiO_3$. *Solid State Ionics*, 53–56:578–582, 1992.

[96] C. Gu and P. Yeh. Diffraction properties of fixed gratings in photorefractive media. *J. Opt. Soc. B*, 7:2339, 1990.

[97] M. Carrascosa and L. Arizmendi. High-temperature photorefractive effects in $LiNbO_3$:Fe. *J. Appl. Phys.*, 73:2709–2713, 1992.

[98] L. Hesselink J.F. Heanue, M.C. Bashaw. Volume holographic storage and retrieval of data. *Science*, 265:749–752, 1994.

[99] R. Sommerfeldt, R.A. Rupp, H. Vormann, and E. Krätzig. Thermal fixing of volume phase holograms in $LiNbO_3$:Cu. *Phys. Stat. Sol. (a)*, 99:K15, 1987.

[100] P. Hertel, K.H. Ringhofer, and R. Sommerfeldt. Theory of thermal hologram fixing and application to $LiNbO_3$:Cu. *Phys. Stat. Sol. (a)*, 104:855, 1987.

[101] M.H. Garrett, private communication.

[102] D. Temple and C. Warde. Anisotropic scattering in photorefractive crystals. *J. Opt. Soc. Am. B*, 3:337–341, 1986.

[103] M.H. Garrett, J.Y. Chang, H.P. Jenssen, and C. Warde. High photorefractive sensitivity in an *n*-type 45°-cut $BaTiO_3$ crystal. *Opt. Lett.*, 17:103, 1992.

[104] R.S. Cudney, J. Fousek, M. Zgonik, P Günter, M.H. Garrett and D. Rytz. Photorefractive and domain gratings in barium titanate. *Appl. Phys. Lett.*, 63:3399–3401, 1993.

[105] R.S. Cudney, J. Fousek, M. Zgonik, P Günter, M.H. Garrett and D. Rytz. Enhancement of the amplitude and lifetime of photoinduced space-charge fields in multidomain ferroelectric crystals. *Phys. Rev. Lett.*, 72:3883–3886, 1994.